DYNAMIC ENHANCEMENT OF THE FUTURE SASKPOWER INTERCONNECTED NORTH AND SOUTH SYSTEMS: THE HVDC INTERCONNECTION

A Thesis

Submitted to the College of Graduate Studies and Research

in Partial Fulfillment of the Requirements

For the Degree of Master of Science

in the Department of Electrical Engineering

University of Saskatchewan

Saskatoon, Saskatchewan

By

Linh Pham

PERMISSION TO USE

I agree that the Library, University of Saskatchewan, may make this thesis freely available for inspection. I further agree that permission for copying of this thesis for scholarly purpose may be granted by the professor or professors who supervised the thesis work recorded herein or, in their absence, by the Head of the Department or the Dean of the College in which the thesis work was done. It is understood that due recognition will be given to me and to the University of Saskatchewan in any use of the material in this thesis. Copying or publication or any other use of this thesis for financial gain without approval by the University of Saskatchewan and my written permission is prohibited.

Request for permission to copy or to make any other use of the material in this thesis in whole or part should be addressed to:

Head of the Department of Electrical and Computer Engineering
University of Saskatchewan
57 Campus Drive
Saskatoon, Saskatchewan S7N 5A9
Canada

ABSTRACT

SaskPower has two separate systems, namely the North and the South systems. The South system contains SaskPower major generation and system load. The North system load is located relatively far from its generation (200 to 300 km). The North system is considered, therefore, to be electrically weaker than the South system. Recently there has been an interest in connecting the two systems to improve the security, stability and reliability of the integrated system. Grid interconnections, however, especially between weak and strong systems, often result in the arising of low-frequency oscillations between the newly connected areas. These oscillations that are termed "inter-area oscillations" exhibit, generally poor damping and can severely restrict system operations by requiring the curtailment of electric power transfers level as an operational measure.

There are two options for SaskPower North and South systems interconnection, namely HVAC and HVDC interconnections (tie-lines). This thesis reports the results of digital time-domain simulation studies that are carried out to investigate the dynamic performance of a proposed 260 km, ± 110 kV, 50 MW Voltage-Sourced Converter HVDC tie-line that would connect SaskPower North and South systems. The potential problems that might arise due to such an interconnection, namely power flow control and low-frequency oscillations are studied and quantified and a proposed feasible solution is presented. In this context, the effectiveness of the HVDC and a Power Oscillations Damping (POD) controller in damping power system oscillations in the tie-line is investigated.

Time-domain simulations are conducted on the benchmark model using the ElectroMagnetic Transients program (EMTP-RV). The results of the investigations have demonstrated that the presented HVDC link and its POD controller are effective in mitigating the low-frequency oscillations between the North and South systems at different system contingencies and operating conditions.

ACKNOWLEDGEMENTS

I would like to acknowledge to my research supervisor Dr. Sherif O. Faried, for giving me the opportunity to pursue the M.Sc. under his super-vision. His valuable guidance, thoughtful suggestion and constructive technical discussions have been a valuable source, inspiration and motivation for me to complete this thesis.

I would like to express my sincere gratitude to my supervisor, Dr. A. Dinh for his consistent encouragement and financial support throughout the course of this research work.

I would also like to acknowledge Dr. U. Karaagac for his valuable advice and support during evaluation of technique in EMTP-RV. I am pleased to thank to all the professors of the Department of Electrical and Computer Engineering, for their course supervision and strengthening my knowledge.

I would also like to express my appreciation to my parents, my brothers and sisters for their encouragement and full support. Special thank goes to my wife and daughter, Chau Nguyen and Nhu Pham, for your love and understanding.

TABLE OF CONTENTS

LIST OF FIGURES

LIST OF TABLES

LIST OF SYMBOLS

A	Blade sweep area (m^2)
C	Capacitor in the transmission line
C_f	Wind turbine blade design constant
C_p	Power coefficient of the blade
E_{fd}	Exciter output voltage
E_{ref}	Reference voltage of the excitation system
E_{SB}	Feedback stabilizing signal of the excitation system
E_R	Output voltage of the voltage regulator amplifier
e_{fd}	Field voltage
e_a, e_b, e_c	Stator three-phase voltages respectively
e_d, e_q	Stator voltages in the d-q reference frame
e_{fd}	Field voltage
G_N1	The generator at bus N1 of the North system
G_N5	The generator at bus N5 of the North system
G_S1	Generator at bus S1 of the South system
G_S2	Generator at bus S2 of the South system
G_S4	Generator at bus S4 of the South system
G_S6	Generator at bus S6 of the South system
H	Inertia constant
i_d, i_q	Stator currents in the d-q reference frame
i_{dc}	Current through the dc capacitor
i_{fd}, i_{1d}, i_{1q}, i_{2q}	Field and damping winding currents in the d-q reference Frame respectively
I, i_{abc}	Current flowing from a VSC to an AC system

K_A	Gain of the voltage regulator amplifier
K_E	Exciter gain
K_{FE}	Feedback stabilizing loop gain of the excitation system
L	Inductance of the transmission line
L_{ad}	d-axis magnetizing inductance
L_{aq}	q-axis magnetizing inductance
L_d, L_q	d and q synchronous inductances
L_{ffd}, L_{11d}, L_{11q}, L_{22q}	Rotor and damping windings self inductances respectively
$L_{s,}$ L_r	Stator and rotor inductances
M	Mutual inductance between rotor and stator
P	Real power
P_{N3N2}	Active power flowing from bus N3 to N2
P_{S2S3}	Active power flowing from bus S2 to S3
P_{S5S3}	Active power flowing from bus S5 to S3
$P_{Windfarm}$	Active power flowing from DFIG Windfarm to bus S4
$P_{tie\text{-}line}$	Active power flowing through the VSC HVDC link
P_m	Mechanical power
Q	Reactive power
R	Rotor radius of the wind turbine
R_L	Resistance of the transmission line
R_a	Armature resistance
R_{fd}, R_{1d}, R_{1q}, R_{2q}	Rotor and damp windings resistances respectively
r_r	Resistance of the RC snubber circuit
P_m	Mechanical power
s	Laplace transformation operator
T_A, T_E, T_{FE}	Time constants in the excitation system
T_{ELEC}	Air-gap torque
T_{MECH}	Mechanical torque
T_m	Time constant in supplemental controller
V_C	Voltage across the series capacitor of the compensated Transmission line
Vdc_T	Voltage at the DC terminals

V_L	Voltage across the inductance of the series capacitor Compensated transmission line
V_{Ld}, V_{Lq}	Voltages across the inductance in the d-q reference frame
V_a, V_b, V_c	Three phase voltages on the AC side
V_{aN}	Converter phase "a" output voltage related to neutral point
$V_{control}$	Control signal
V_{dc}	Voltage across the dc capacitor
V_R	Voltage across the resistance of the series capacitor compensated transmission line
V_b	Infinite-bus voltage
V_t	Generator terminal voltage
V_s, Vs_{abc}	AC system voltage
V_{sd}, V_{sq}	q-axis and d-axis components of the AC system voltage
V_{sh}, Vsh_{abc}	Source voltages of the converter station
V_{shd}, V_{shq}	q-axis and d-axis components of the AC system voltage of source voltages of the converter station
V_s, V_r	Stator and rotor side voltages
V_{td}, V_{tq}	d- and q- axis generator terminal voltages
$V_{tie\text{-}line}$	AC voltage on HVDC after inverter
V_{tri}	Triangular carrier signal
V_{N1}, V_{N2}, V_{N3}, V_{N4}, V_{N5}, and V_{N6}	System bus voltages of the North system
V_{S1}, V_{S2}, V_{S3}, V_{S4}, V_{S5}, V_{S6} and V_{S6}	System bus voltages of the South system
V_w	Wind speed (m/s)
X_L	Reactance of the transmission line
X_l	Converter reactance
X_c, Z_c	Impedance of the transmission line
Ψ_d, Ψ_q	Stator flux linkages in d-q components
Ψ_{fd}, Ψ_{1d}, Ψ_{1q}, Ψ_{2q}	Rotor flux linkages in d-q components
δ	Generator power angle
δ_{sh}	Phase angle of the VSC source voltage
λ	Wind turbine blade tip speed ratio

$\lambda_{s,}\lambda_{r}$	Stator and rotor side flux linkages
$\lambda_{qm,}\lambda_{dm}$	q-axis and d-axis magnetizing flux linkages
ω	Generator speed
ω_{N1N5}	Generator speed G_N1 measured with respect to generator G_N5
ω_{S4S1}	Generator speed G_S1 measured with respect to generator G_S4
ω_{S4S2}	Generator speed G_S2 measured with respect to generator G_S4
ω_{S4S6}	Generator speed G_S6 measured with respect to generator G_S4
$\omega_0 (f_0)$	Synchronous frequency (377 rad/sec)
Ωm	Mechanical angular velocity (rad/s)

Chapter 1

INTRODUCTION

1.1 General

SaskPower has two separate systems, namely the North and the South systems. The South system contains SaskPower major generation and system load. Recently there has been an interest in connecting the two systems to improve the security, stability and reliability of the integrated system. The benefits of grid interconnections are conclusive. Some of the major technical benefits, many of which have economic impacts are:

- Improving power system reliability through sharing reserve generating capacity within an interconnected network. Grid interconnections also allow the coordination of planned outages of the generating units and transmission facilities for maintenance such that the overall cost is optimized. This has a direct positive impact on power system reliability.

- Reducing investment in adding new generating capacity since individual systems would be able to share their generating resources.

- Improving the load factor through the diversity of system loads with different daily or seasonal patterns that complement their own.

Grid interconnections, however, often result in the arising of low-frequency oscillations between the newly connected areas. These oscillations that are termed "inter-area oscillations" exhibit, generally, poor damping [1]. Inter-area oscillations can severely restrict system operations by requiring the curtailment of electric power transfers level as an operational measure. These oscillations can also lead to widespread system disturbances, e.g, cascading outages of transmission line and, therefore, system wide voltage collapse. Figure 1.1 illustrates the real power flow through an interconnection (tie-line) between two large systems during and after clearing a three-cycle, three-phase fault on a system bus. As it can be seen from this figure, the damping of the tie-line power oscillations is low and results in system instability.

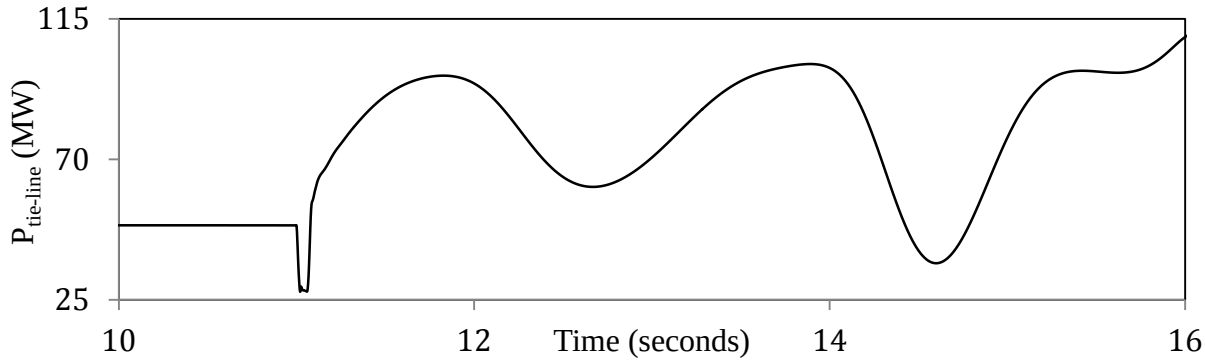

Figure 1.1: A tie-line real power flow during and after clearing a three cycle, three-phase fault on a system bus.

1.2 SaskPower North and South Systems

Figure 1.2 shows a simple schematic diagram of SaskPower North and South systems. The North system which is connected to the Manitoba grid by a tie-line for the purpose of power exchange has two hydro generating stations located near Uranium city and Nipawin. The load in the North system is located relatively far from its generation (200 to 300 km). The South system which contains SaskPower major generation and system load is connected to Manitoba, Alberta and North Dakota grids by an AC tie-line, a DC back-to-back link and an AC tie-line respectively. The North system is, thus, considered to be electrically weak relative to the South system.

The interconnection (tie-line) between SaskPower North and South Systems could be either a High Voltage Alternating Current (HVAC) or a High Voltage Direct Current (HVDC) interconnection. Each option has its own advantages and disadvantages. In the following sections, an introduction to each option and a comparison between them are presented.

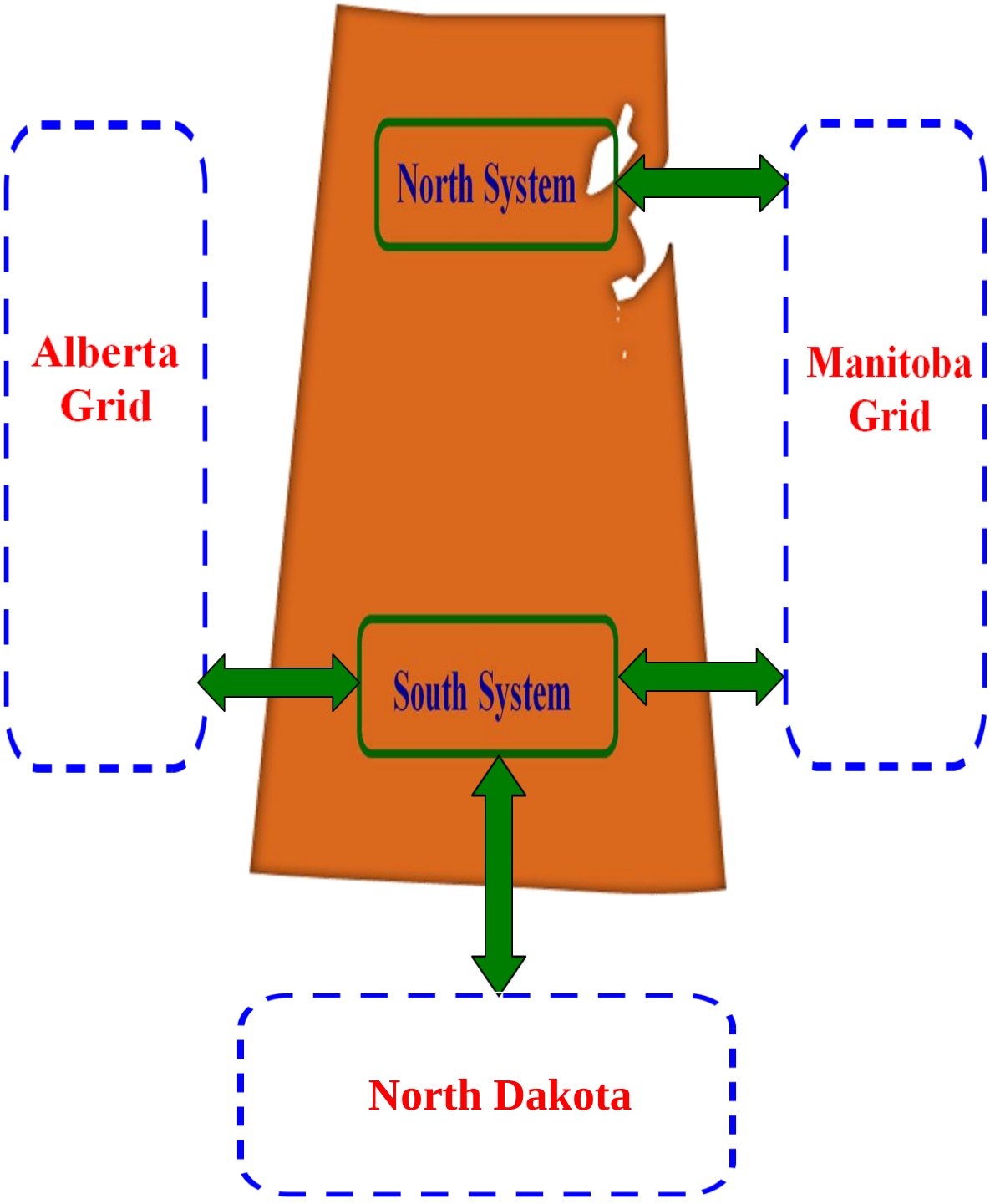

Figure 1.2: SaskPower North and South systems (the two directional arrows represent power import/export from/to the neighboring systems).

1.3 HVAC Interconnection

The AC network is dominant in electrical power system and, therefore, AC transmission became very common in domestic and commercial uses. However, an important factor dealing with HVAC tie-lines is that they consume and produce reactive power, so there is a technical limit to the transmission distance. In the studies conducted in this thesis, it is planned to transmit 50 MW from the North system to the South system over a distant of 260 km. With such a power level, a 138 kV HVAC double-circuit transmission link is selected as shown in Figures 1.3. The justification of such a choice is as follows:

The power transfer capacity of a transmission line is governed by its Surge Impedance Loading (SIL). The SIL is a function of the transmission line characteristic impedance, Z_c and the transmission line voltage. The transmission line characteristic impedance is defined by the following equation

$$Z_C = \sqrt{\frac{R + j\omega L}{j\omega C}} \sim \sqrt{\frac{L}{C}}(1 - j\frac{R}{2\omega L}) \tag{1.1}$$

where $R + j\,\omega L$ is the transmission line series impedance, C is the line shunt capacitance and ω is the power frequency ($2\pi \times 60$ rad/sec). Typical values of Z_C are 400 Ω and 200 Ω for single- and double-circuit transmission line respectively.

The characteristic impedance *Zc* with the line losses neglected is commonly referred to as the *surge impedance.* The definition of the SIL is "the power delivered by a transmission line when it is terminated by its surge impedance is known as the natural load or the surge impedance load (SIL)" [2]. At such an ideal condition, the reactive power consumed by the line series inductance is equal to the reactive power generated by its shunt capacitance. The SIL is given by the following equation

$$SIL = \frac{(Line\,voltage\,in\,kV)^2}{Z_C\ in\ \Omega} \quad MW \tag{1.2}$$

The SIL of 138 kV and 220 kV transmission lines are around 50 MW and 140 MW respectively. Although a single-circuit 138 kV transmission line is able to transmit the planned 50 MW from SaskPower North to South systems, to ensure high reliability and continuity of the

power flow over such a vital interconnection, a 138 kV double-circuit transmission line with a 100 MW (2 × 50 MW for each circuit) rated capacity will be used.

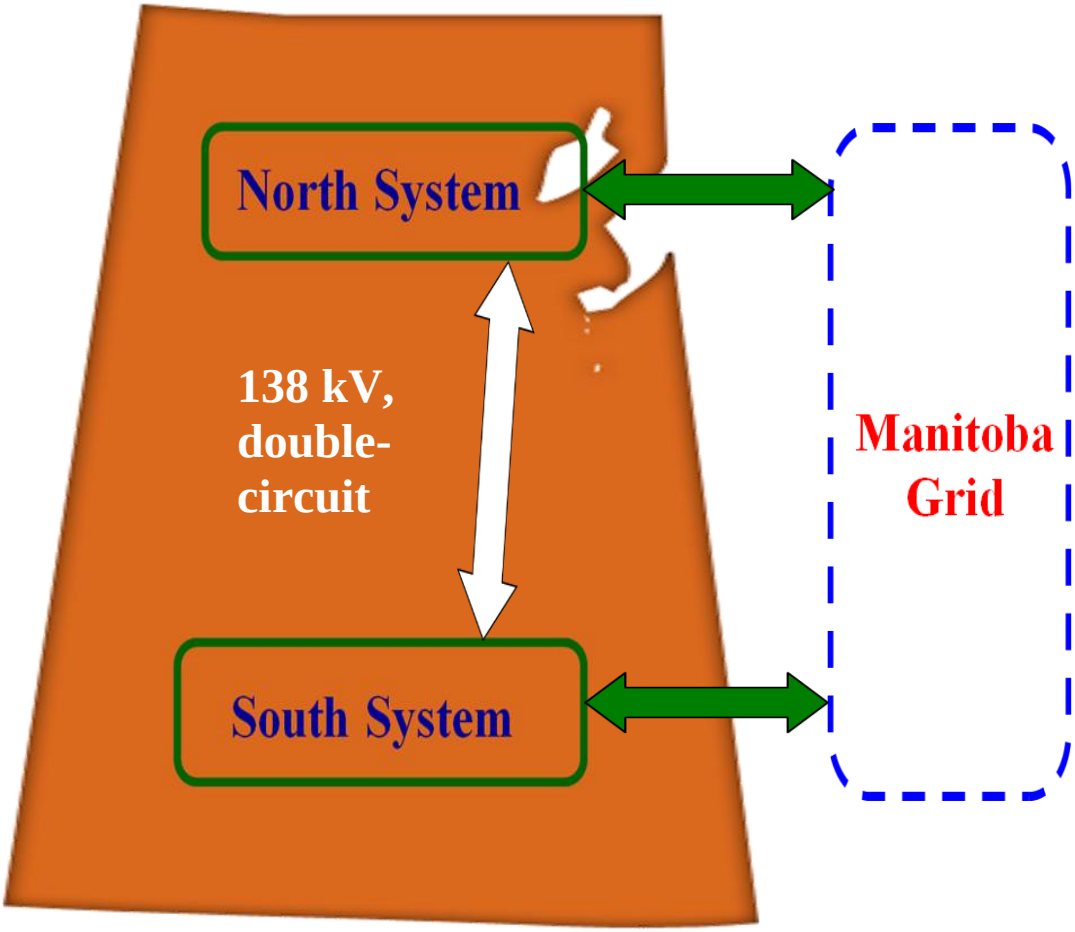

Figure 1.3: The simplified HVAC interconnection system.

One of the major drawbacks of HVAC transmission is its inability to provide natural damping to the low-frequency oscillations. For that reason, some major HVAC transmission lines are equipped with power flow and damping controllers that belong to the FACTS family. Flexible AC Transmission Systems (FACTS) devices are power electronic based controllers which can control impedances and/or phase angles, system currents, voltages, currents effectively [3], [4]. Furthermore, the FACTS devices can influence the active and reactive power, as well as damping system oscillations to improve system stability. Many FACTS devices are installed in the electric grid such as Thyristor Controlled Series Capacitor (TCSC), Static Synchronous Compensator (STATCOM), Unified Power Flow Controller (UPFC), Static Series Synchronous Compensator (SSSC) and Static VAR Compensator (SVC).

1.4 HVDC Link (Interconnection)

Comparing to HVAC transmission, the advantages of HVDC transmission are well known; no technical limit to the transmission distance because of the no reactive power flow on the DC line, excellent asynchronous interconnection, rapid and easy controllability of the power through converter control, no large line inductive reactance or stability problems, bulk power transmission, less reactive power consumption at the AC sides and low DC line resistance. For environmental benefits, HVDC has no skin effect, low corona and low radio interference [5]. Figures 1.4 shows a simplified HVDC interconnection. There are two types of HVDC transmission technologies; Line Commutated Current Source Converter (LCC CSC) and self-commutated Voltage Sourced Converter (VSC).

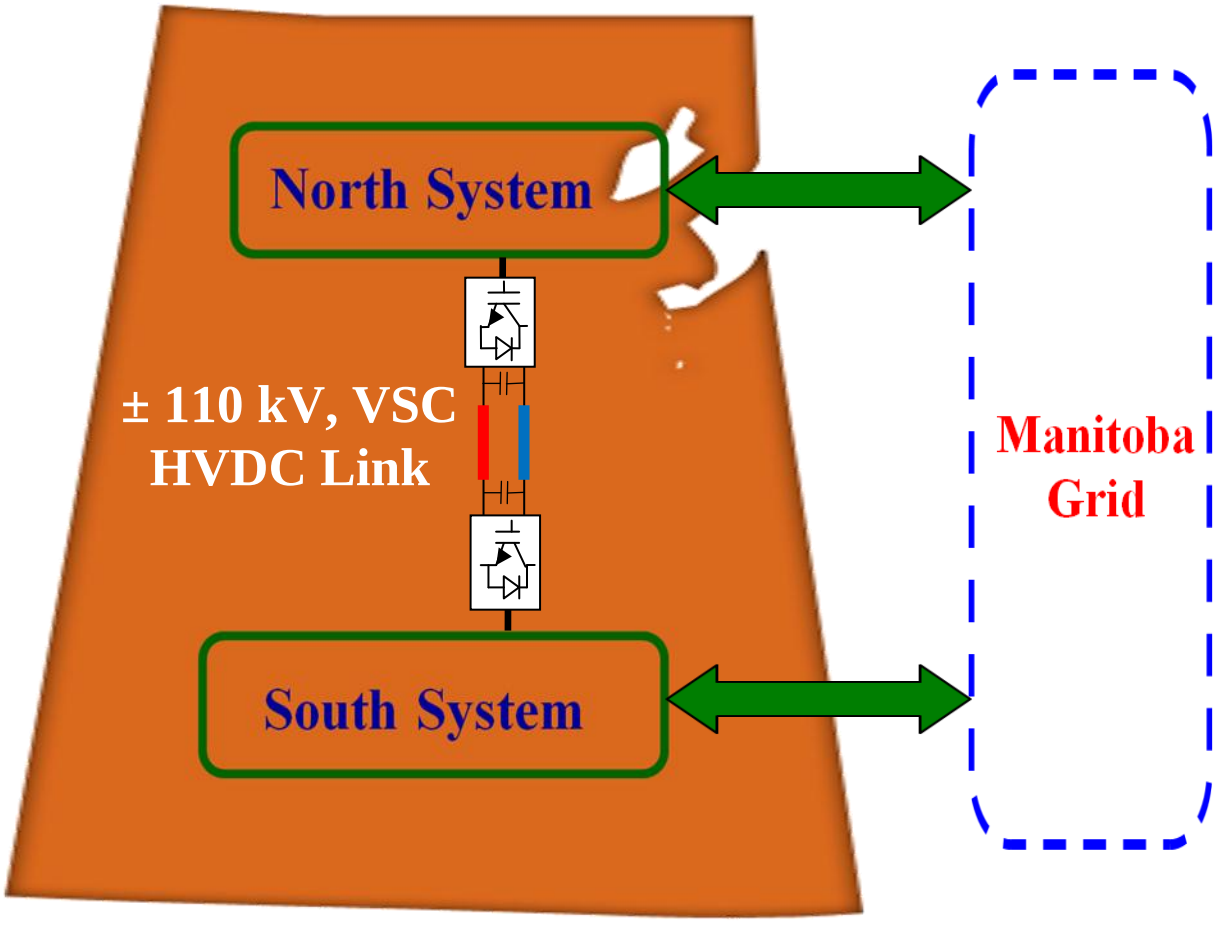

Figure 1.4: The simplified HVDC interconnection system.

1.4.1 LCC CSC transmission

Figure 1.5 shows a simplified diagram of an HVDC LCC CSC transmission system. The gate signal controls turning on the thyristor valves while the zero crossing of the AC current which is determined by the AC network voltage determines the instant of naturally turning off the thyristor valves. The LCC CSC scheme inherits some weaknesses such as harmonic distortion, large AC over-voltage during major system disturbances, commutation failure and the inability to feed a weak AC or passive network because the converter depends on the AC network voltage to commutate [6] [7].

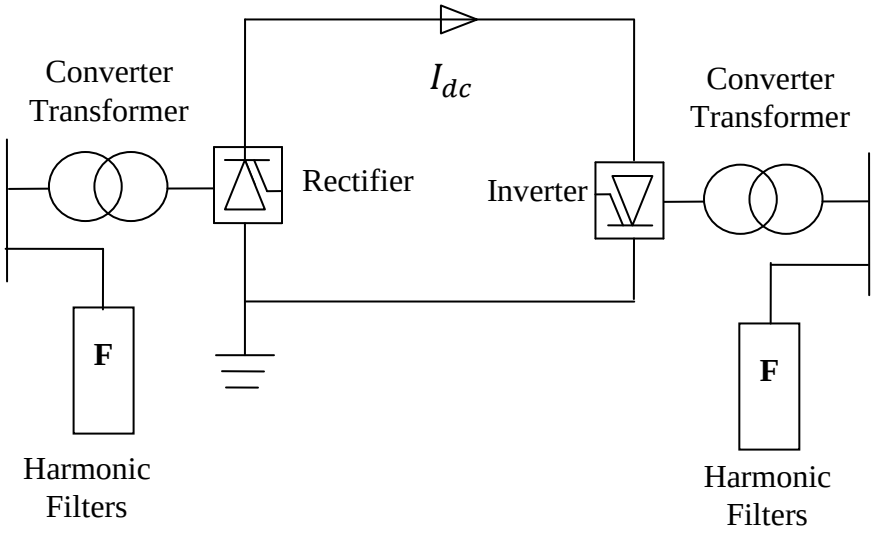

Figure 1.5: The **s**implified monopolar HVDC scheme.

1.4.2 VSC transmission

The capability of independently active and reactive power control as well as independently control at two end converters of VSC can overcome the weaknesses of the CSC scheme. The detailed of VSC controlling method is presented in Chapter 2. Figures 1.6 and 1.7 show simplified diagrams of HVDC VSC transmission system and VSC station respectively.

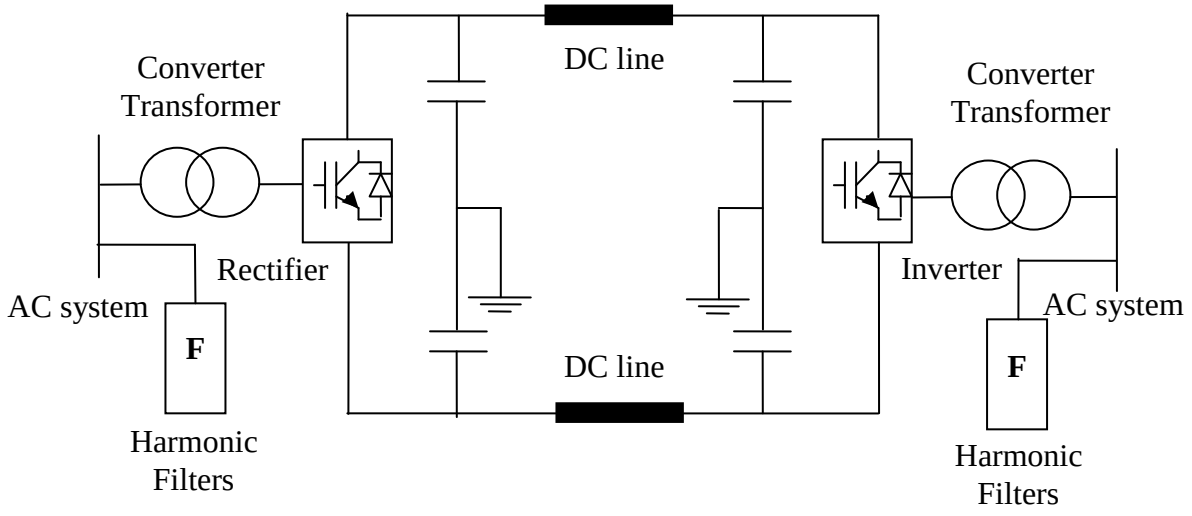

Figure 1.6: A simplified diagram of a VSC HVDC system.

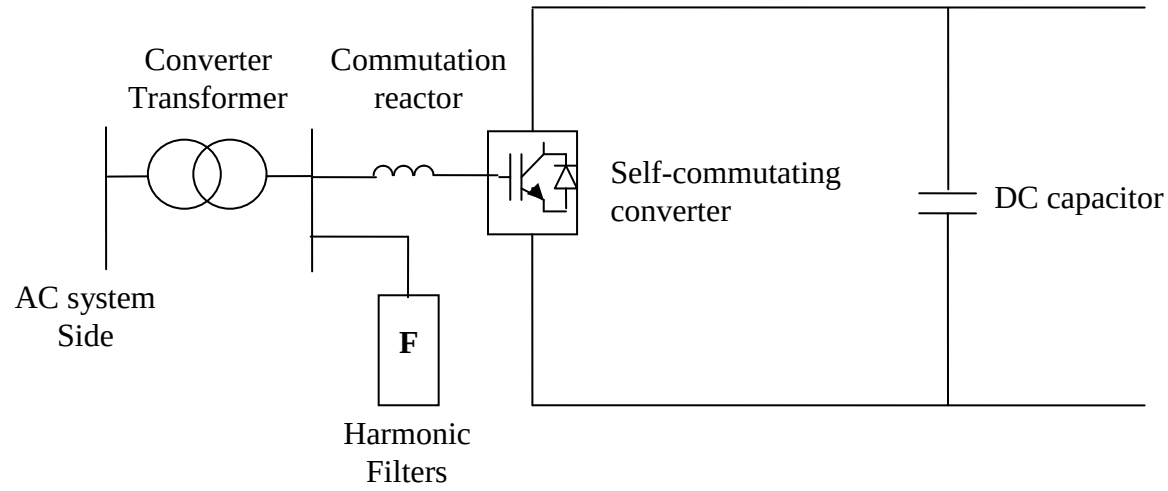

Figure 1.7: A schematic diagram of a VSC station.

The VSC station basically consists of a DC capacitor, a self-commutating converter, a commutation reactor, AC harmonic filters and a converter transformer.

The function of the **converter transformer** is to transform the voltage of AC the power grid to the required voltage of the converter and vice versa.

The commutation reactor or smoothing reactor is the high inductance reactor that eliminates the harmonic currents and voltages in the dc line. It also limits the short circuit current.

The AC harmonic filter filters the harmonic voltages and currents on the AC sides that are produced by the power conversion process.

The DC capacitor takes the roles of electrical energy storage of the DC lines and DC voltage ripple reduction.

The self-commutating convertor uses Insulated Gate Bipolar Transistors (IGBTs) with gate signal control to switch on and off. It is possible for the VSC to influence both the phase angle and the amplitude of the fundamental frequency component of the ac voltage by switching the valves on and off several times during each cycle. The ability of phase angle control allows the VSC to effectively adjust the transmitting active power, while the magnitude control enables the VSC to manage the exchanging reactive power.

Pulse-Width Modulation (PWM) technique, shown in Figure 1.8, illustrates how the VSC is able to influence the magnitude and phase angle. The triangular wave is the carrier wave and the pure sine wave is the voltage reference. The figure shows the derivation of the control signals (a), and the resulting wave shape (b). The coupling between the carrier wave and the voltage reference determines the switching time for the VSC valves. Basically, the VSC controls the phase angle and the amplitude of the converter ac voltage.

In practice, VSC technologies exist at two and three-level VSC topologies. A two-level VSC consisting of six IGBTs, with two IGBTs placed on each leg is shown in Figures 1.9 and 1.10. The diode is connected in an anti-parallel connection to allow bidirectional current flow. The advance of Modular Multilevel Convertors (MMCs) HVDC is expected to improve the scalability, performance and efficiency [8], [9].

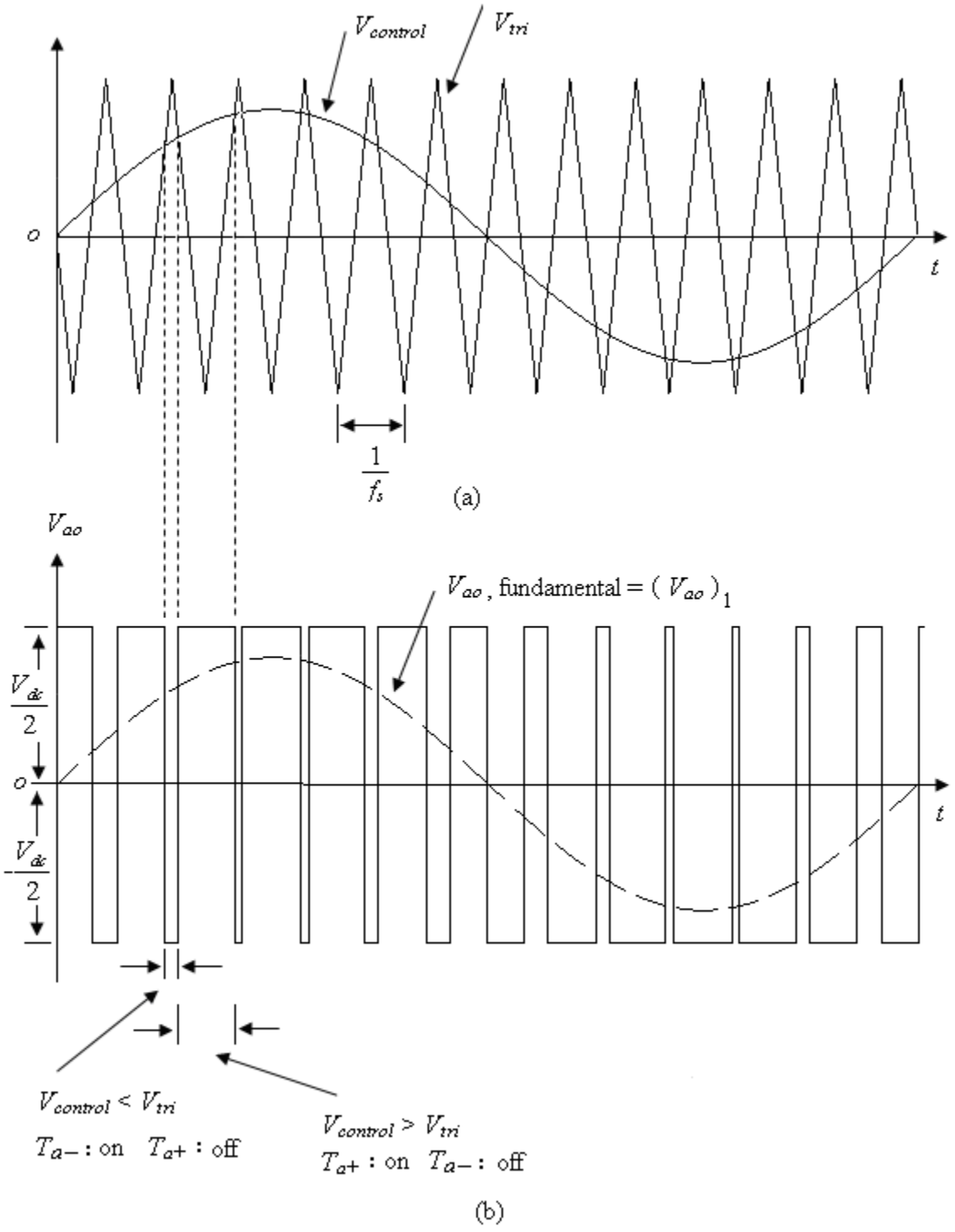

Figure 1.8: PWM controlled VSC with a pure sine-wave converter ac voltage and a triangular carrier.

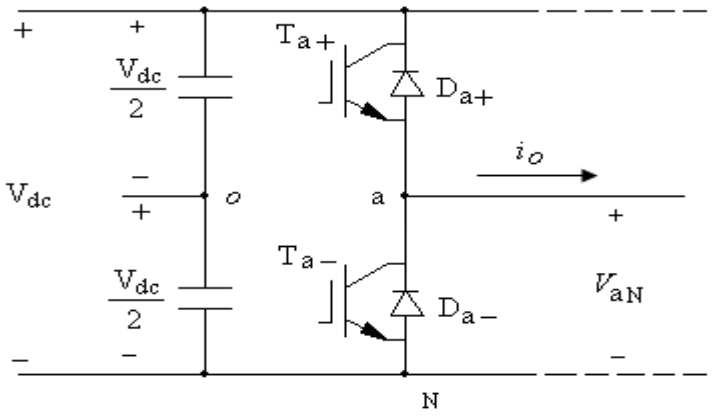

Figure 1.9: A single-phase two-level VSC.

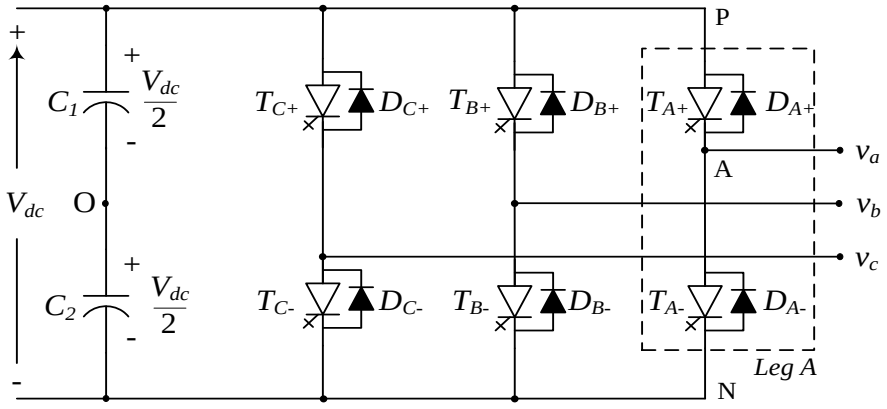

Figure 1.10: A three-phase, two-level VSC.

1.4.3 Principle of voltage source converter operation

Figure 1.11 shows one line diagram of a VSC connected to an AC system [10]. The converter produces an AC voltage with a fundamental frequency equal to that of the AC reference voltage. The voltage at the supply bus is assumed to be $V_s \angle 0^0$, and the AC voltage produced by the VSC is taken to be $V_{sh} \angle \delta_{sh}$. X_l is the reactance of the converter reactor.

The active and the reactive power can be expressed respectively as

$$P = \frac{V_{sh} V_s}{X_l} \sin \delta_{sh} \tag{1.3}$$

$$Q = \frac{V_{sh} V_s}{X_l} \cos \delta_{sh} - \frac{V_{sh}^{\ 2}}{X_l} \tag{1.4}$$

It can be seen from Equations 1.3 and 1.4 that the active and reactive power (P, Q) can be controlled by varying Vs, V_{sh} and δ_{sh}. In a strong system, Vs can be considered constant. Therefore, P and Q can be controlled by changing the magnitude $|V_{sh}|$ and the phase angle δ_{sh} of the converter AC voltage. That also means that VSC is able to control the active and reactive power on the HVDC interconnection.

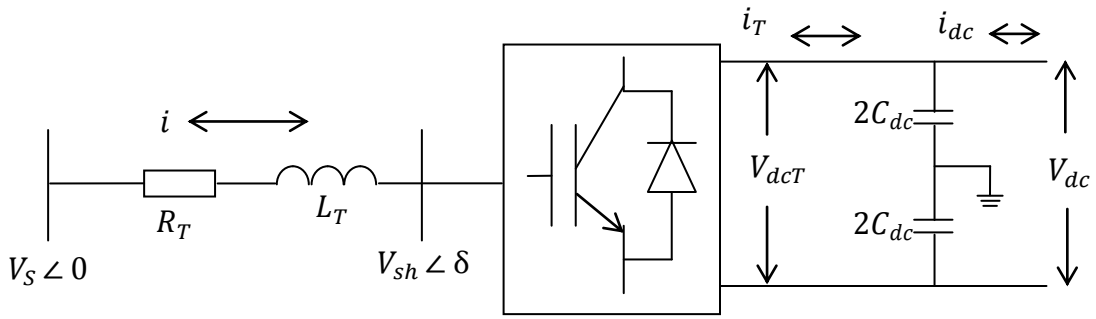

Figure 1.11: A VSC connected to an AC system.

1.5 Inter-Area Oscillations

When two power systems (two areas) are connected via a tie-line as shown in the Figure 1.12, two types of low-frequency oscillations can be observed. The first type is known as local-modes of oscillations. It involves a generator (or a group of generators) in one area oscillating against another generator (or another group of generators) in the "*same"* area. Figure 1.13 illustrates an example of a local mode of oscillations in area 1 between G_{11} - G_{12} and G_{13}. The second type is known as inter-area-modes of oscillations. It involves the generators in Area 1 oscillating as a coherent generator against the generators in Area 2 that are also oscillating as a coherent generator. Figure 1.14 illustrates an example of the inter-area mode of oscillations between Areas 1 and 2. The frequency of inter-area oscillations which depends on the strength of the system and on the moment of inertia of the generator rotors lies in the range of 0.1 Hz to 2.5 Hz [11], [16]. The consequence of inter-area oscillations can be excessive wear of mechanical actuators of the machine controllers, fatigue of in the generator shaft system, system instability or even major system blackouts.

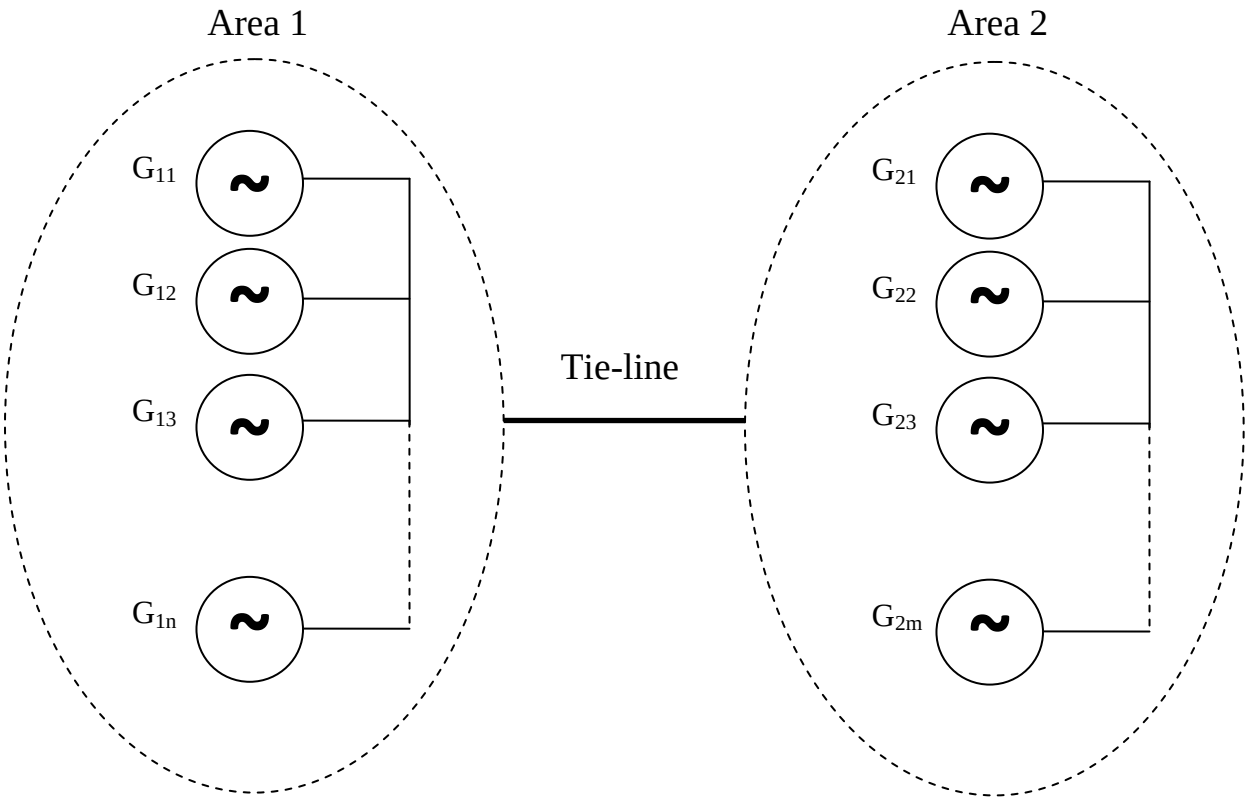

Figure 1.12: A simplified interconnected two-area system.

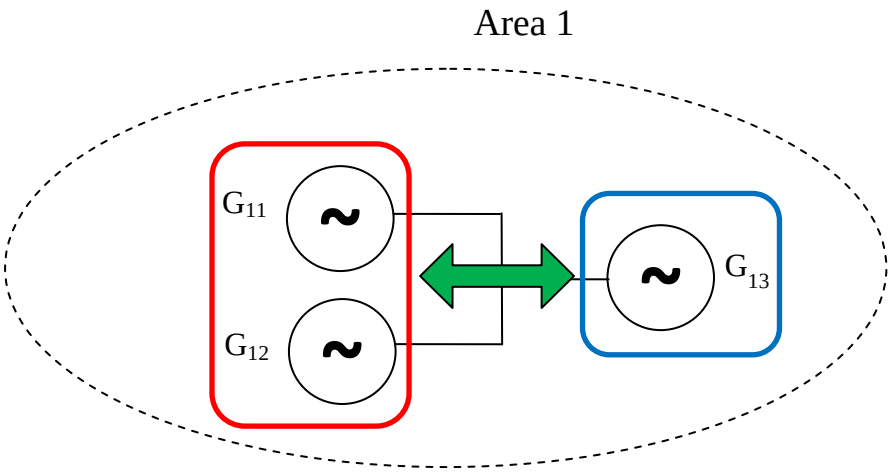

Figure 1.13: A local oscillation mode in Area 1.

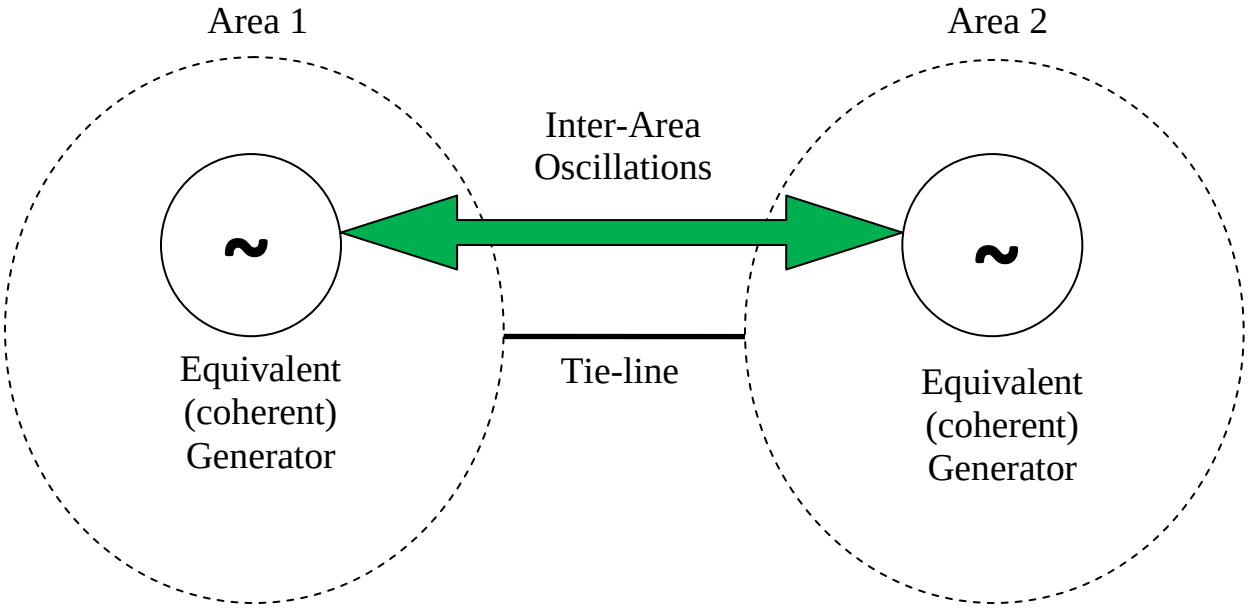

Figure 1.14: An inter-area oscillation mode between Areas 1 and 2.

Local modes of oscillations are primarily influenced and determined by the local states. Inter-area oscillations are more difficult to study and investigate because they need the complete interconnected system to study and their characteristics are determined by the global states of the entire power system. Since this research work involves an interconnection (tie-line) between SaskPower North and the South systems, inter-area oscillations are of a major concern.

1.6 Research Objectives and Scope of the Thesis

The main objective of this research work is to investigate the dynamic performance of a proposed 260 km, ± 110 kV, 50 MW VSC HVDC tie-line that would connect SaskPower North and South systems. The potential problems that might arise due to such an interconnection, namely power flow control and low-frequency oscillations should be studied and quantified and a proposed feasible solution should be established. In this context, the effectiveness of the HVDC and a Power Oscillations Damping (POD) controller in damping power system oscillations in the tie-line is investigated.

The research work consists of the following four major tasks in order to meet its objective.

- Developing adequate models for SaskPower North and South systems suitable for studying the dynamic performance of the VSC HVDC interconnection.
- Studying the power flows of SaskPower North and South systems before and after incorporating the interconnection and identifying any major loop flow problems (e.g, overloaded transmission lines) in the interconnected system.
- Proposing a POD supplemental controller that introduces a supplementary control signal in the main VSC HVDC controller in order to enhance the damping of the low-frequency oscillations.
- Conducting dynamic stability studies on the interconnected system using time-domain simulations to examine the performance of the HVDC main controller as well as the POD supplemental controller in damping the system low- frequency oscillations.

The thesis is organized in five chapters, a list of references section and an appendix.

In Chapter 1, the fundamental benefits and the problems arising from grid interconnections are introduced. A brief introduction to SaskPower North and South systems and the objective of the research are also presented in this chapter.

In Chapter 2, the system used for the investigations conducted in this thesis is described and the detailed dynamic models of its individual components are also presented in this chapter. The results of the digital time-domain simulations of a case study for the system during a three-phase fault are presented at the end of this chapter.

In Chapter 3, the load flow profiles of the North and South systems as well as the interconnected North and South systems (with HVAC and HVDC tie-lines) are examined and important conclusions are drawn. The structures of the HVDC main controller as well as the POD supplemental controller and its possible stabilizing signals are also presented in this chapter.

In Chapter 4, the effectiveness of the VSC HVDC main controller in damping power system oscillations is demonstrated through several time-domain simulation case studies. The

performance of the POD supplemental controller in enhancing the damping of the system oscillations is also presented in this chapter.

Chapter 5 summarizes the research described in this thesis and presents some conclusions.

The data of the systems under investigations are given in Appendix A.

Chapter 2

POWER SYSTEM MODELING FOR LARGE DISTURBANCE STUDIES

2.1 Introduction

This chapter discusses the mathematical models of the various components of the system under study and the models of SaskPower North and South systems suitable for studying the dynamic performance of the HVAC and HVDC interconnections. The results of digital time-domain simulations of a case study of the integrated system incorporating the HVAC interconnection during a three-phase fault are also presented at the end of this chapter.

2.2 Power System Modeling

The nonlinear differential equations of the system under study are derived by developing individual mathematical models which represent the various components of the system, namely the synchronous generator, the excitation system, the transmission line, the system load, the DFIG wind turbine and the VSC HVDC tie-line. Knowing the mutual interaction among these models, the whole system differential equations can be formed.

2.2.1 Modeling of the synchronous machine

In a conventional synchronous machine, the stator circuit consisting of a three-phase winding produces a sinusoidally space distributed magnetomotive force. The rotor of the machine carries the field (excitation) winding which is excited by a dc voltage. The electrical damping due to the eddy currents in the solid rotor and, if present, the damper winding is represented by three equivalent damper circuits; one on the direct axis (d-axis) and the other two on the quadrature axis (q-axis). The performance of the synchronous machine can be described by the equations given below in the d-q reference frame [12], [13]. In these equations, the convention adopted for the signs of the voltages and currents are that v is the impressed voltage at the terminals and that the direction of positive current i corresponds to generation. The sign of

the currents in the equivalent damper windings is taken positive when they flow in a direction similar to that of the positive field current [12].

With time t expressed in seconds, the angular velocity ω expressed in rad/s ($\omega_0 = 377 rad/\sec$) and the other quantities expressed in per unit, the stator equations become:

$$e_d = \frac{1}{\omega_0}\frac{d\Psi_d}{dt} - \frac{\omega}{\omega_0}\Psi_q - R_a i_d \tag{2.1}$$

$$e_q = \frac{1}{\omega_0}\frac{d\Psi_q}{dt} + \frac{\omega}{\omega_0}\Psi_d - R_a i_q \tag{2.2}$$

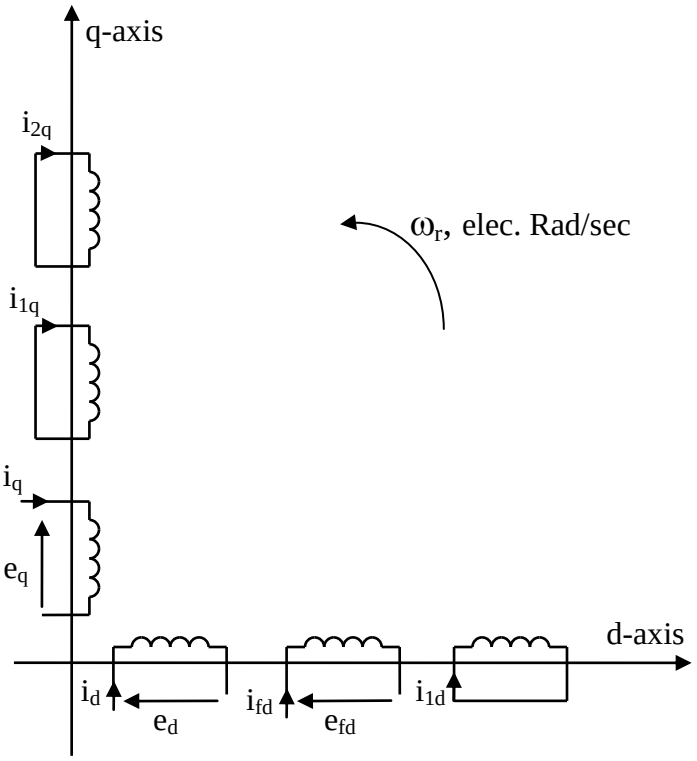

Figure 2.1: Modeling of the synchronous machine in the d-q reference frame.

The rotor equations are:

$$e_{fd} = \frac{1}{\omega_0}\frac{d\Psi_{fd}}{dt} + R_{fd} i_{fd} \tag{2.3}$$

$$0 = \frac{1}{\omega_0}\frac{d\Psi_{1d}}{dt} + R_{1d} i_{1d} \tag{2.4}$$

$$0 = \frac{1}{\omega_0}\frac{d\Psi_{1q}}{dt} + R_{1q} i_{1q} \tag{2.5}$$

$$0 = \frac{1}{\omega_0}\frac{d\Psi_{2q}}{dt} + R_{2q}i_{2q} \tag{2.6}$$

The stator flux linkage equations:

$$\Psi_d = -L_d i_d + L_{ad} i_{fd} + L_{ad} i_{1d} \tag{2.7}$$

$$\Psi_q = -L_q i_q + L_{aq} i_{1q} + L_{aq} i_{2q} \tag{2.8}$$

The rotor flux linkage equations:

$$\Psi_{fd} = L_{ffd} i_{fd} + L_{ad} i_{1d} - L_{ad} i_d \tag{2.9}$$

$$\Psi_{1d} = L_{ad} i_{fd} + L_{11d} i_{1d} - L_{ad} i_d \tag{2.10}$$

$$\Psi_{1q} = L_{11q} i_{1q} + L_{aq} i_{2q} - L_{aq} i_q \tag{2.11}$$

$$\Psi_{2q} = L_{aq} i_{1q} + L_{22q} i_{2q} - L_{aq} i_q \tag{2.12}$$

The electromagnetic torque equation:

$$T_e = \Psi_d i_q - \Psi_q i_d \tag{2.13}$$

The matrix equation below expresses the transient performance of the synchronous machine:

$$\left[\frac{dX_{syn}}{dt}\right] = \left[At_{syn}\right]\left[X_{syn}\right] + \left[Bt_{syn}\right]\begin{bmatrix} V_{td} \\ V_{tq} \\ e_{fd} \end{bmatrix} \tag{2.14}$$

where

$$\left[X_{syn}\right] = \begin{bmatrix} i_d & i_q & i_{fd} & i_{1q} & i_{1d} & i_{2q} \end{bmatrix}^T$$

$$\left[At_{syn}\right] = \left[L\right]^{-1}\left[Qt\right]$$

$$\left[Bt_{syn}\right] = \left[L\right]^{-1}\left[Rt\right]$$

$$\left[L\right] = \begin{bmatrix} -L_d & 0 & L_{ad} & 0 & L_{ad} & 0 \\ 0 & -L_q & 0 & L_{aq} & 0 & L_{aq} \\ -L_{ad} & 0 & L_{ffd} & 0 & L_{ad} & 0 \\ 0 & -L_{aq} & 0 & L_{11q} & 0 & L_{aq} \\ -L_{aq} & 0 & L_{ad} & 0 & L_{11d} & 0 \\ 0 & -L_{aq} & 0 & L_{aq} & 0 & L_{22q} \end{bmatrix} \tag{2.15}$$

$$[Qt]=\begin{bmatrix} \omega_0 R_a & -\omega L_q & 0 & \omega L_{aq} & 0 & \omega L_{aq} \\ \omega L_d & \omega_0 R_a & -\omega L_{ad} & 0 & -\omega L_{ad} & 0 \\ 0 & 0 & -\omega_0 R_{fd} & 0 & 0 & 0 \\ 0 & 0 & 0 & -\omega_0 R_{1q} & 0 & 0 \\ 0 & 0 & 0 & 0 & -\omega_0 R_{1d} & 0 \\ 0 & 0 & 0 & 0 & 0 & -\omega_0 R_{2q} \end{bmatrix}$$

$$[Rt]=\begin{bmatrix} \omega_0 & 0 & 0 \\ 0 & \omega_0 & 0 \\ 0 & 0 & \omega_0 \\ 0 & 0 & 0 \\ 0 & 0 & 0 \\ 0 & 0 & 0 \end{bmatrix}$$

Below is the swing equation of a synchronous machine:

$$\frac{2H}{\omega_o}\frac{d\omega}{dt} = T_{MECH} - T_e \tag{2.16}$$

$$\frac{d\delta}{dt} = \omega - \omega_o \tag{2.17}$$

2.2.2 Modeling of the transmission line

A series capacitor-compensated transmission line may be represented by the *RLC* circuit shown in Figure 2.2 [14]. In the voltage phasor diagram shown in Figure 2.3, the rotor angle δ is the angle (in elec. rad) by which the q-axis leads the reference voltage V_b. The differential equations for the circuit elements, after applying Park's transformation [14], can be expressed in d-q reference frame by the following matrix expressions.

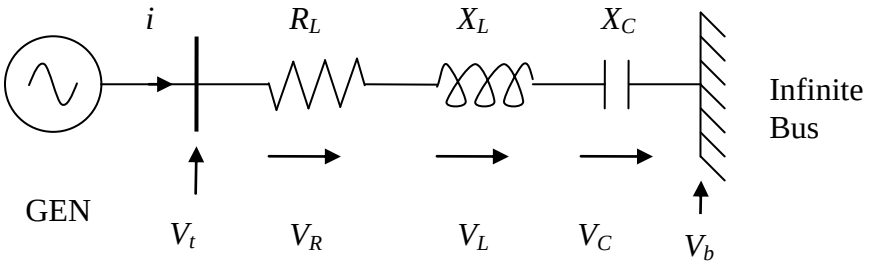

Figure 2.2: The transmission line model.

The voltage drops at the inductance:

$$\begin{bmatrix} V_{Ld} \\ V_{Lq} \end{bmatrix} = \begin{bmatrix} 0 & -\dfrac{\omega}{\omega_0} X_L \\ \dfrac{\omega}{\omega_0} X_L & 0 \end{bmatrix} \begin{bmatrix} i_d \\ i_q \end{bmatrix} + \begin{bmatrix} \dfrac{X_L}{\omega_0} & 0 \\ 0 & \dfrac{X_L}{\omega_0} \end{bmatrix} \begin{bmatrix} \dfrac{di_d}{dt} \\ \dfrac{di_q}{dt} \end{bmatrix} \tag{2.18}$$

The voltage across the capacitor:

$$\begin{bmatrix} \dfrac{dV_{Cd}}{dt} \\ \dfrac{dV_{Cq}}{dt} \end{bmatrix} = \begin{bmatrix} \omega_0 X_C & 0 \\ 0 & \omega_0 X_C \end{bmatrix} \begin{bmatrix} i_d \\ i_q \end{bmatrix} + \begin{bmatrix} 0 & \omega \\ -\omega & 0 \end{bmatrix} \begin{bmatrix} V_{Cd} \\ V_{Cq} \end{bmatrix} \tag{2.19}$$

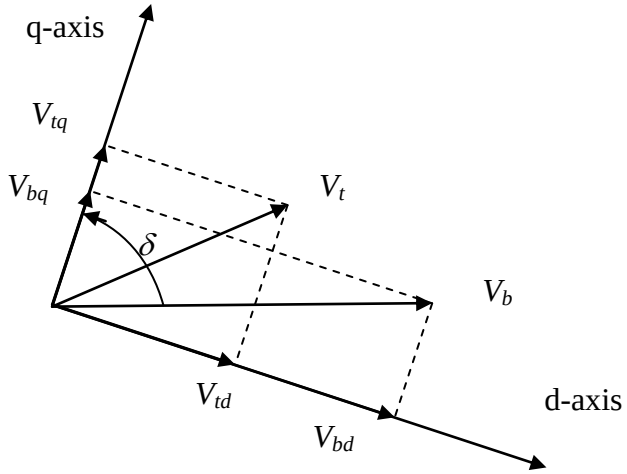

Figure 2.3: Voltage phasor diagram.

The overall equations of the transmission line can be written as

$$\begin{bmatrix} \dfrac{dV_{Cd}}{dt} \\ \dfrac{dV_{Cq}}{dt} \\ V_{td} \\ V_{tq} \end{bmatrix} = [Att] \begin{bmatrix} V_{Cd} \\ V_{Cq} \end{bmatrix} + [Rt1] \begin{bmatrix} \dfrac{di_d}{dt} \\ \dfrac{di_q}{dt} \end{bmatrix} + [Rt2] \begin{bmatrix} i_d \\ i_q \end{bmatrix} + [Btt][V_b] \tag{2.20}$$

where

$$[Att] = \begin{bmatrix} 0 & \omega \\ -\omega & 0 \\ 1 & 0 \\ 0 & 1 \end{bmatrix}$$

$$[Rt1] = \begin{bmatrix} 0 & 0 \\ 0 & 0 \\ \frac{X_L}{\omega_0} & 0 \\ 0 & \frac{X_L}{\omega_0} \end{bmatrix}$$

$$[Rt2] = \begin{bmatrix} \omega_0 X_C & 0 \\ 0 & \omega_0 X_C \\ R_L & -\frac{\omega}{\omega_0} X_L \\ \frac{\omega}{\omega_0} X_L & R_L \end{bmatrix} \qquad (2.21)$$

$$[Btt] = \begin{bmatrix} 0 \\ 0 \\ \sin\delta \\ \cos\delta \end{bmatrix}$$

In the case of an uncompensated transmission line, the impedance Xc in Equations 2.19 and 2.21 is set to zero.

2.2.3 Modeling of the excitation system

Figure 2.4 show the block diagram of the excitation system and the corresponding data are given in Appendix A [14].

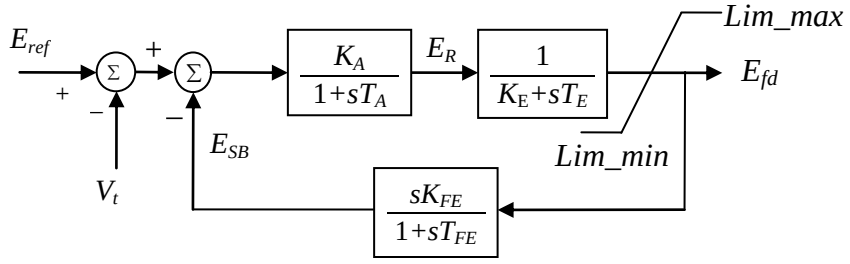

Figure 2.4: Block diagram of the excitation system.

The state-space equation of the excitation system is given by Equation 2.23

$$\left[\frac{dX_v}{dt}\right] = [At_v][X_v] + [Bt_v]\begin{bmatrix} V_t \\ E_{ref} \end{bmatrix} \tag{2.22}$$

where

$$[X_v] = \begin{bmatrix} e_{fd} & E_R & E_{SB} \end{bmatrix}^T$$

$$[At_v] = \begin{bmatrix} -\frac{K_E}{T_E} & \frac{1}{T_E}\frac{R_{fd}}{L_{ad}} & 0 \\ 0 & -\frac{1}{T_A} & -\frac{K_A}{T_A} \\ -\frac{K_E K_F}{T_E T_F}\frac{L_{ad}}{R_{fd}} & \frac{K_F}{T_F T_E} & -\frac{1}{T_F} \end{bmatrix} \tag{2.23}$$

$$[Bt_v] = \begin{bmatrix} 0 & 0 \\ -\frac{K_A}{T_A} & \frac{K_A}{T_A} \\ 0 & 0 \end{bmatrix}$$

2.2.4 Modeling of the transformer

The step up transformers' connection is DYg+30 which are the LV side connects as Delta and HV side connects as Y grounded with 30 degree compensation. Beside, the characteristics of the transformer consisting of winding resistance, winding reactance and winding impedance are supported in the model.

2.2.5 Modeling of the system loads

A constant impedance is represented for the system load. The formula, which is used in calculating the load impedances, is given by [15]:

$$Z_{Load} = \frac{|V_{Load}|^2}{P_{Load} - jQ_{Load}} \tag{2.24}$$

where

Z_{Load} = load impedance.

V_{Load} = load voltage.

P_{Load} = load real power.

Q_{Load} = load reactive power.

2.2.6 Modeling of VSC HVDC system

Figure 2.5 shows one line diagram of a VSC connected to an AC system [10]. Where, the system AC voltage is $V_S\angle 0°$, and the converter AC voltage is $V_{Sh}\angle\delta_{sh}$.

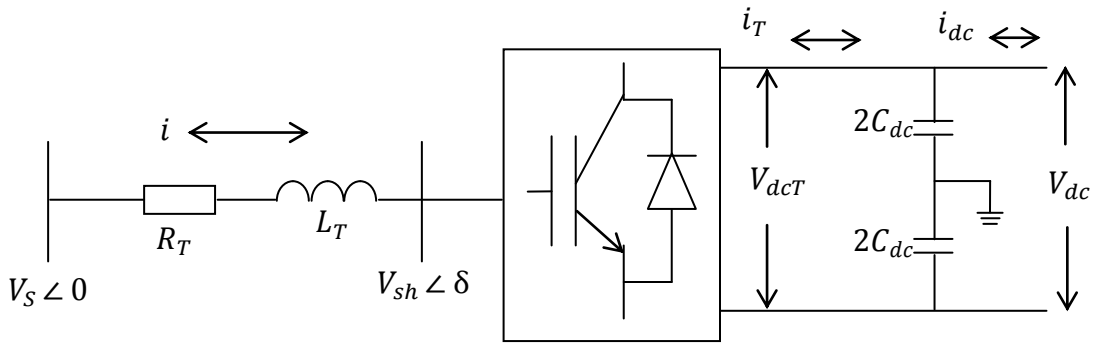

Figure 2.5: A VSC connected to an AC system.

Applying Kirchhoff's Voltage Law for the circuit in Figure 2.5, the equation is given as below

$$Vs_{abc} = L_T \frac{d}{dt} i_{abc} + Vsh_{abc} \tag{2.25}$$

Converting Equation 2.25 into dq-reference frame by applying Park's transformation [10]

$$Vs_{dq} = L_T \frac{d}{dt} i_{dq} + Vsh_{dq} \tag{2.26}$$

$$\frac{di_d}{dt} = \omega i_q + \frac{Vs_d - Vsh_d}{L_T} \tag{2.27}$$

$$\frac{di_q}{dt} = -\omega i_d + \frac{Vs_q - Vsh_q}{L_T} \tag{2.28}$$

Where, i_q and i_d are the q-axis and d-axis components of the AC system current. Equations 2.27 and 2.28 form the basis of the inner controller of VSC-HVDC.

Equation 2.29 expresses the relationship between the converter AC voltage and DC voltage

$$V_{\text{sh}}(t) = \frac{1}{2} V_{DC} M sin(\omega t + \delta) \tag{2.29}$$

Where, M is modulation index and δ is phase shift between fundamental component of converter and AC voltage and V_{DC} is DC voltage

Converting Equation 2.29 into dq-reference frame by applying Park's transformation

$$Vsh_d = \frac{1}{2} M V_{DC} cos\delta \;\; ; \;\; Vsh_{\text{q}} = \frac{1}{2} M V_{DC} \sin\delta \tag{2.30}$$

The modulation index M and phase shift δ can be derived for Equation 2.30 as below

$$M = \frac{2\sqrt{Vsh_d^2 + Vsh_q^2}}{V_{DC}}; \; \delta = \; tan^{-1}(\frac{Vsh_q}{Vsh_d}) \tag{2.31}$$

Where, Vsh_d and Vsh_q are d-axis and q-axis component of the converter AC voltage, V_{DC} is the DC voltage. The active and reactive power in dq-frame can be derived from the equation below [10]

$$P = \frac{3}{2}(Vs_d i_d + \; Vs_q i_q) \tag{2.32}$$

$$Q = \frac{3}{2}(-Vs_d i_q + \; Vs_q i_d) \tag{2.33}$$

Where, i_d and i_q are the d-axis and q-axis components of the AC system current.

The power on DC site is given by

$$P_{DC} = \; i_T Vdc_T \tag{2.34}$$

Where, i_T is the current flowing through the DC terminal and Vdc_T is voltage at the DC terminals. The current i_T is given by:

$$i_T = \; C_{dc} \frac{dVdc_T}{dt} + \; i_{dc} \tag{2.35}$$

Where, i_{dc} is current flowing through DC overhead cables. If the losses are neglected, Equation 2.36 is derived from Equations 2.32 and 2.34.

$$\frac{3}{2}\left(Vs_d i_d + Vs_q i_q\right) = i_T Vdc_T \tag{2.36}$$

Equation 2.37 below is derived from Equations 2.34 and 2.35.

$$\frac{dVdc_T}{dt} = \frac{3}{2}\frac{Vs_d i_d}{Vdc_T C_{dc}} + \frac{3}{2}\frac{Vs_q i_q}{Vdc_T C_{dc}} - \frac{i_{dc}}{C_{dc}} \tag{2.37}$$

VSC-HVDC model in EMTP-RV controls the active and reactive power by applying the vector control strategy. Normally, the modulation index M and phase shift δ are correlated and they can not be controlled independently due to the coupling between electrical quantities (voltage and current). In case of vector control strategy, "the synchronous of dq-reference frame vectors using PLL block is done in such a way that the d-axis is in phase with phase A voltage vector, so Vs_d = Vs and Vs_q = 0" [10]. Therefore, the Equations 2.32 and 2.33 become

$$P = \frac{3}{2}(Vsi_d), Q = -\frac{3}{2}(Vsi_q) \tag{2.38}$$

Assuming constant AC source voltage, the vector control strategy allows the active and reactive power to be controlled independently through i_d and i_q which are the d-axis and q-axis components of AC system current (Equation 2.39). This control mechanism is also the basis of the outer control block.

$$i_{dref} = \frac{2}{3}\left(\frac{P_{ref}}{V_S}\right), i_{qref} = -\frac{2}{3}\left(\frac{Q_{ref}}{V_S}\right) \tag{2.39}$$

2.2.7 Modeling of the VSC HVDC link for load flow studies

For load flow studies, each converter station of the VSC HVDC link is represented by a complex voltage source $\boldsymbol{V}_{sh}$ behind its transformer impedance Z_{sh}. These two synchronous voltage sources represent the fundamental Fourier-series component of the switched voltage waveforms at the AC converter terminals of the VSC HVDC link. A VSC HVDC link installed between buses "*E*" and "*B*" can, therefore, be modeled at steady-state as shown in Figure 2.6. The two shunt impedances are assumed to be purely inductive. The total real power injected to

the power system by the two voltage sources is equal to zero at steady-state. However, there is a real power exchange between the two sources. For load flow studies, the two-voltage source model of the VSC HVDC link is converted into two power injections as shown in Figure 2.7.

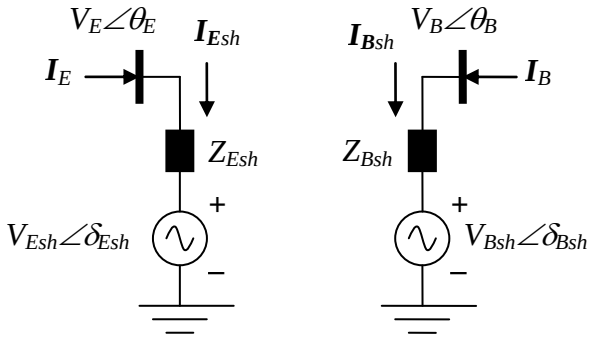

Figure 2.6: VSC HVDC link equivalent circuit for load flow studies and steady-state analysis.

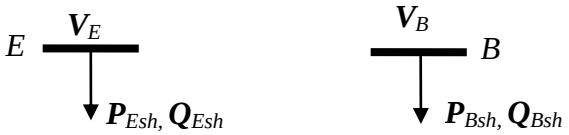

Figure 2.7: The VSC-based BtB injected power model.

The constraining load flow equation for the active power through the VSC HVDC link at steady-state is expressed mathematically as:

$$\mathrm{Re}\left\{V_{Esh}I_{Esh}^{*}+V_{Bsh}I_{Bsh}^{*}+P_{rec\_loss}+P_{inv\_loss}+P_{DCline\_loss}\right\}=0 \quad (2.40)$$

2.2.8 Modeling of the DFIG wind turbine

The basic configuration of a DFIG wind turbine is shown in Figure 2.8, where the stator of the induction machine is directly connected to the grid while a back-to-back (BtB) partial-scale power converter (25% to 30% of the generator rating) connects its wound-rotor to the grid. The BtB converter consists of two voltage-sourced converters (Rotor-Side Converter (RSC) and Grid-Side Converter (GSC)) and a common dc bus. The mathematical model of the DFIG wind turbine can be summarized as follows [19]-[24]:

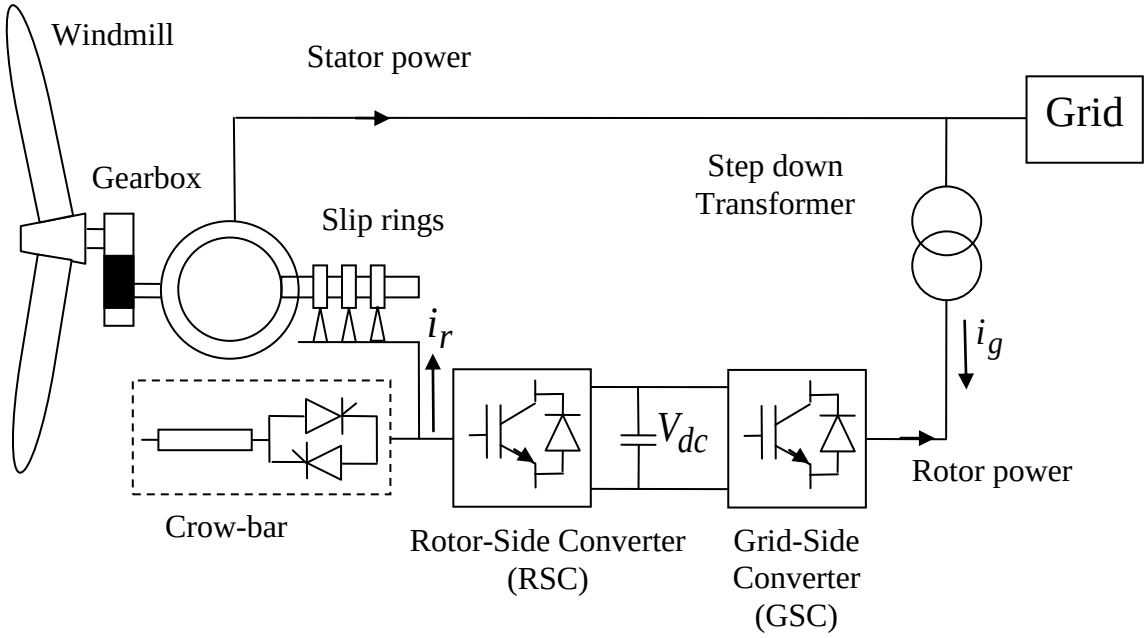

Figure 2.8: Schematic diagram of a DFIG wind turbine.

The dynamic output mechanical torque of the wind turbine is expressed as

$$T_m = \frac{1}{2}\rho \mathrm{A} R C_p V_\omega^2 / \lambda \tag{2.41}$$

Where ρ is the air density (kgm^{-3}), A is the blade sweep area (m^2), R is the rotor radius of wind turbine (m), and V_ω is the wind speed (m/s). C_p is the power coefficient of the blade which is a function of the blade pitch angle θ and the tip speed ratio λ according to the following equation:

$$C_p = \frac{1}{2}\left(\frac{RC_f}{\lambda} - 0.022\theta - 2\right) e^{-0.255\frac{RC_f}{\lambda}} \tag{2.42}$$

Where C_f is the wind turbine blade design constant and the tip speed ratio λ is given by

$$\lambda = \frac{\Omega_m R}{V_\omega} \tag{2.43}$$

Where Ω_m is the mechanical angular velocity (rad/s).

The power rotating speed, wind speed and the pitch angle relationships are illustrated in Figure 2.9.

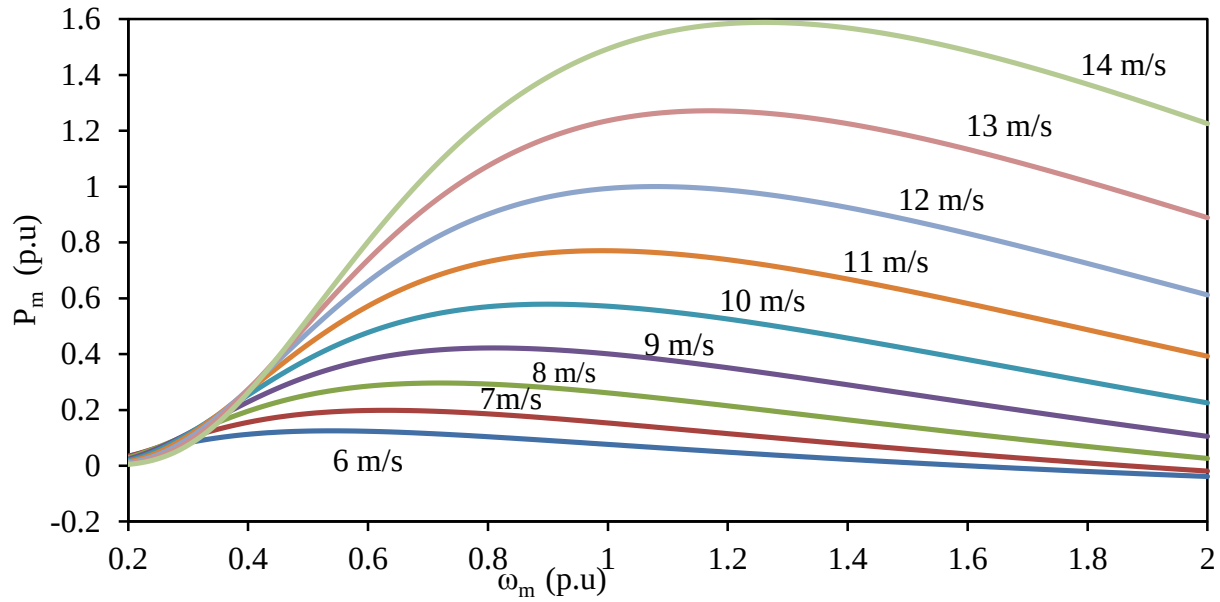

Figure 2.9: Mechanical power, rotor speed and wind speed relationships.

Figure 2.10 shows the equivalent circuit of a DFIG in the synchronous qd reference frame, where the $q-$axis leads the $d-$axis by 90^{o}. The stator and rotor voltage equations in qd reference frame can be obtained as follows:

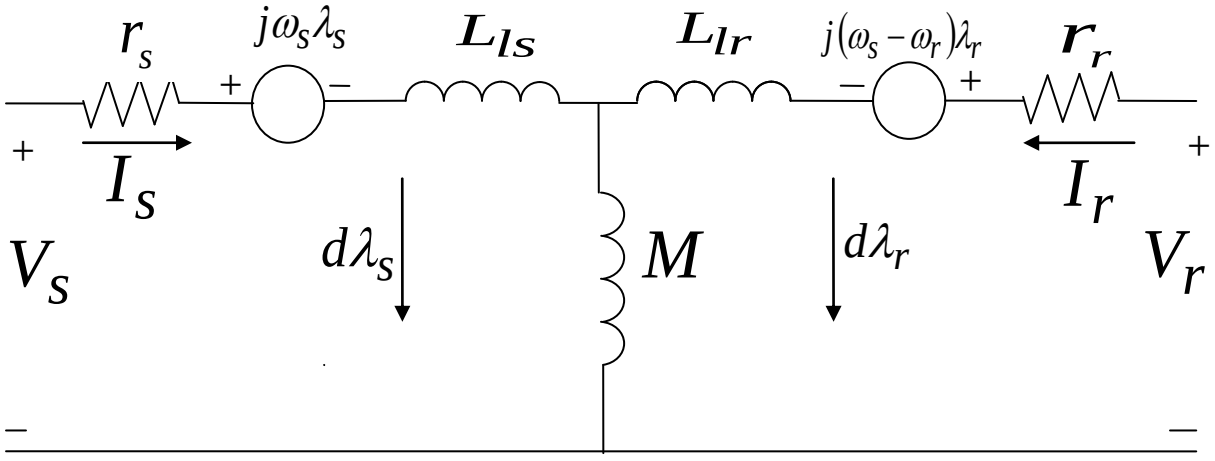

Figure 2.10: Equivalent circuit of the DFIG.

$$\begin{cases} V_s = r_s I_s + j\omega_s \lambda_s + \dfrac{d\lambda_s}{dt} \\ V_r = r_r I_r + j(\omega_s - \omega_r)\lambda_r + \dfrac{d\lambda_r}{dt} \end{cases} \tag{2.44}$$

where $V_s = v_{qs} - j\,v_{ds}$ and $V_r = v_{qr} - j\,v_{dr}$. The flux linkage expressions are given as follows:

$$\begin{cases} \lambda_s = L_s I_s + M\, I_r \\ \lambda_r = L_r I_r + M\, I_s \end{cases} \tag{2.45}$$

where $L_s = L_{ls} + M$, $L_r = L_{lr} + M$, $\lambda_s = \lambda_{qs} - j\lambda_{ds}$, $\lambda_r = \lambda_{qr} - j\lambda_{dr}$, $I_s = i_{qs} - j\,i_{ds}$ and $I_r = i_{qr} - j\,i_{dr}$.

From Equations 2.44 and 2.45, a set of differential equations with stator and rotor currents as state variables, stator and rotor voltages as inputs can be established. While the rotor voltages are determined by RSC control scheme, the stator voltages are determined by the network interface.

The electromagnetic torque T_e can be expressed as follows:

$$T_e = \lambda_{qm} i_{dr} - \lambda_{dm} i_{qr} \tag{2.46}$$

Where, λ_{qm} and λ_{dm} are, respectively, the $q-$ and $d-$axes magnetizing flux linkages defined as

$$\lambda_{qm} = \lambda_{qs} - i_{qs} L_{ls} \tag{2.47}$$

$$\lambda_{dm} = \lambda_{ds} - i_{ds} L_{ls}. \tag{2.48}$$

2.3 Modeling of SaskPower North and South Systems for Dynamic Studies of the Integrated System

The two hydro generating stations of SaskPower North system, G_N1 and G_N5 are rated at 25 MVA and 150.8 MVA respectively. Between these two generating stations which are 650 km apart are two load centers at buses N2 and N3. Manitoba grid is connected to SaskPower North system at bus N6 as shown in Figure 2.11. Transmission lines voltage is 138 kV.

Only the Northern part of SaskPower South system is modeled. This is due to the fact that the Northern part which has a high density of generation could represent reasonably the South system as the dynamic studies are focused on the tie-line performance. Therefore, modeling the entire SaskPower South system is unnecessary. As it can be seen from Figure 2.11,

there are four generating stations in the modeled Saskpower South system; G_S1, G_S2, G_S4 and G_S6 with rated capacity of 192 MVA, 147.1 MVA, 192 MVA and 231.6 MVA respectively. There are also two load centers located at buses S3 and S5. A DFIG-based wind farm comprising 50 × 1.5 MW DFIG wind turbines is also connected to SaskPower South system at bus S4. The operating wind speed and power output of the wind farm are given in Table 2.1. Transmission line voltages in SaskPower South system are 138 and 220 kV.

The data of the modeled SaskPower North and South generating stations are given in Appendix A [2] and the data of the system load are given in Table 2.2. Moreover, since generators are required to operate above minimum levels, some loads are added to some generator busses. The electrical parameters of 138 and 220 kV transmission lines are typical transmission lines data [2]. The modeled SaskPower integrated system incorporating an AC tie-line is shown in Figure 2.12. It is worth noting here that in order to carry out the time-domain simulation studies, the two large systems representing Manitoba grid connections, shown in Figure 2.10, are replaced with a single large system and a virtual transmission line between buses N6 and S7.

Table 2.1: DFIG-based wind farm operating speed and power output.

Wind farm	Operating speed and output power
DFIG Wind farm	Wind speed = 11 m/s, ≈ 75 MW

Table 2.2: System loads.

Load	MW	Mvar
L_{N2}	32	24
L_{N3}	28	21
L_{S3}	150	50
L_{S5}	90	40

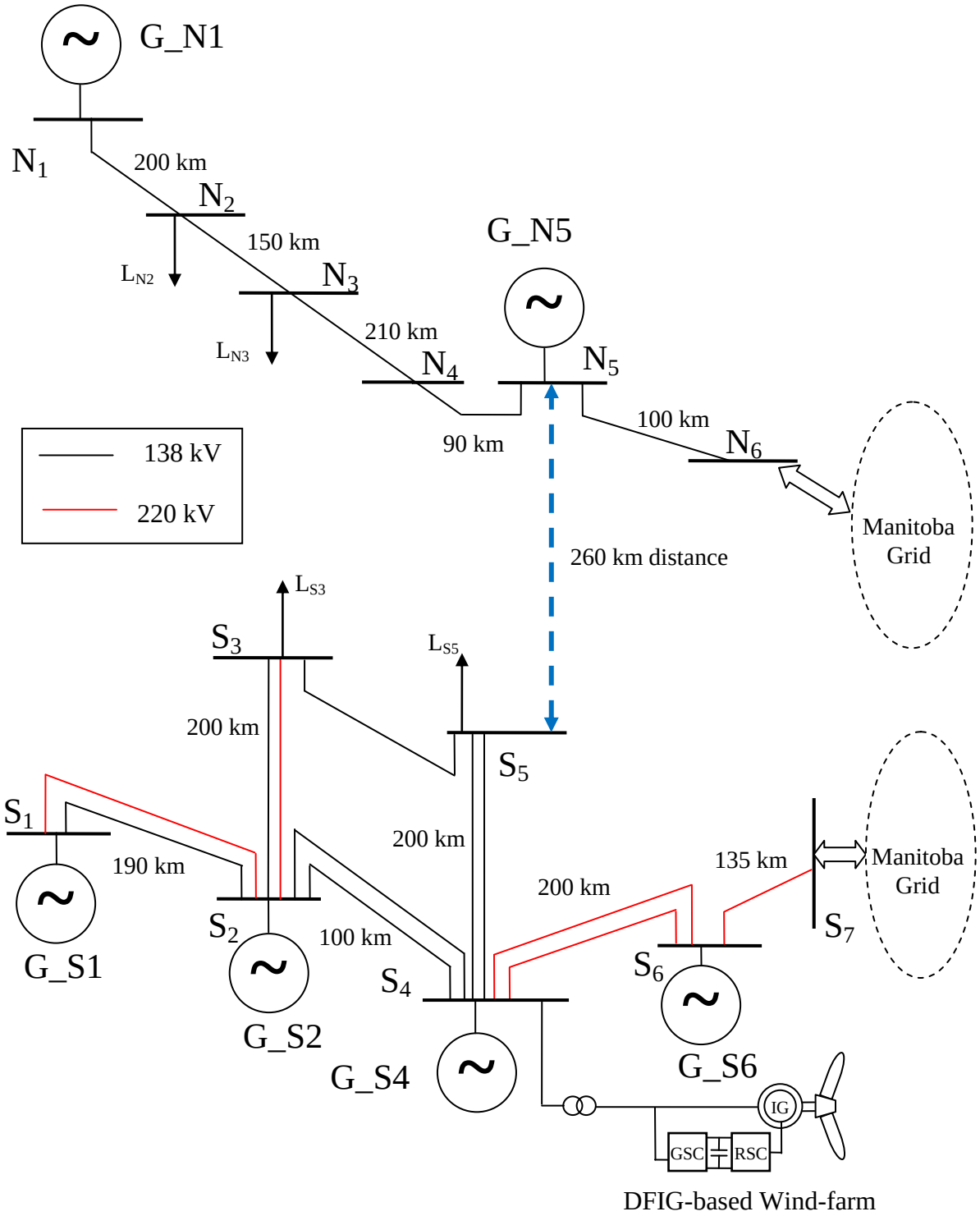

Figure 2.11: Modeling of SaskPower North and South systems.

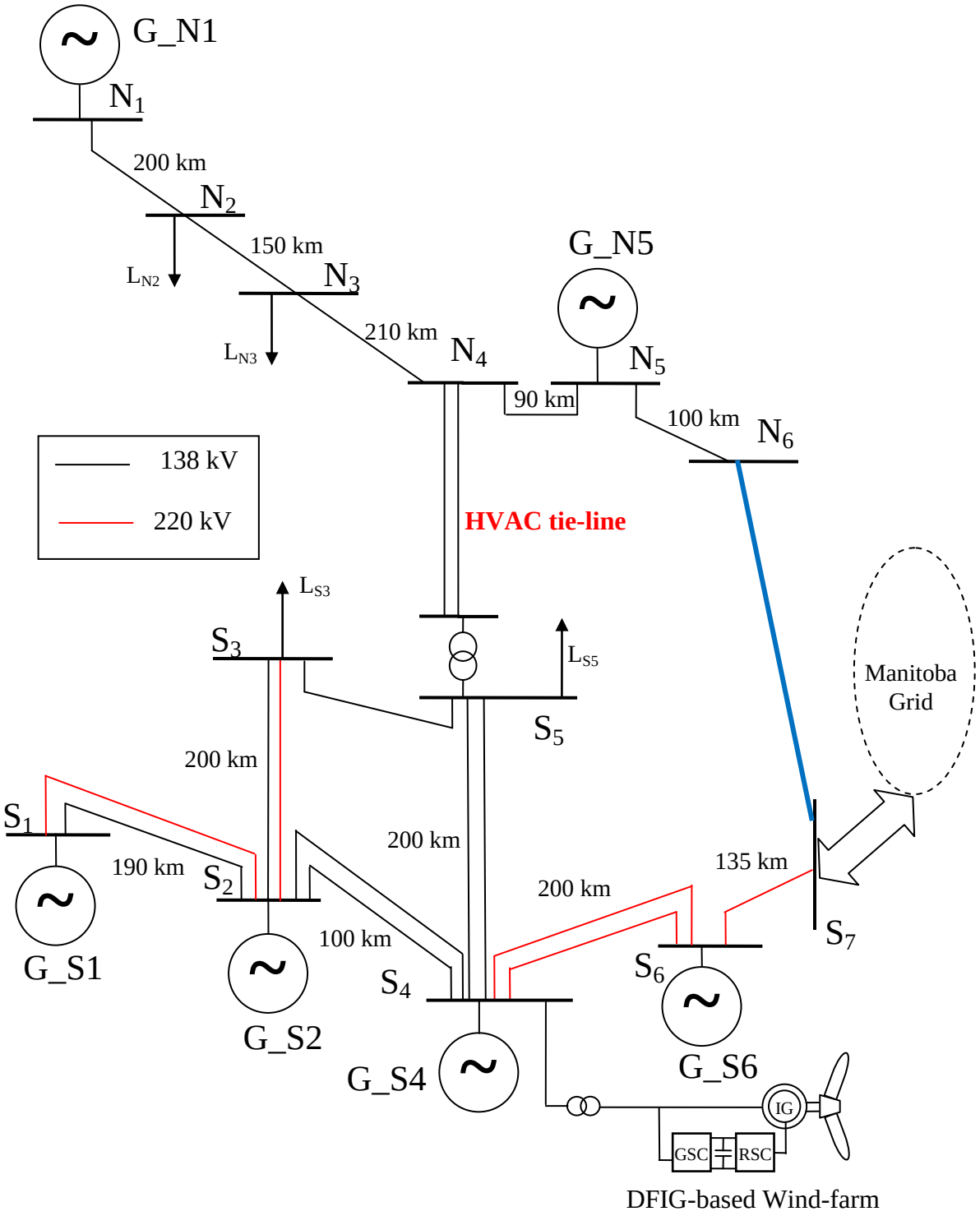

Figure 2.12: SaskPower integrated system incorporating an AC tie-line.

2.4 A Sample Case Study

The ElectroMagnetic Transient Program (EMTP-RV) is used in the studies conducted in this thesis to obtain the time-domain simulations and, therefore, the system components are modelled in it. Due to the nature of the EMTP-RV initialization process, the time-domain simulations start at t = 10 seconds. Moreover, system faults are assumed to occur at t = 11 seconds.

Figure 2.13 illustrates transient time responses of SaskPower integrated system incorporating the 260 km, 138 kV double-circuit tie-line during and after clearing a three-cycle, three-phase fault on transmission line N6-S7 (transmission line between buses N6 and S7). This case study is designated as the "base case" and is used for comparison with other case studies.

The physical explanation of tripping the virtual transmission line N6-S7, shown in Figure 2.12, is that bus N6 has lost its interconnection with the Manitoba grid (Figure 2.11).

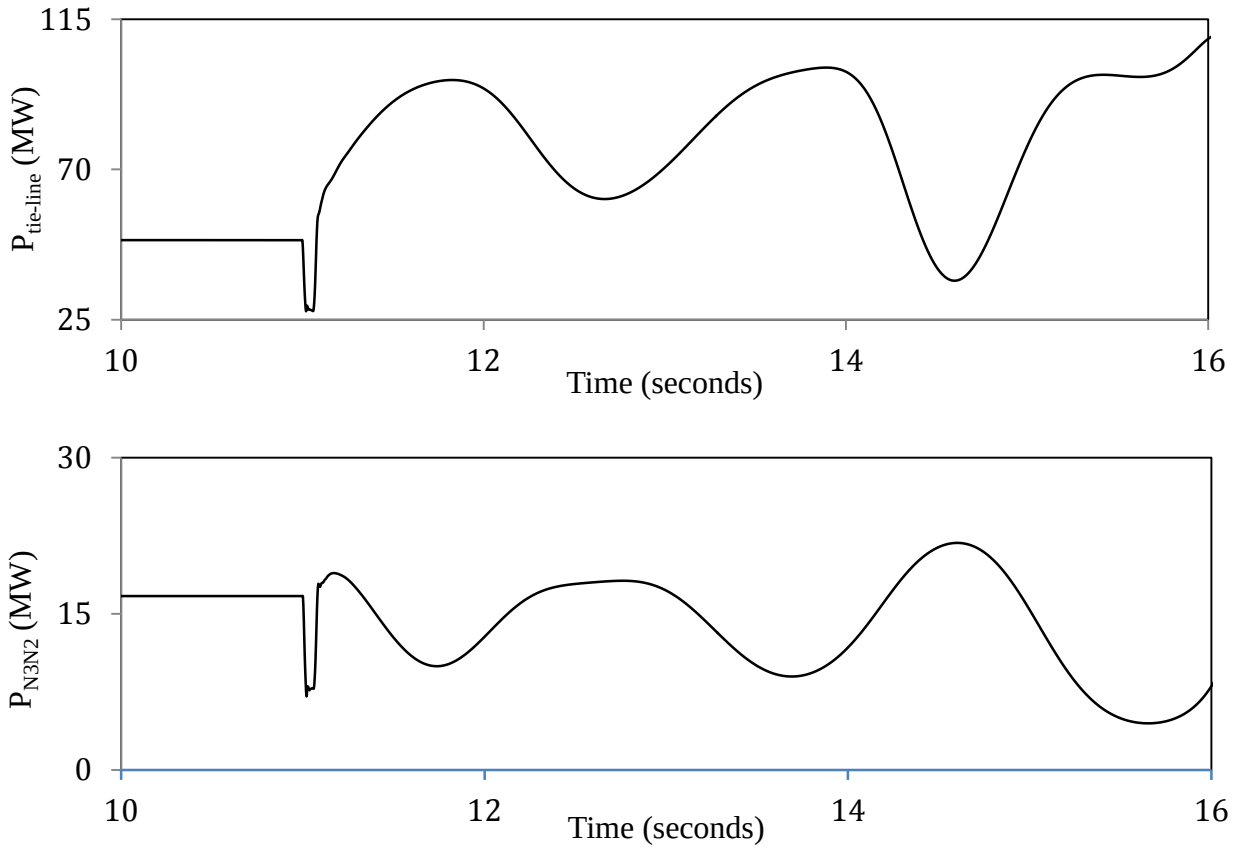

Figure 2.13: Transient time responses of the power system during and after clearing a three-cycle, three-phase fault on transmission line N6-S7 (with the 260 km, 138 kV double-circuit tie-line).

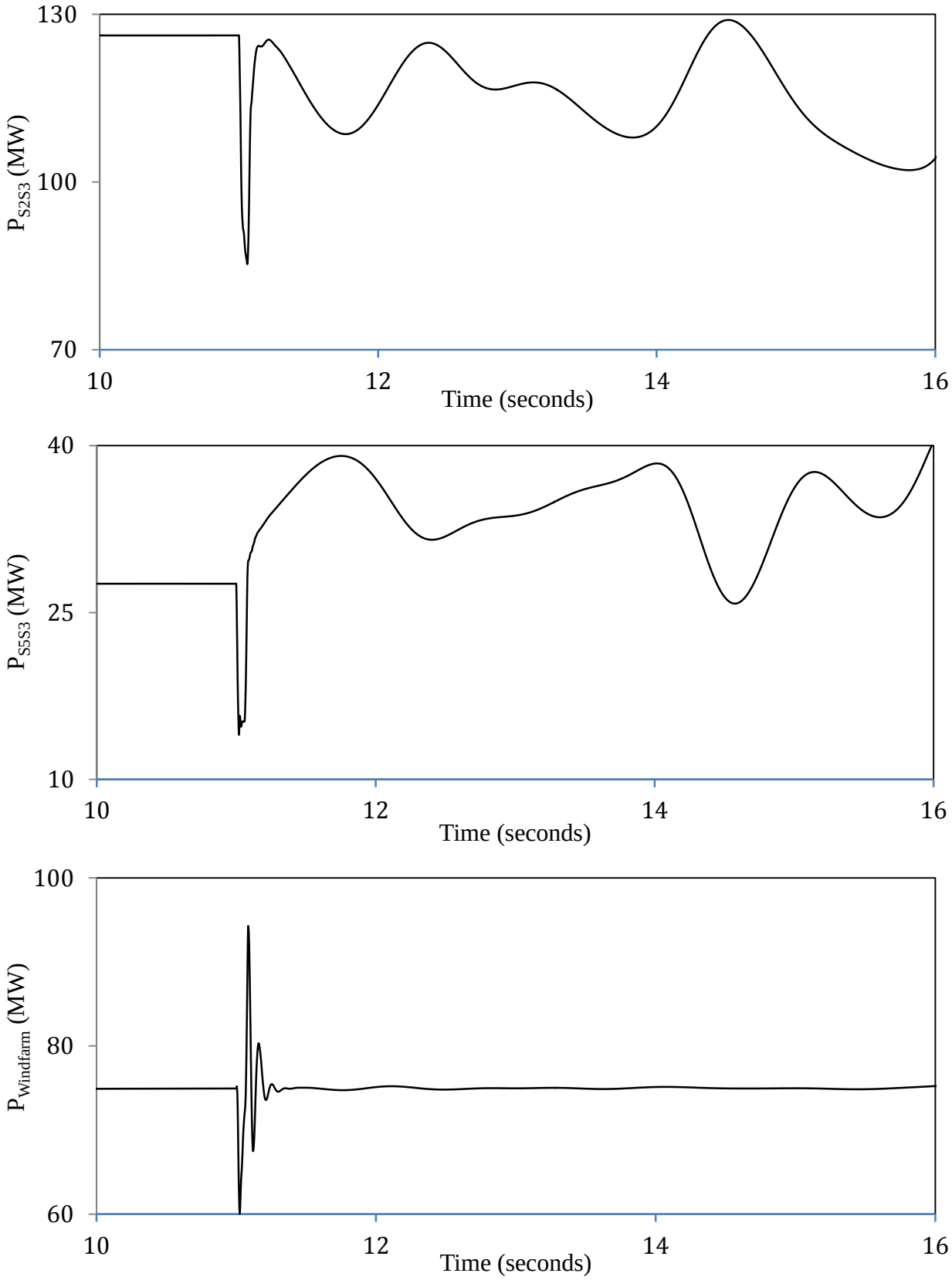

Figure 2.13: continued.

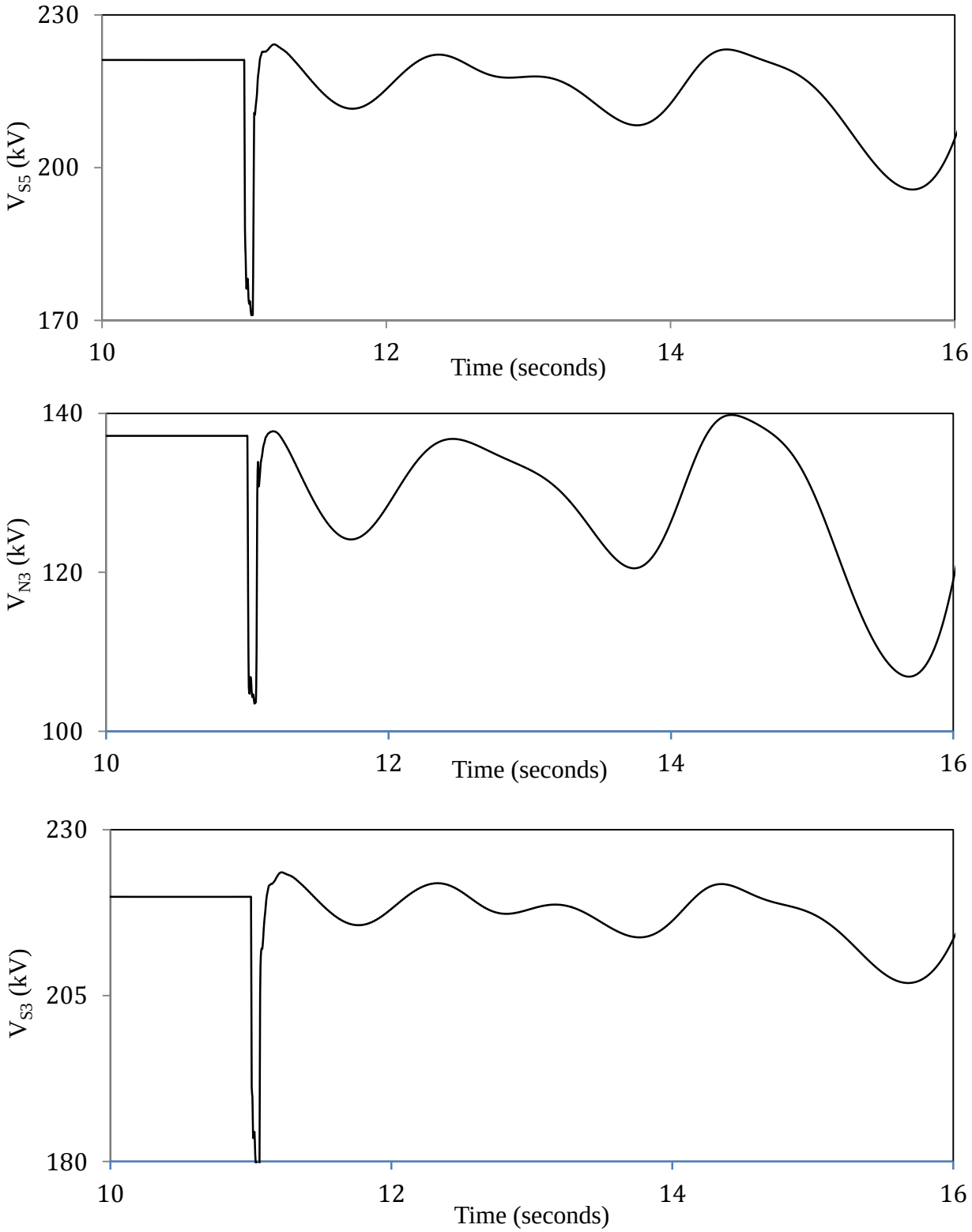

Figure 2.13: continued.

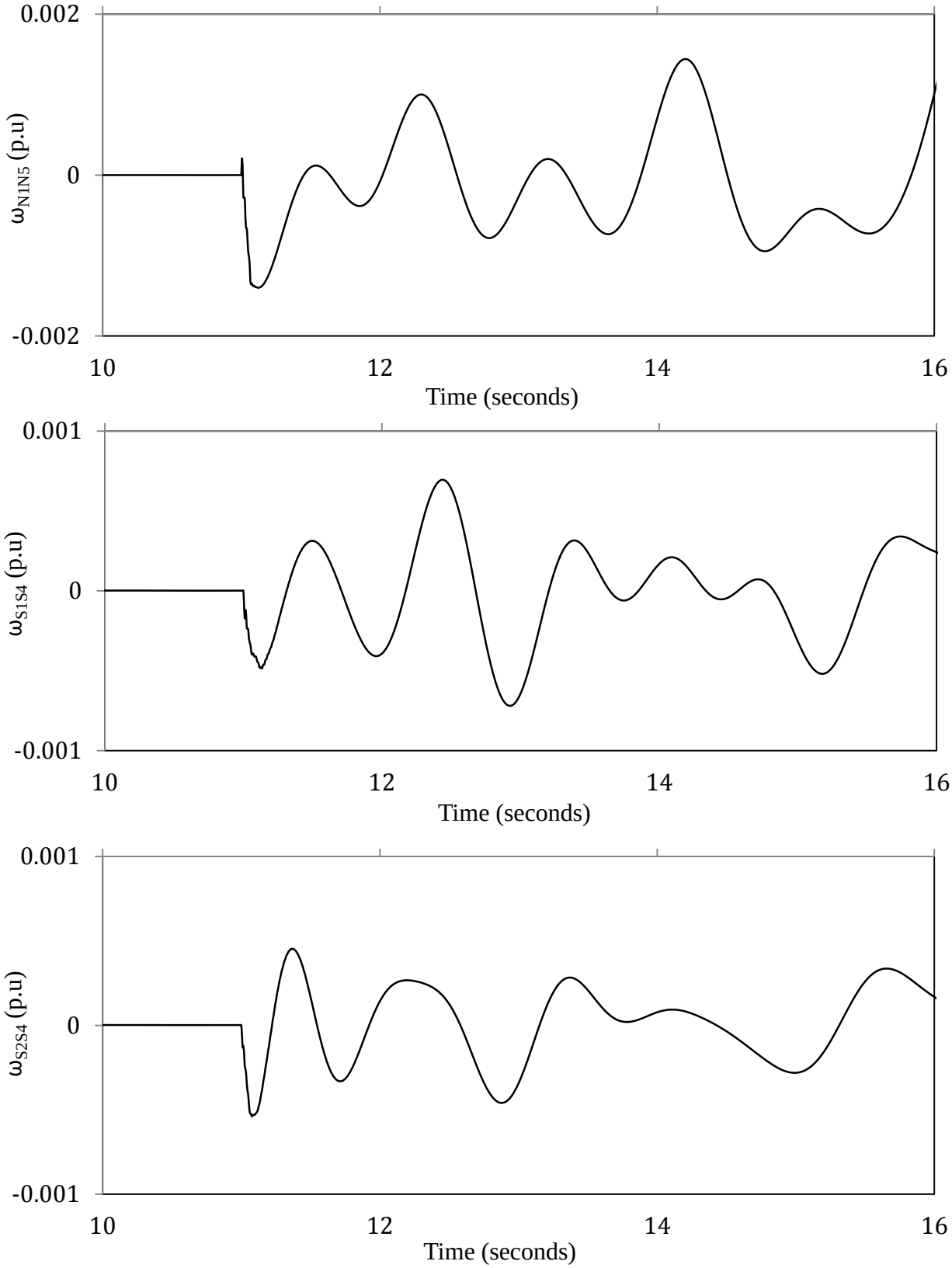

Figure 2.13: continued.

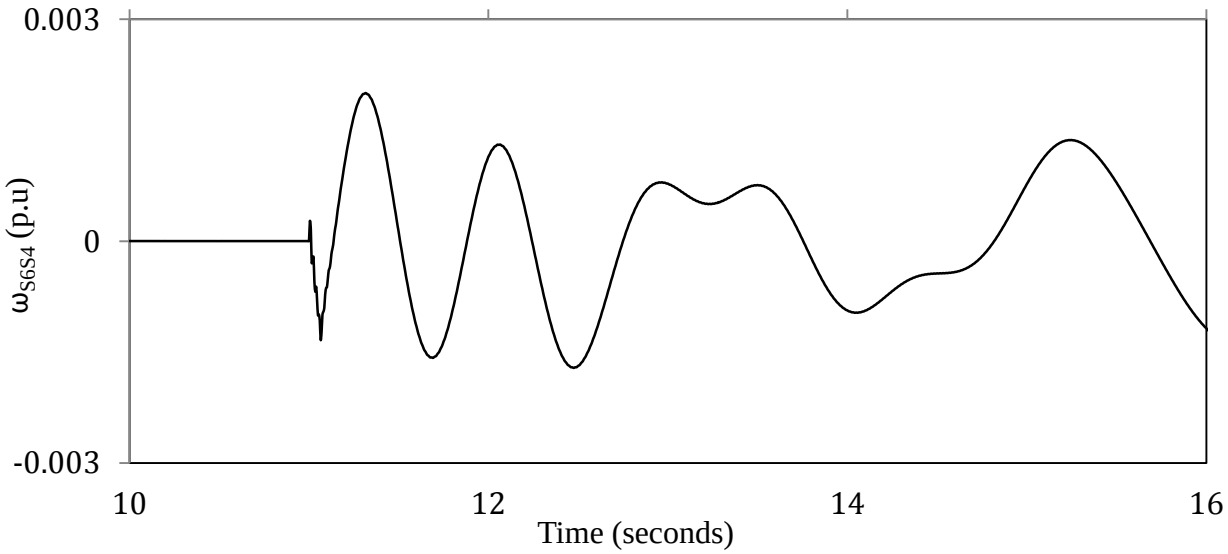

Figure 2.13: continued.

The following observations can be made from examining Figure 2.13:

1. As expected, 50 MW is transmitted through the tie-line.
2. After fault clearing the system bus voltages, transmission line real power flows and generator speed deviations experience severe low-frequency oscillations. Failing to reach a new steady-state condition, the system has lost its stability.
3. The DFIG-based wind farm is stable after fault clearing delivering its rated power of 75 MW.

2.5 Summary

The mathematical models of various components of the system under study are presented in this chapter. A detailed description of SaskPower North and South system models suitable for studying the dynamic performance of the HVAC and HVDC interconnections are also presented. Moreover, the results of digital time-domain simulations of a case study of the integrated system incorporating the HVAC interconnection during a three-phase fault are also presented.

Chapter 3

SYSTEM LOAD FLOW STUDIES AND THE CONTROL STRATEGY OF THE VSC HVDC LINK AND ITS POWER OSCILLATIONS DAMPING SUPPLEMENTAL CONTROLLER

3.1 Introduction

In this chapter, the load flow studies of SaskPower North and South systems as well as of the integrated system incorporating the HVAC 138 kV double-circuit tie-line and the ± 110 kV VSC HVDC link are presented. The basic control strategy of VSC HVDC transmission system is also discussed. Furthermore, the general structure of the VSC HVDC POD supplemental controller and an insight on the selection of its stabilizing signal are also presented.

3.2 System Load Flow Studies

As mentioned in Chapter 1, it is planned to transmit 50 MW from SaskPower North system to its South system through a "new" 260 km tie-line. With the new tie-line, it is required to still be able to keep the imported/exported power from the Manitoba grid to a minimum.

The results of the load flow studies (the bus voltages and the real power flow) for SaskPower North and South systems are shown in Figures 3.1 and 3.2 respectively. It can be seen from these figures that the North system is exporting 2 MW to the Manitoba grid while there is no power exchange between the South system and the Manitoba grid. It can also be seen from Figure 3.1 that the North system load is about 60 MW which would allow 50 MW of the extra generating capacity of G_N5 to be transmitted to the South system through the new tie-line.

Figure 3.3 shows the results of the load flow studies (the bus voltages and the real power flow) for SaskPower integrated system incorporating the 260 km, 138 kV double-circuit AC tie-line. It can be seen from this figure that the new tie-line results in changing the loop power flow profile as the power exported from the North system to the Manitoba grid is increased to 39 MW

and the South system is now importing 38 MW although the net power exchange with Manitoba grid is unchanged significantly.

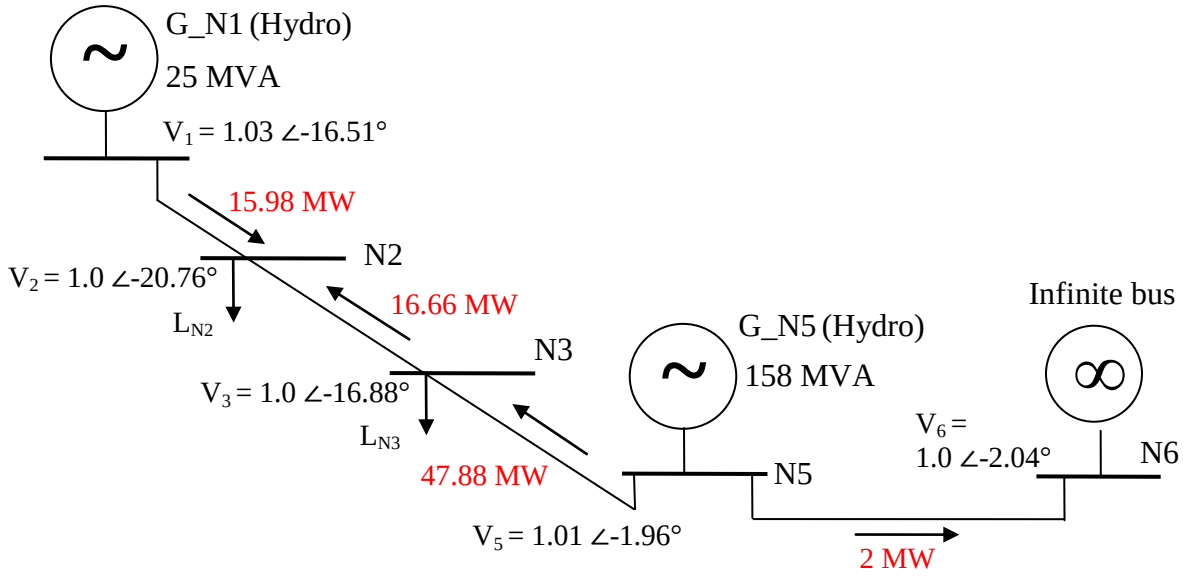

Figure 3.1: SaskPower North system load flow results.

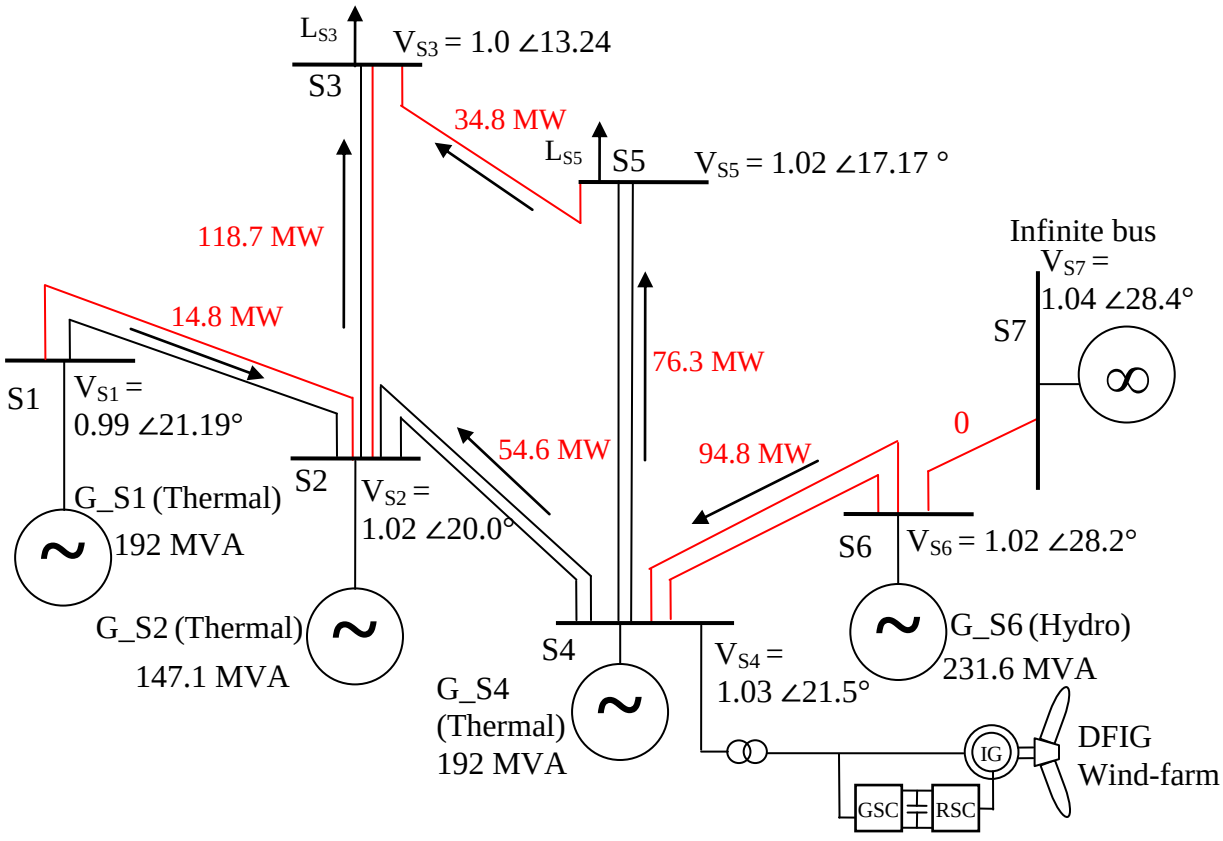

Figure 3.2: SaskPower South system load flow results.

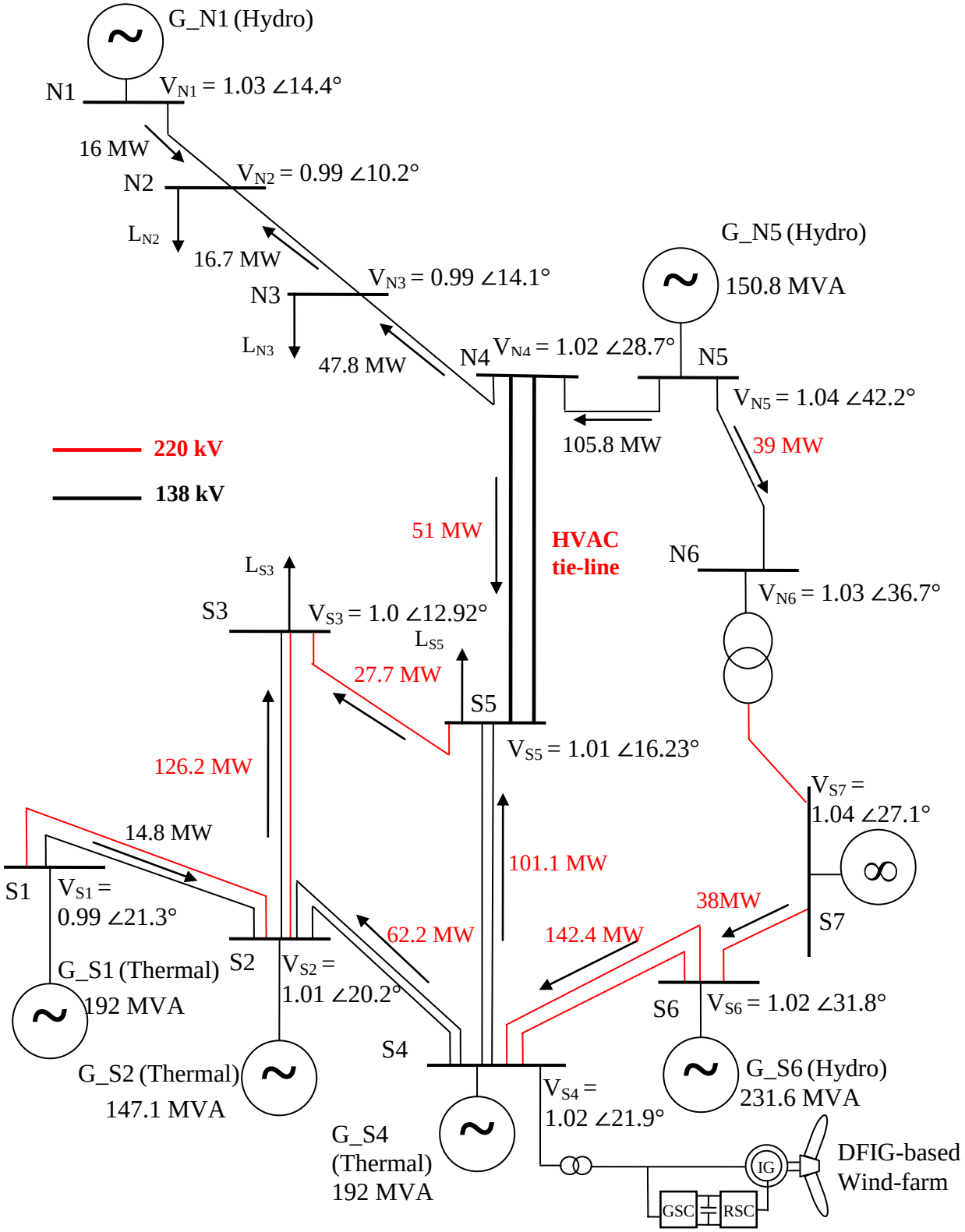

Figure 3.3: Load flow results of SaskPower integrated system incorporating a HVAC interconnection.

Figure 3.4 shows the results of the load flow studies (the bus voltages and the real power flow) for SaskPower integrated system incorporating the 260 km, ± 110 kV, VSC HVDC link. The comparison between this figure and Figures 3.1 and 3.2 shows that the new tie-line does not result in any appreciable changing in the loop power flow profiles of the North and South systems. It can also be seen from Figure 3.4 that the net power exchange with the Manitoba grid is zero.

3.3 VSC HVDC Control Strategy

Each VSC HVDC converter is able to control the real and reactive power independently by simultaneously regulating the amplitude and phase angle of the fundamental component of the converter output voltage. This is achieved utilizing vector control techniques. Vector control allows decoupled control of both real and reactive power. The idea is to use a rotating reference frame based on an AC flux or voltage and then to project the currents on this rotating frame. Such projections are usually referred to as the d- and q- components of their respective currents. For flux-based rotating frames, changes in the q- component lead to real power changes, while changes in the d- component lead to reactive power changes. In voltage-based rotating frames (90 degrees ahead of flux-based frames), the effect is the opposite.

Figure 3.5 shows a general control scheme for a VSC HVDC converter station [10]. In such a scheme, the converter operates in the stator voltage reference frame. The q-axis current is used to control the reactive power (and the AC voltage) while the d-axis current is used for active power control (and the DC voltage). As illustrated in Figure 3.5, the converter is controlled by a two-stage controller. The first stage (inner current control loop) consists of a very fast current controller regulating the currents to references values that are specified by slower power controllers (outer power control loop). The control strategy is applied for both the inverter and the rectifier converter stations where converter implements all four controlled variables, real power control P, reactive power control Q, DC voltage control V_{dc} and AC voltage $V_{Sh}\angle\delta_{sh}$.

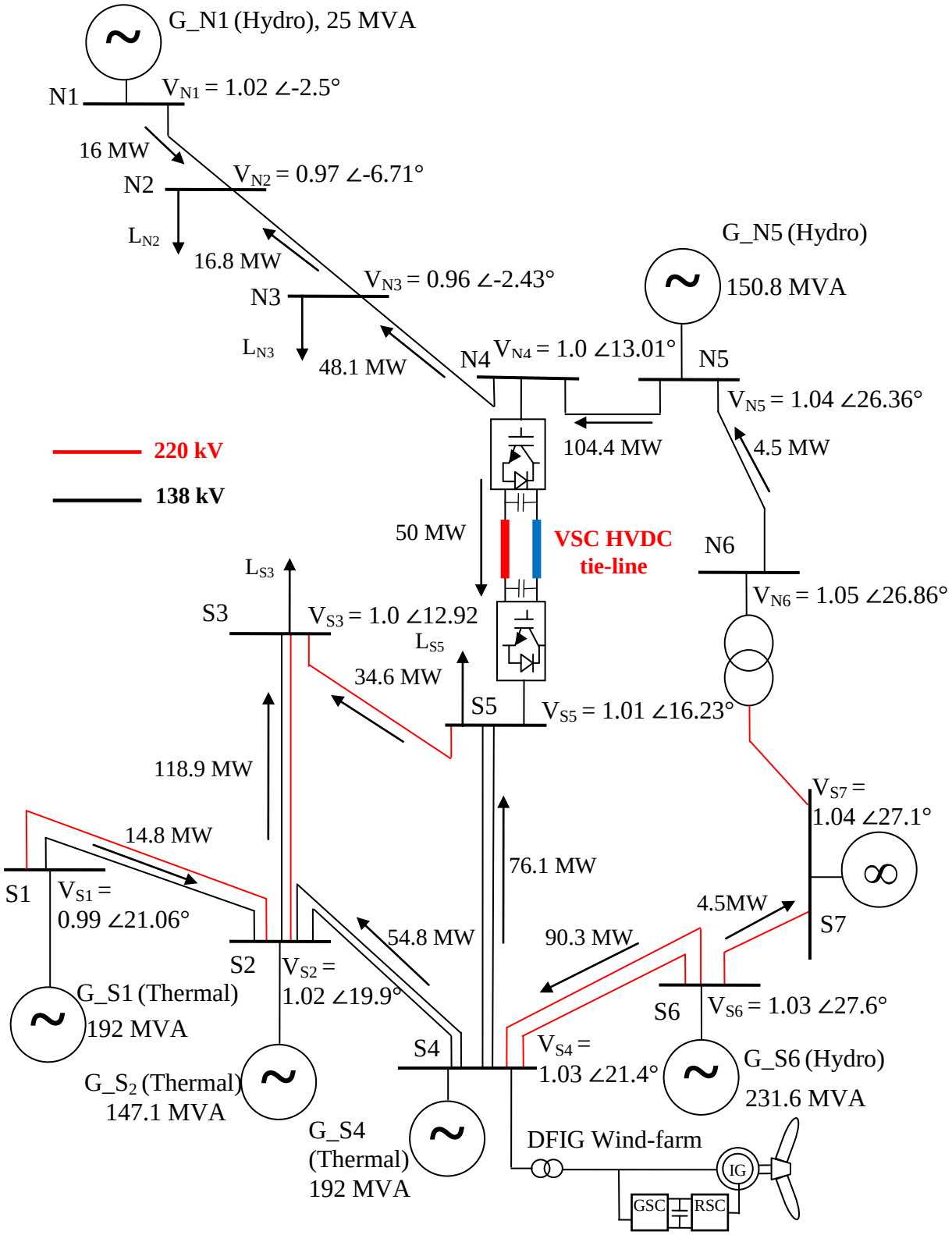

Figure 3.4: Load flow results of SaskPower integrated system incorporating a VSC HVDC interconnection.

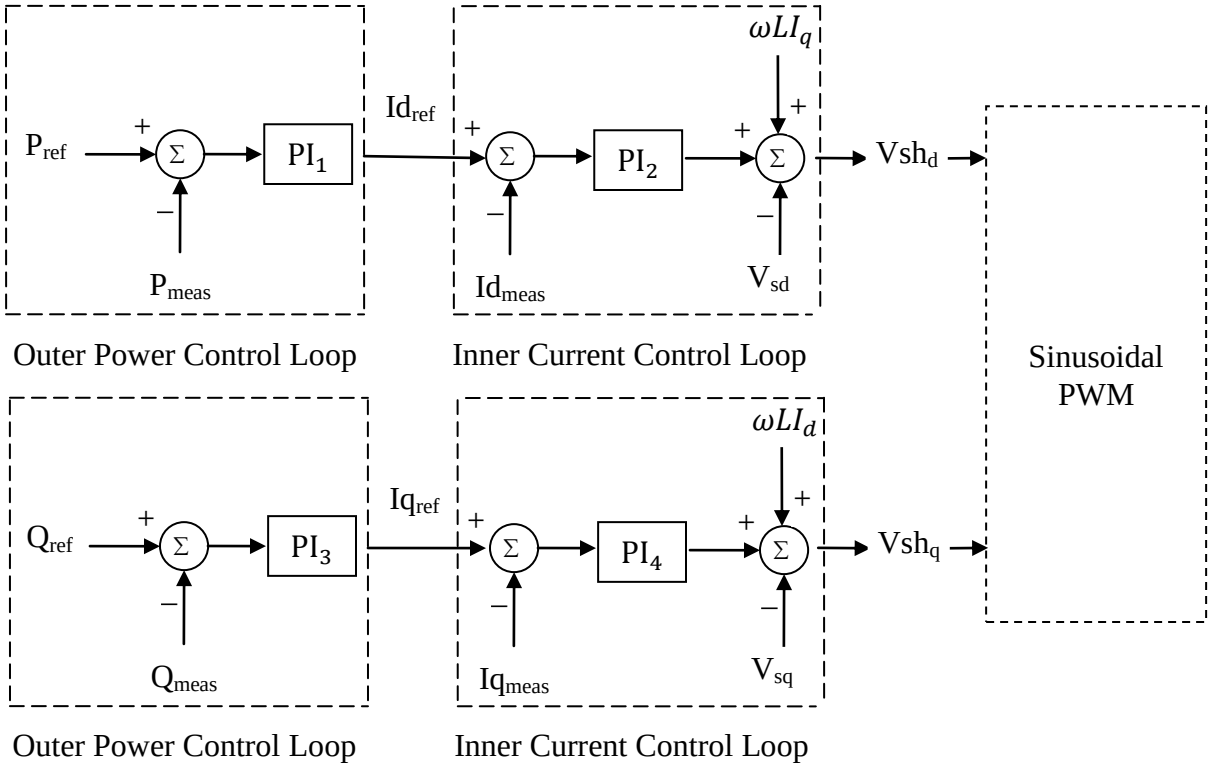

Figure 3.5: Schematic diagram of a general control scheme of a VSC-HVDC converter station.

3.4 VSC HVDC Power Oscillations Damping Supplemental Controller

Power Oscillations Damping (POD) supplemental controller contributes to the positive system damping by generating a damping torque which is in phase with the q-axis component of the AC system current I_q. This is accomplished by introducing a supplementary damping (stabilizing) signal in the inner current controller loop of the VSC HVDC converter. Figure 3.6 shows a general structure block diagram of a POD supplemental controller [17], [18]. The wash-out block is a high-pass filter that eliminates the average and extracts the oscillating part of the input signal. The phase compensation blocks are linear lead-lag networks that provide the desired phase shift at the oscillations frequency.

3.4.1 Selection of the stabilizing signal

The selection of the appropriate input (stabilizing) signal is an important issue in the design of an effective controller as it must yield correct control action when a severe fault occurs

in the system. The commonly used input signals for the POD supplemental controller are the generator rotor speeds, power angles and ac transmission line real power flows or a combination of those signals.

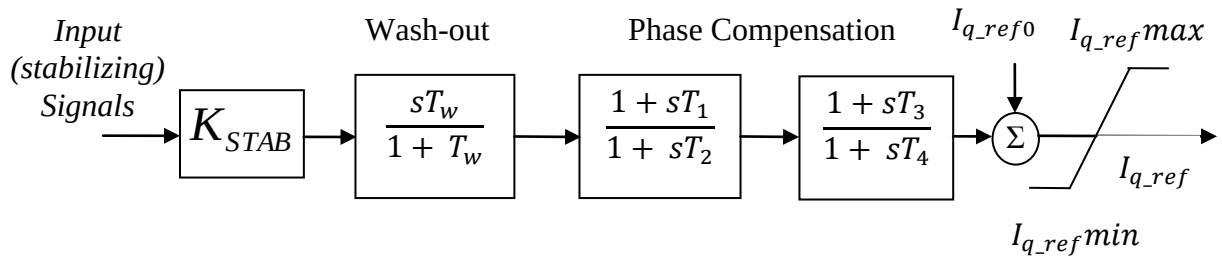

Figure 3.6: Structure of the VSC HVDC POD supplemental controller.

From the general block diagram of the POD supplemental controller, shown in Figure 3.6, in order to damp the low-frequency oscillations, the input signal must satisfy the two following criteria:

1. The input signal must have the harmonic component (frequency) of the oscillations that need to be damped.

2. The input signal must have a sufficient damping torque.

Figure 3.7 illustrates the transient time response of bus S5 voltage during and after clearing a three-cycle, three-phase fault on transmission line N6-S7. As it can be seen from this figure, although the bus voltage exhibits a good damping, its spike after fault clearing could be reduced with the VSC HVDC POD supplemental control. It can also be seen from Figure 3.7 that the frequency of the low-frequency oscillations is around 0.67 Hz. Therefore, the stabilizing signal must have a frequency close to 0.67 Hz and a sufficient damping torque. In this regard, four stabilizing signals, namely G_S1 speed (ω_{S1}), G_S4 speed (ω_{S4},), G_N5 load angle measured with respect to G_S4 load angle (δ_{N5S4}) and G_N1 load angle measured with respect to G_S4 load angle (δ_{N1S4}) are examined. The transient time responses of these four signals during and after clearing a three-cycle, three-phase fault on transmission line N6-S7 are illustrated in Figures 3.8 and 3.9. It can be seen from these figures that the frequencies of G_S4 speed (ω_{S4},) and bus S5 oscillations are very close. Therefore, ω_{S4} is selected as the stabilizing signal.

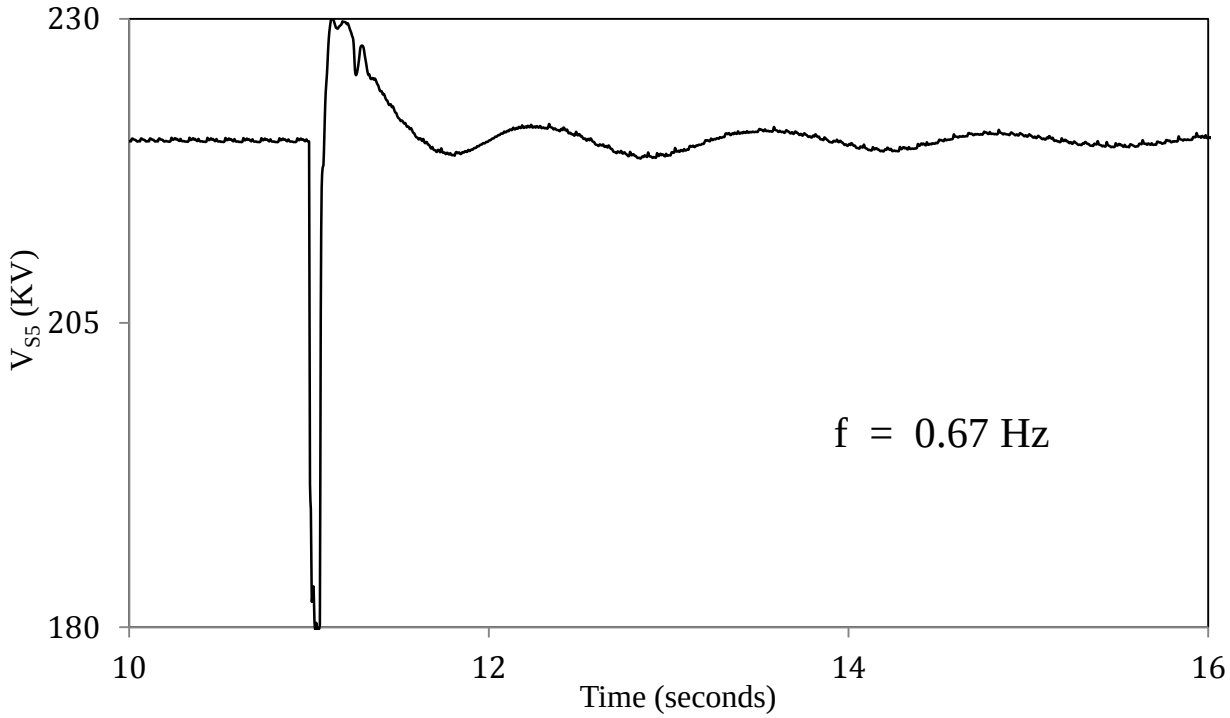

Figure 3.7: Transient time response of bus S5 voltage during and after clearing a three-cycle, three-phase fault on transmission line N6-S7 (with only the VSC HVDC main controller).

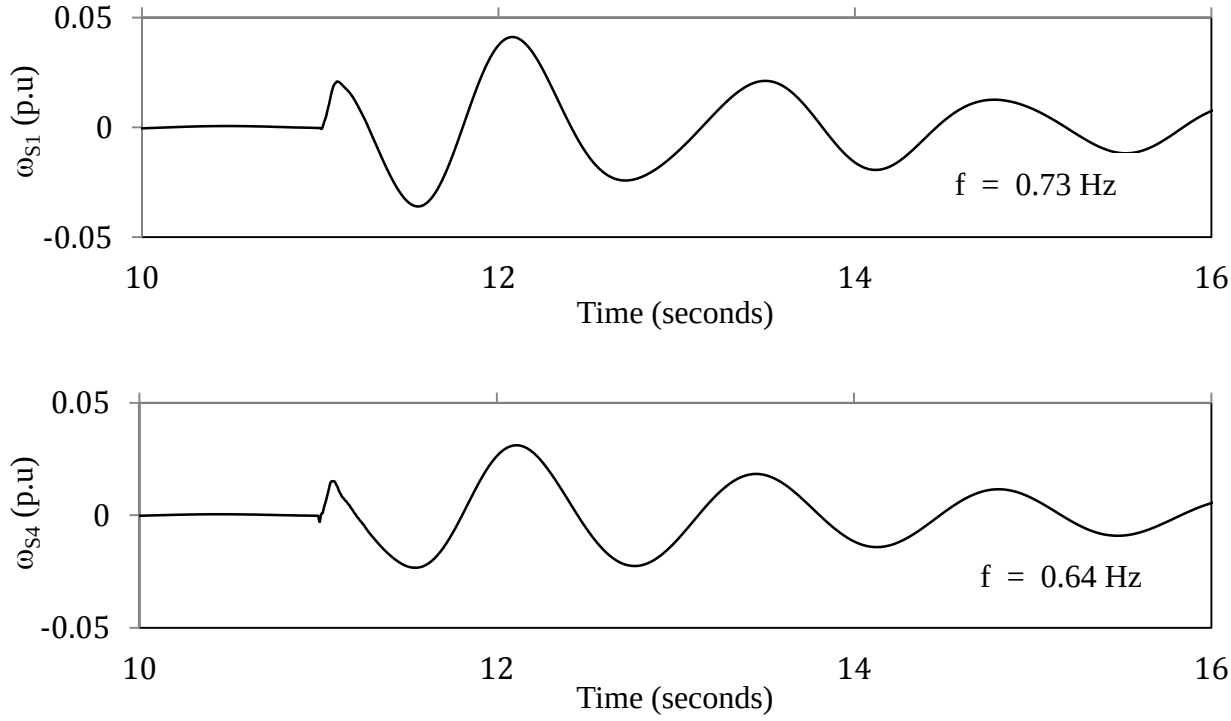

Figure 3.8: Generator rotor speeds during and after clearing a three-cycle, three-phase fault on transmission line N6-S7.

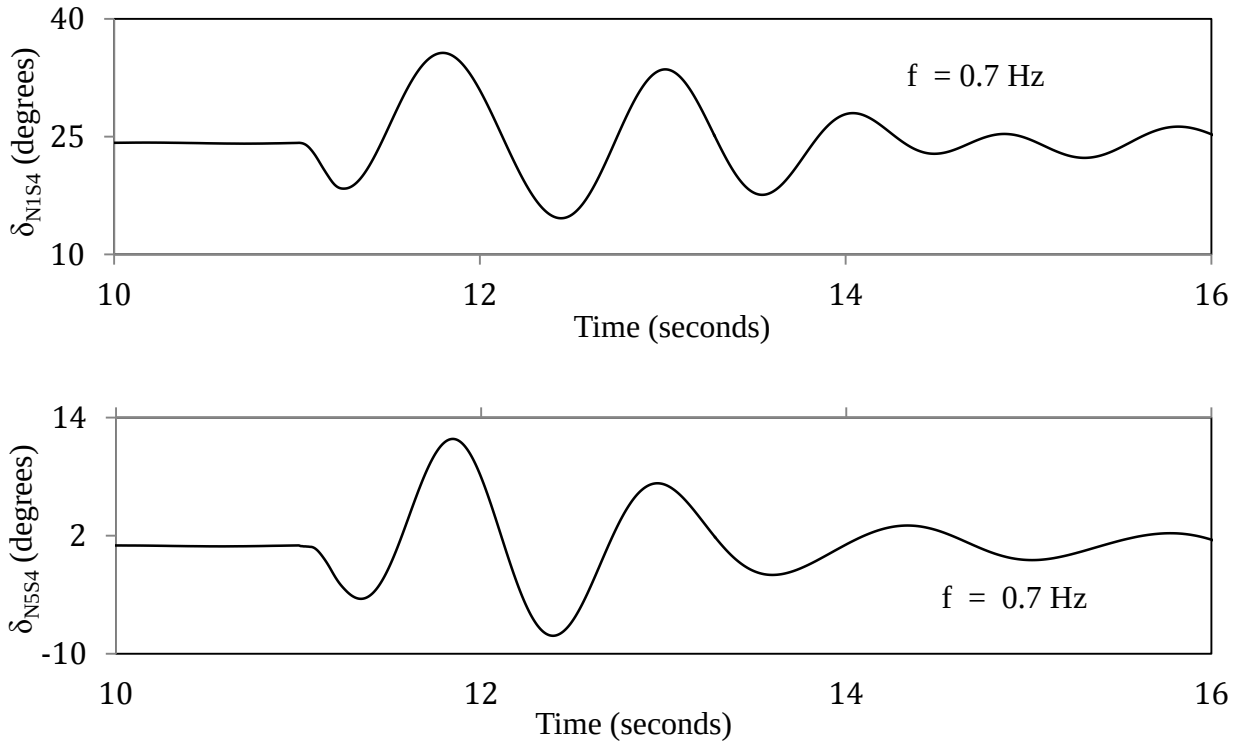

Figure 3.9: Generator load angles, measured with respect to generator G_S4 load angle, during and after clearing a three-cycle, three-phase fault on transmission line N6-S7.

3.4.2 The wash-out filter

The low-frequency oscillations in bus S5 voltage have a frequency about 0.67 Hz. Therefore, the washout block is designed to eliminate the DC component and pass all stabilizing signals in the range of 0.67 Hz.

$$G(s)_{Washout} = \frac{s20}{1 + s20}$$

3.4.3 The phase compensation

There is a phase shift between the stabilizing signal (ω_{S4}) and bus S5 voltage. By varying the parameters of the transfer function of the phase compensation block, an acceptable damping is achieved at a phase compensation of 46.86°.

$$G(s)_{Phase\ compensation} = \frac{1 + 0.8s}{1 + 0.125s}$$

The final design of the VSS HVDC POD supplemental controller is shown in Figure 3.10.

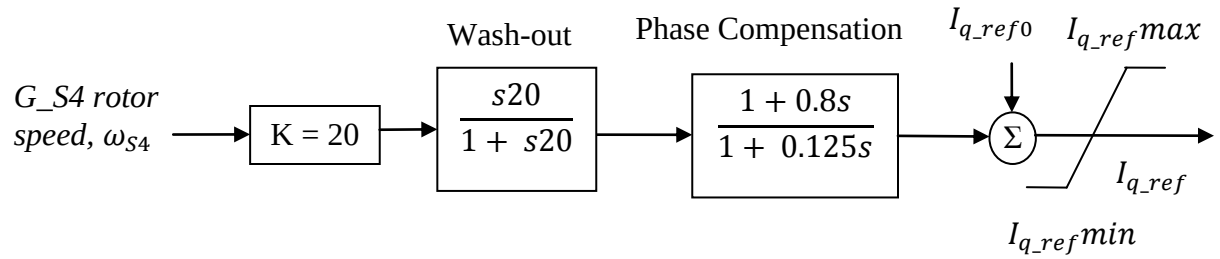

Figure 3.10: The VSC HVDC POD supplemental controller.

3.5 Summary

In this chapter, the load flow studies of SaskPower North and South systems as well as of the integrated system incorporating the HVAC 138 kV double-circuit tie-line and the ± 110 kV VSC HVDC link are presented. The basic control strategy of VSC HVDC transmission system is also discussed. Furthermore, the general structure of the VSC HVDC POD supplemental controller and an insight on the selection of its stabilizing signal are also presented. In this regard, it has been found that the best stabilizing signal is G_S4 speed. The effectiveness of the VSC HVDC supplemental control in damping the low-frequency oscillations in SaskPower integrated system is investigated in the next chapter.

Chapter 4

DYNAMIC PERFORMANCE OF THE VSC HVDC TIE-LINE AND ITS POD SUPPLEMENTAL CONTROLLER

4.1 Introduction

In this chapter, the performances of the VSC HVDC link and its POD supplemental controller are investigated. In this context, several time-domain simulations of three-cycle, three-phase faults at different system locations are carried out on SaskPower integrated system for the following two cases:

Case I: Performance of the VSC HVDC link when its POD supplemental control is not activated.

Case II: Performance of the VSC HVDC link when its POD supplemental control is activated.

4.2 Performance of the VSC HVDC Link

4.2.1 Case Study 1: Three-cycle, three-phase fault on transmission line S5-S4 with line tripping

As it can be seen from Figures 3.4 and 4.1, transmission line S5-S4 is a major line in SaskPower South system that delivers 76.1 MW to load L_{S5}. Selected system bus voltages, generator speeds and transmission line real power flows during and after fault clearing (line tripping) are illustrated in Figures 4.2, 4.3 and 4.4 respectively. The following observations can be made from these figures:

- In the case of the VSC HVDC link, the magnitudes of bus S5, S3 and N3 voltages are almost unchanged after tripping line S5-S4. This is due to the fact that the VSC HVDC link regulates the voltages at its converters at their specified values (i.e. maintains the magnitudes of bus S5 and N4 volatges constant). As buses N3 and S3 are located close to buses N4 and S5

respectively, their voltage magnitudes are almost unchanged after fault clearing. On the other hand, in the case of the AC tie-line, tripping line S5-S4 results in a substantial reduction in the magnitude of bus S5 voltage which consequently results in reductions in the magnitudes of bus S3 and N3 voltages as shown in Figure 4.2.

- As it can be seen from Figure 3.4, load L_{S5} at bus S5 is supplied from transmission line S4-S5 and the VSC HVDC link. Moreover, 34.6 MW is transmitted from bus S5 to load L_{S3} through transmission line S5-S3. As a result of tripping transmission line S5-N4, the real power flow on line S3-S5 is reversed, as shown in Figure 4.4, in order to supply load L_{S5} at bus S5. Furthermore, the power flow on line S2-S3 is increased to compensate for the loss of the real power transmitted on line S4-S5.

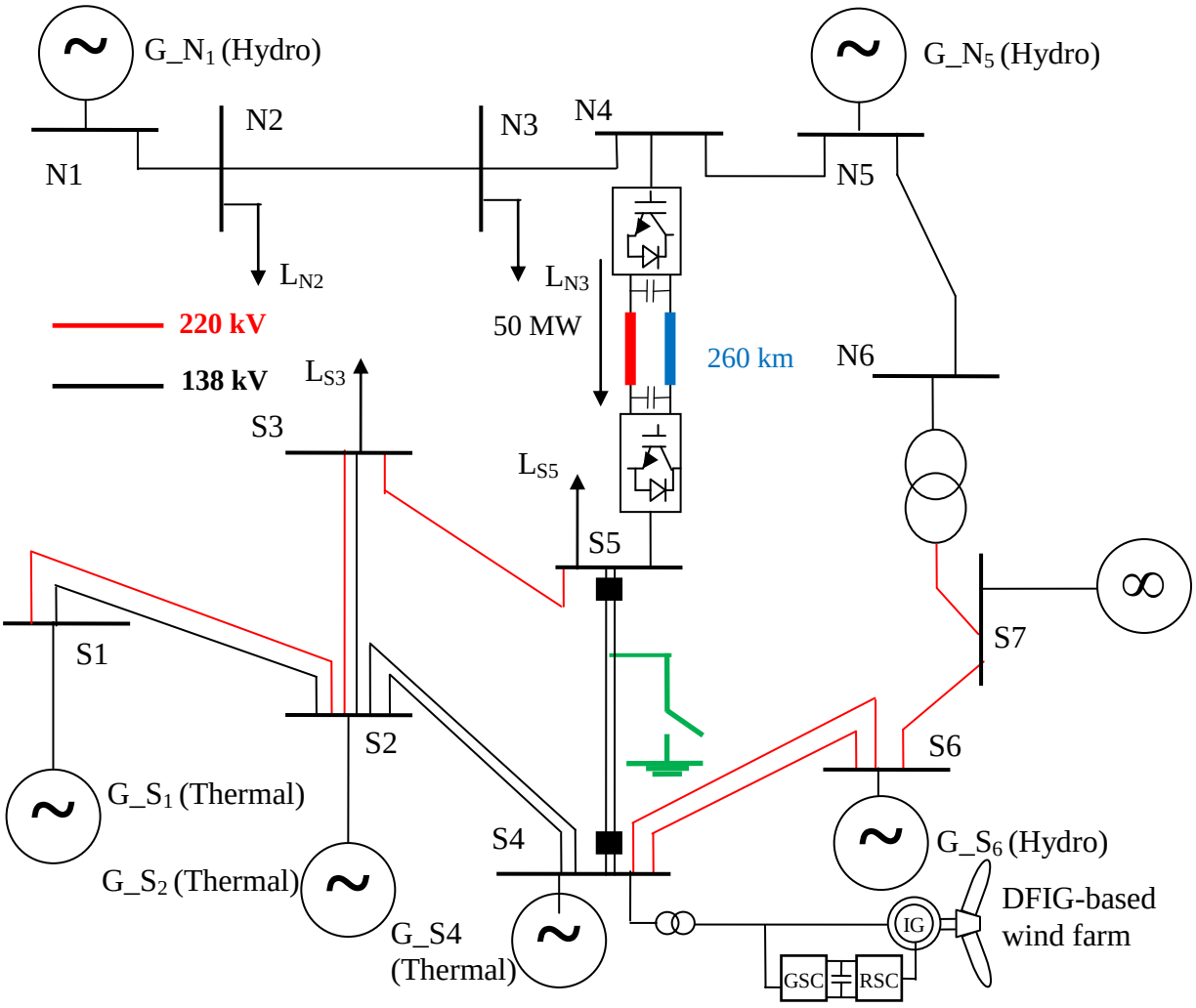

Figure 4.1: Case Study 1: three-cycle, three-phase fault on transmission line S5-S4 with line tripping (POD supplemental controller is not activated).

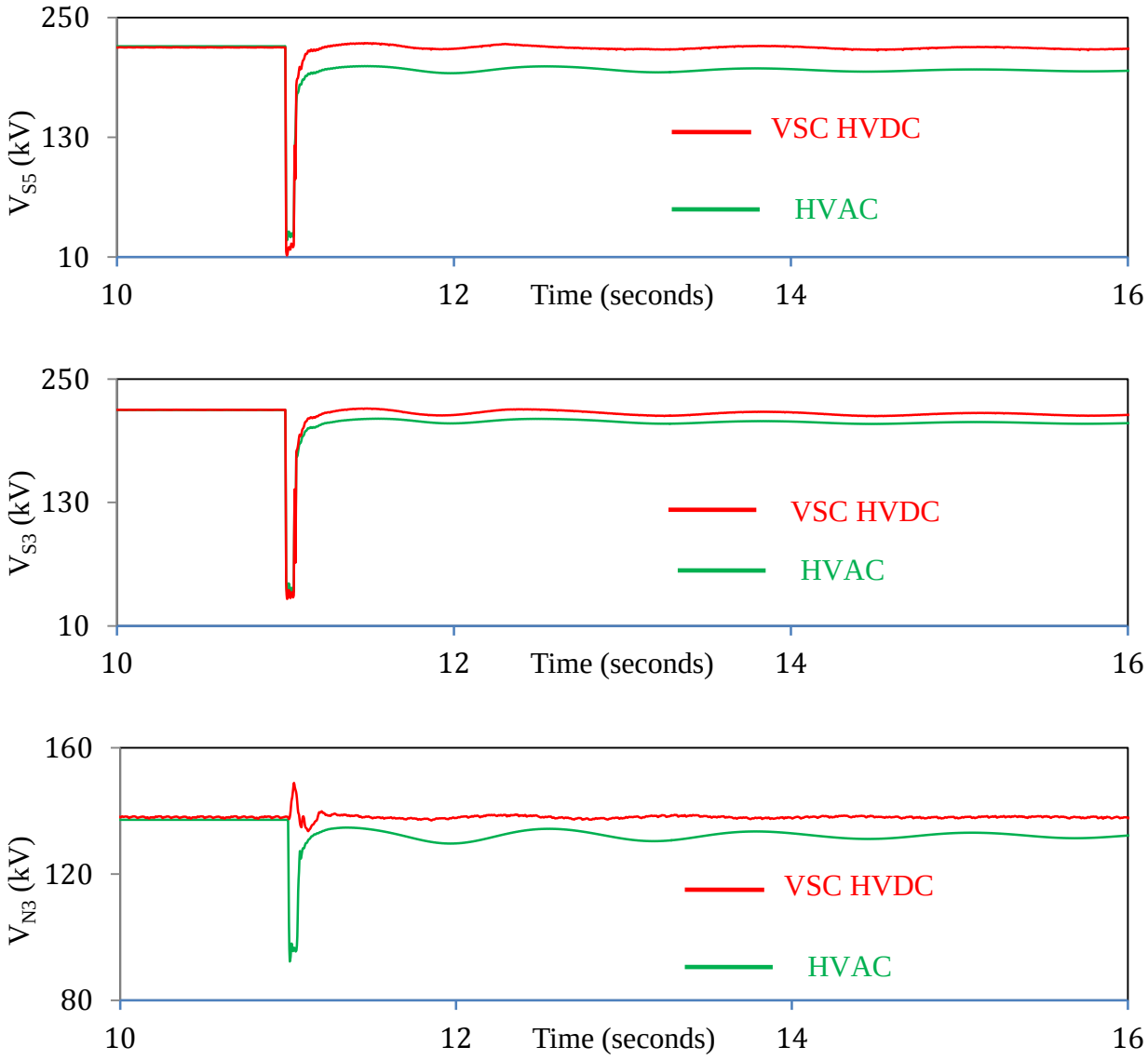

Figure 4.2: System bus voltages during and after clearing a three-cycle, three-phase fault on transmission line S5-S4 (case study 1 - POD supplemental controller is not activated).

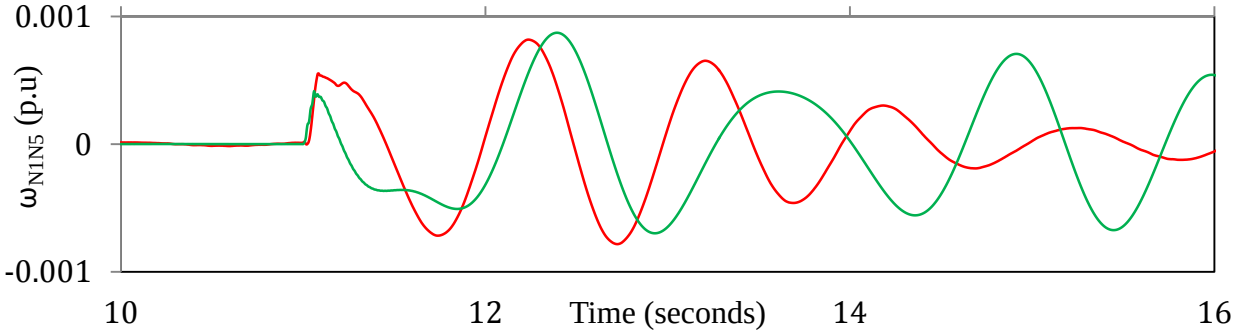

Figure 4.3: Generator speeds, measured with respect to generator G_N5 or G_S4 speed, during and after clearing a three-cycle, three-phase fault on transmission line S5-S4 (case study 1 – POD supplemental controller is not activated).

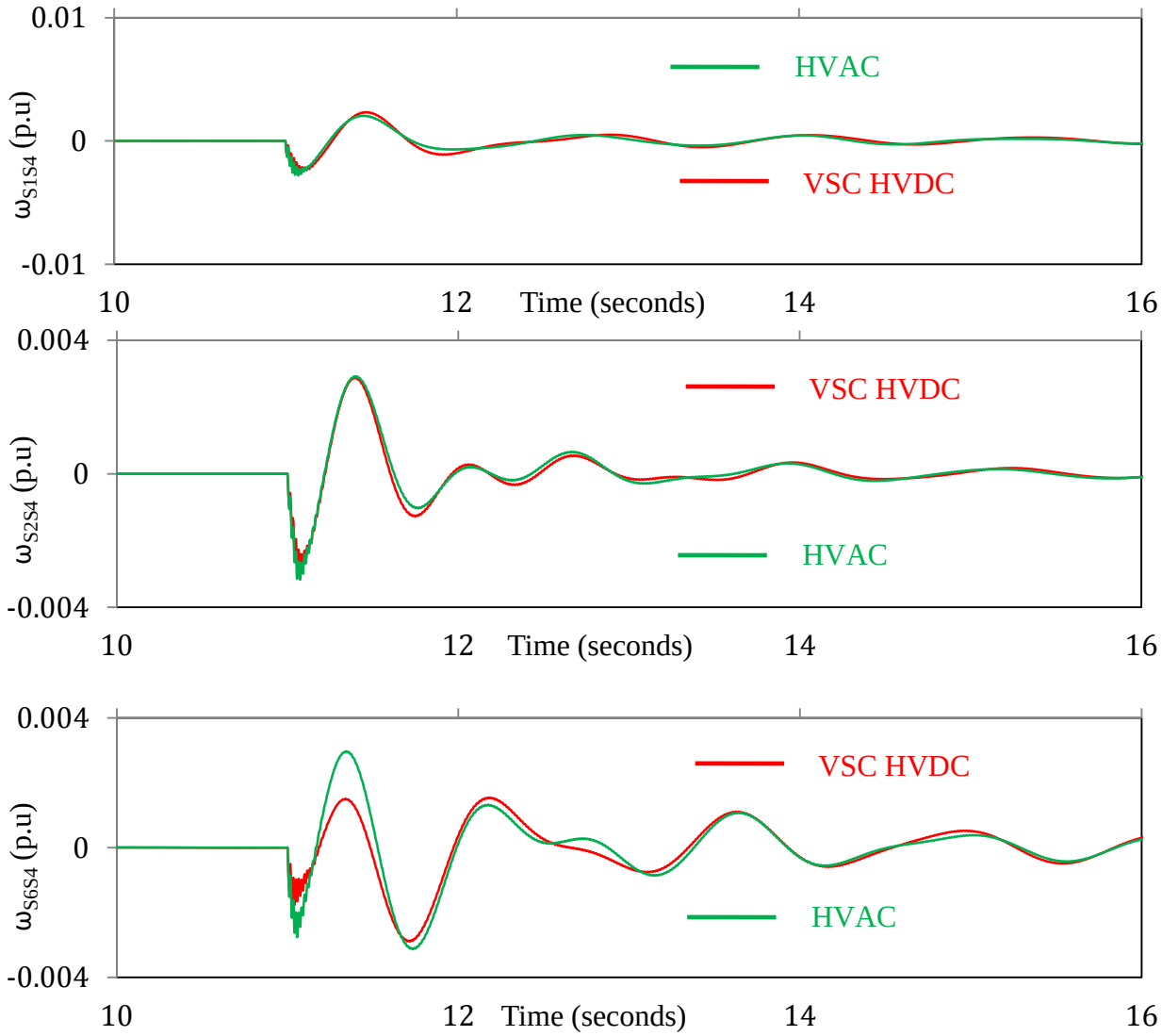

Figure 4.3: continued.

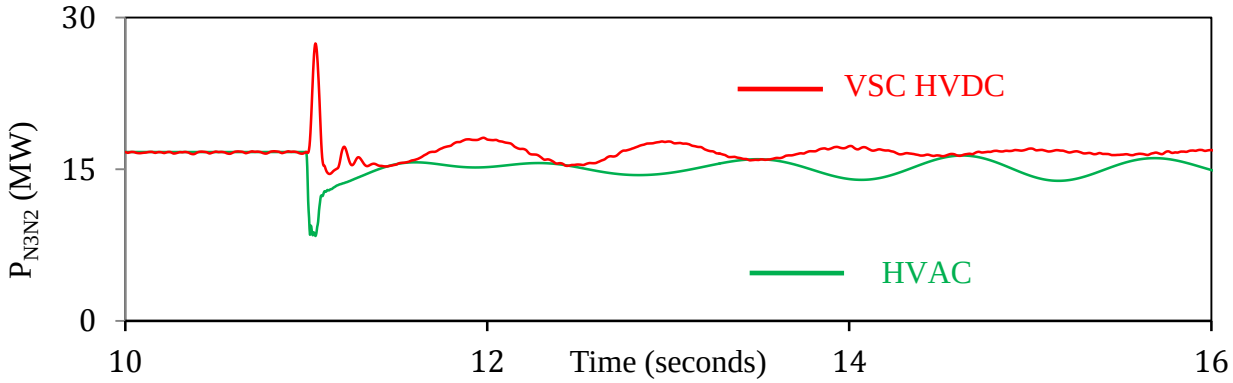

Figure 4.4: Transmission line real power flows during and after clearing a three-cycle, three-phase fault on transmission line S5-S4 (case study 1 – POD supplemental controller is not activated).

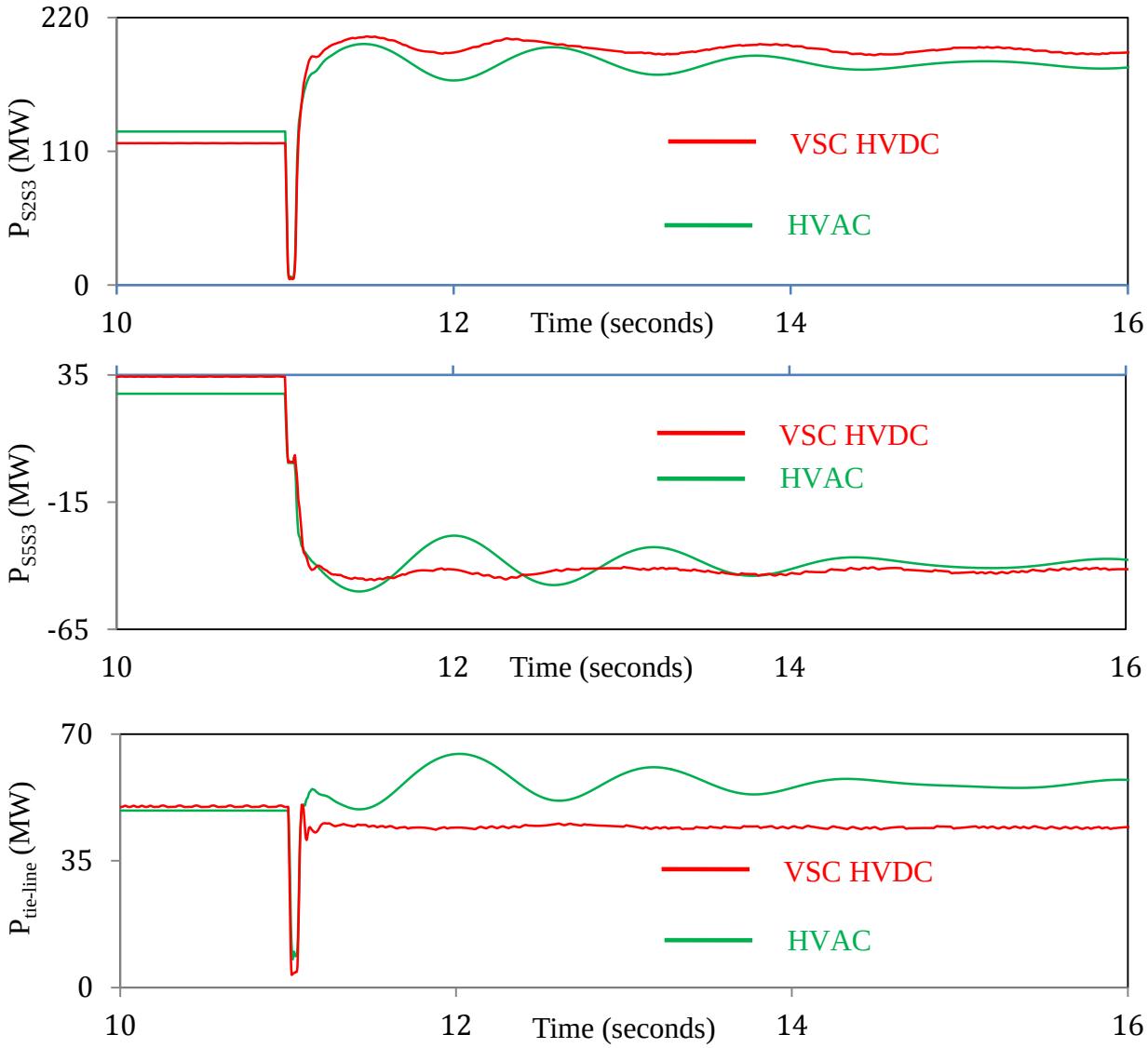

Figure 4.4: continued.

- In the case of the AC tie-line, Figure 4.3 shows that generator G_N1 speed, measured with respect to generator G_N5 speed, exhibits poor damping. To the contrary, in the case of the VSC HVDC link, the oscillations are well damped.
- In the case of the AC tie-line, Figure 4.4 shows that the tie-line power flow increases after tripping line S4-S5. To the contrary, in the case of the VSC HVDC link, the tie-line power flow slightly decreases.

4.2.2 Case Study 2: Three-cycle, three-phase fault at bus S7; SaskPower system loses its connection with Manitoba grid

As shown in Figure 4.5, transmission lines N6-S7 and S6-S7 represent respectively SaskPower North and South system connections to Manitoba grid which is represented in the studies conducted in this thesis by an infinite-bus system. A fault on bus S7 followed by tripping lines N6-S7 and S6-S7 results in that SaskPower system loses its connection with Manitoba grid. Selected system bus voltages, generator speeds and transmission line real power flows during and after fault clearing (line tripping) are illustrated in Figures 4.6, 4.7 and 4.8 respectively. The following observation can be made from these figures:

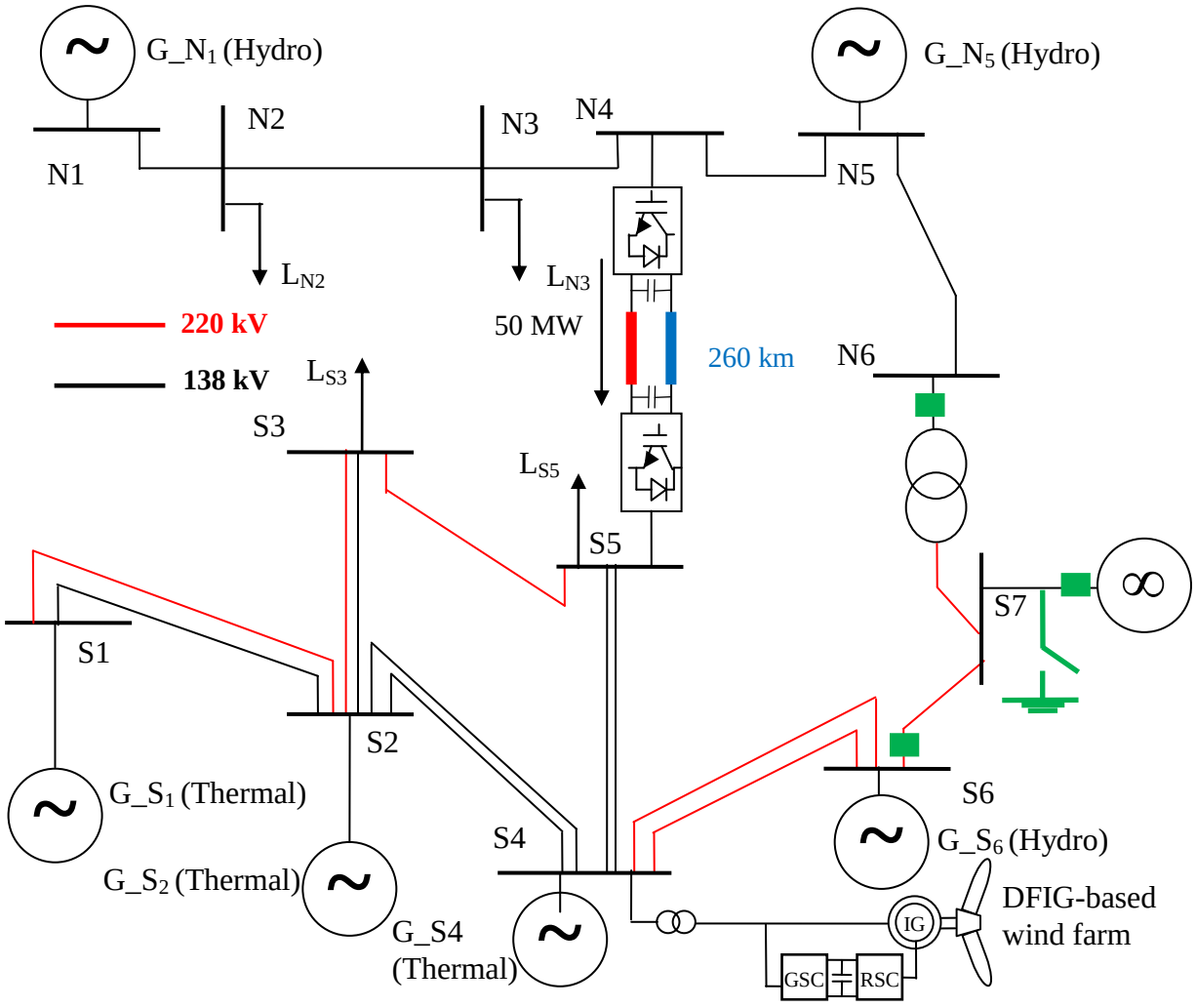

Figure 4.5: Case Study 2: three-cycle, three-phase fault at bus S7; SaskPower system loses its connection with Manitoba grid (POD supplemental controller is not activated).

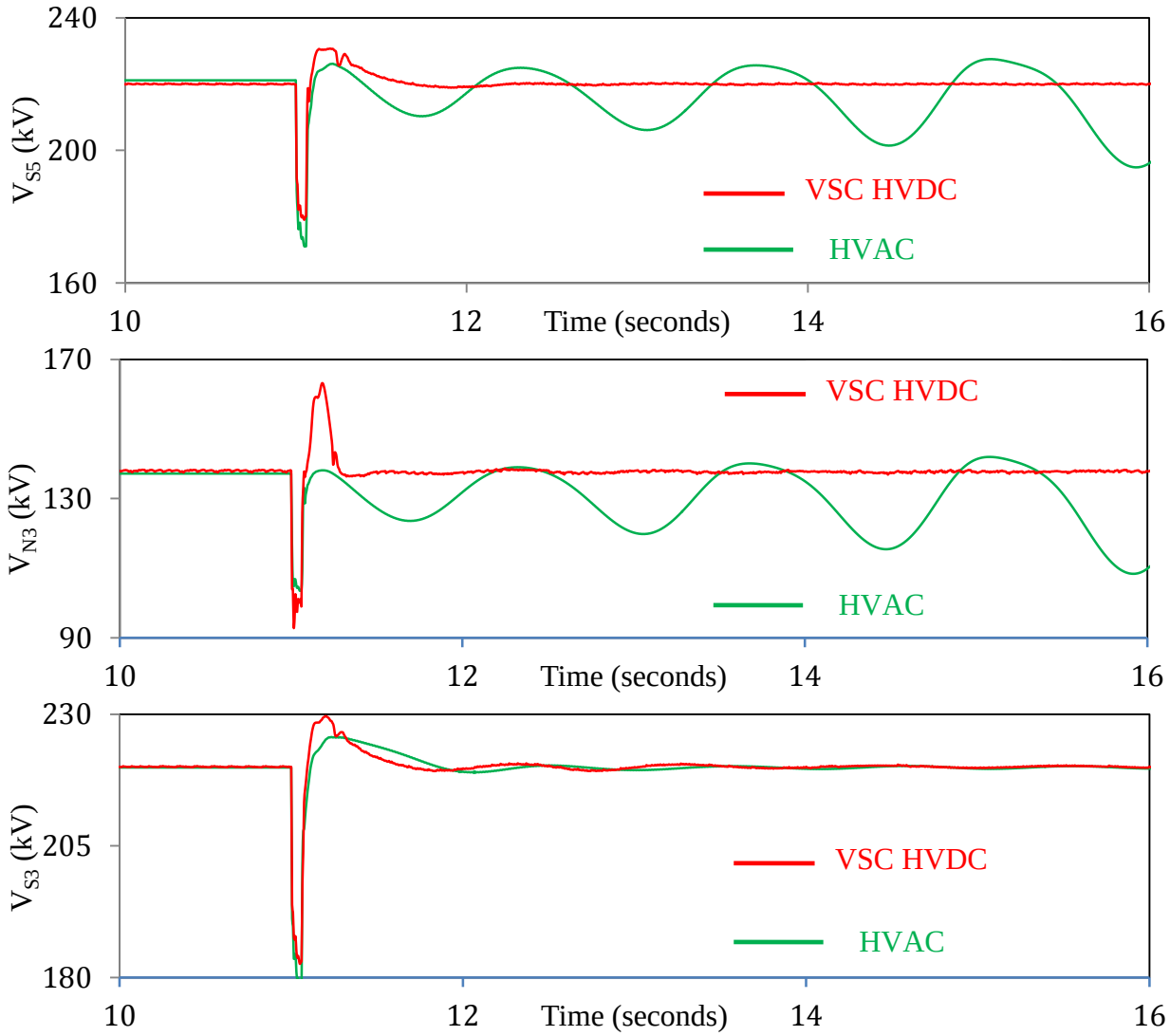

Figure 4.6: System bus voltages during and after clearing a three-cycle, three-phase fault on Manitoba connection bus (case study 2 – POD supplemental controller is not activated).

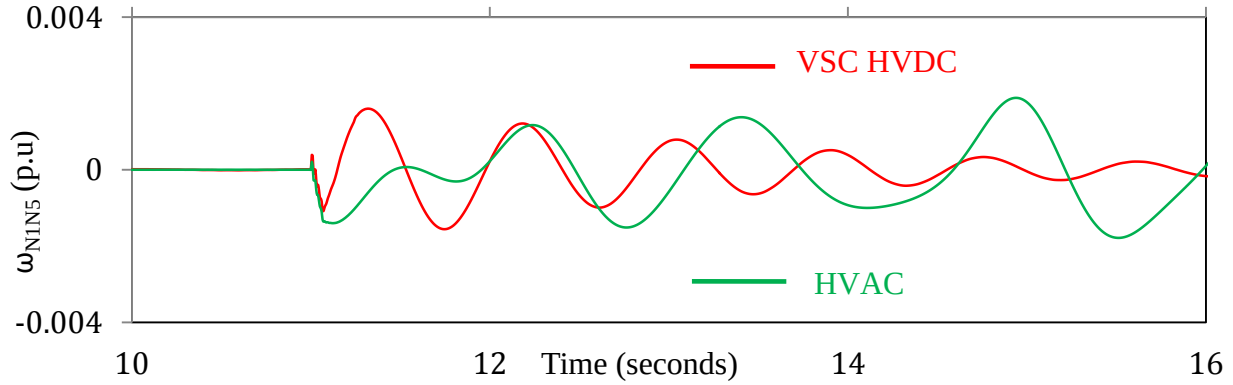

Figure 4.7: Generator speeds, measured with respect to generator G_N5 or G_S4 speed, during and after clearing a three-cycle, three-phase fault on Manitoba connection bus (case study 2 – POD supplemental controller is not activated).

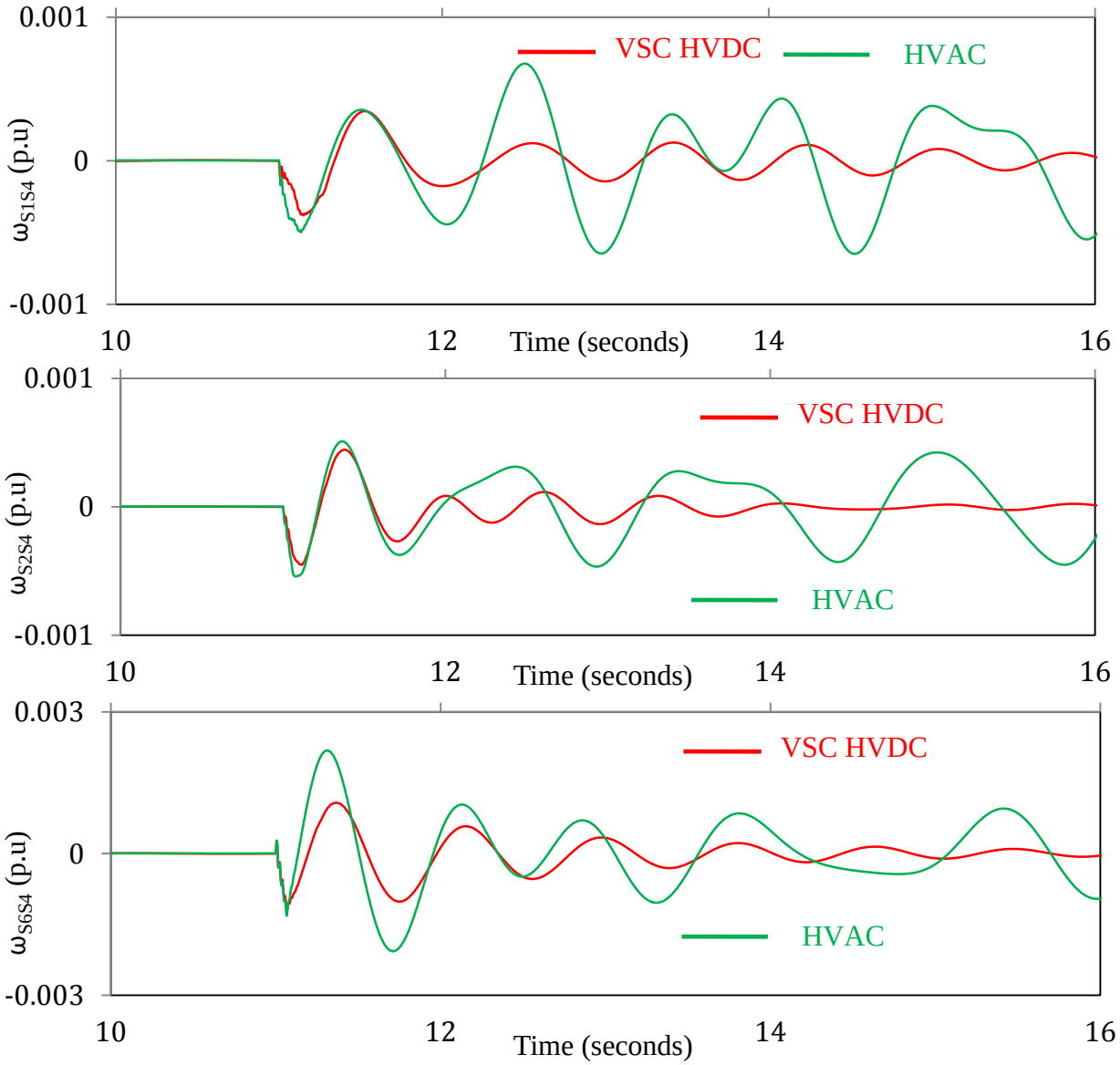

Figure 4.7: continued.

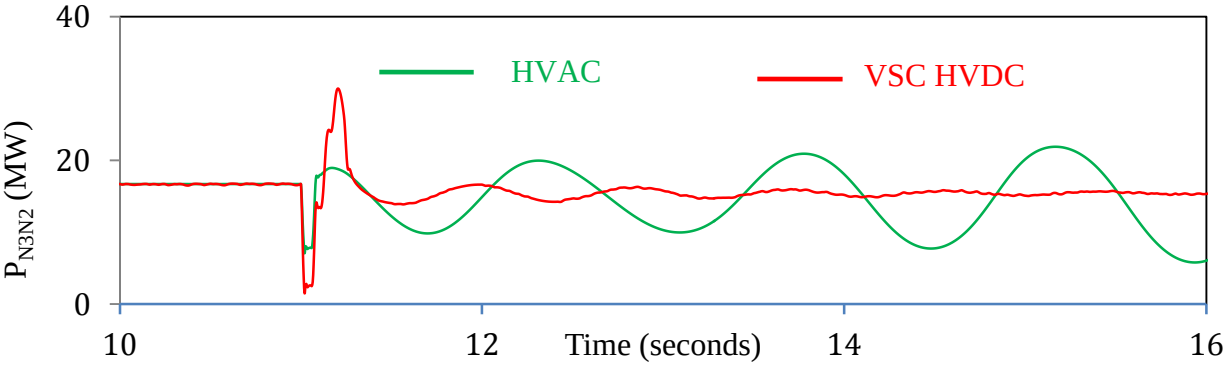

Figure 4.8: Transmission line real power flows during and after clearing a three-cycle, three-phase fault on Manitoba connection bus (case study 2 – POD supplemental controller is not activated).

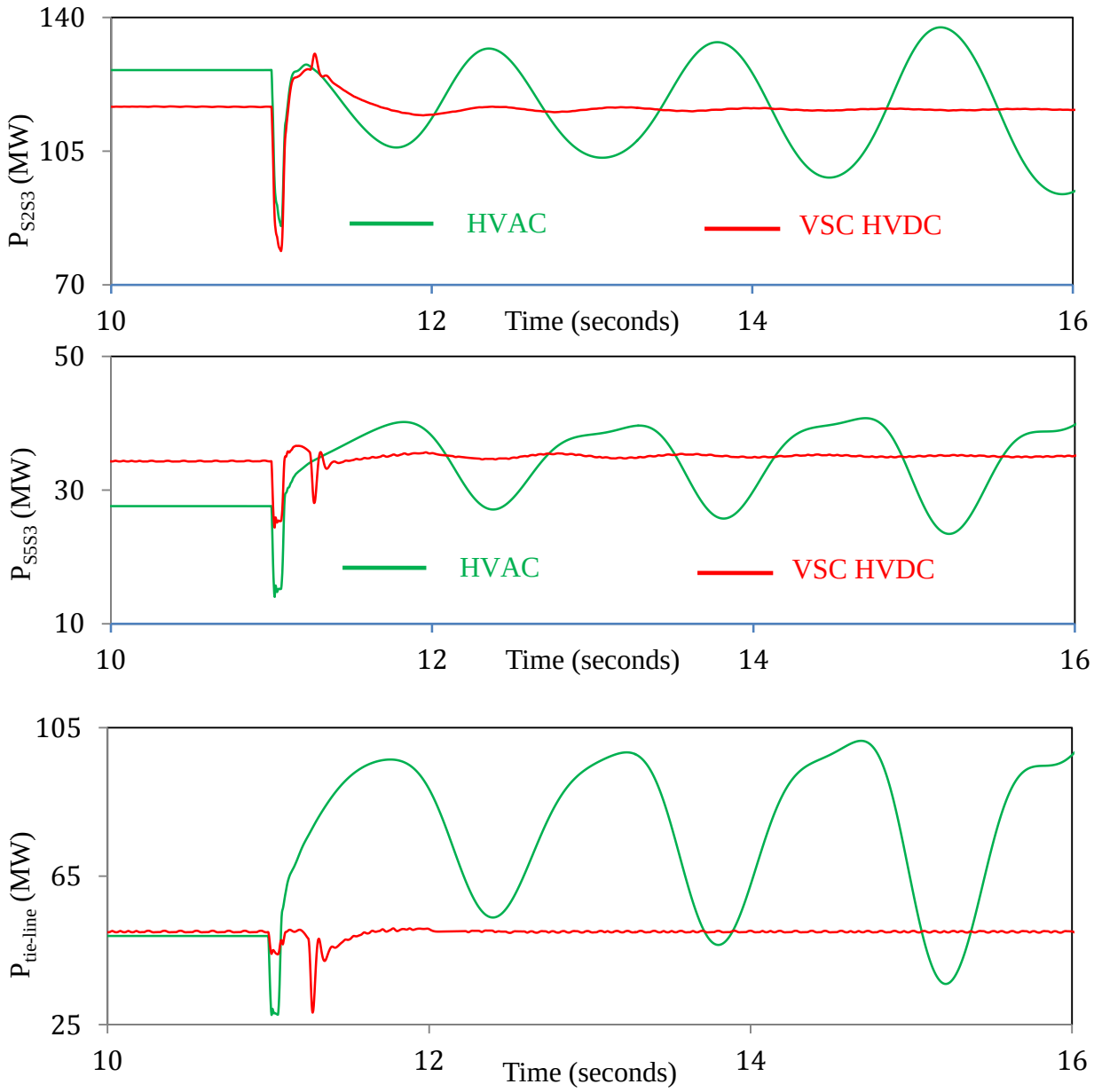

Figure 4.8: continued.

- Losing the connection with Manitoba grid is a severe event. In the case of the AC tie-line, SaskPower integrated system loses its stability. Severe growing oscillations can be observed in the system bus voltages, generator speeds and transmission line real power flows. To the contrary, in the case of the VSC HVDC link, SaskPower system stability is maintained after such a severe disturbance.

4.2.3 Case Study 3: Three-cycle, three-phase fault on transmission line N6-S7; SaskPower North system loses its connection with Manitoba grid

The fault location is shown in Figure 4.9. Tripping transmission line N6-S7 results in that SaskPower North system loses its connection with Manitoba grid. Selected system bus voltages, generator speeds and transmission line real power flows during and after fault clearing (line tripping) are illustrated in Figures 4.10, 4.11 and 4.12 respectively. The following observation can be made from these figures:

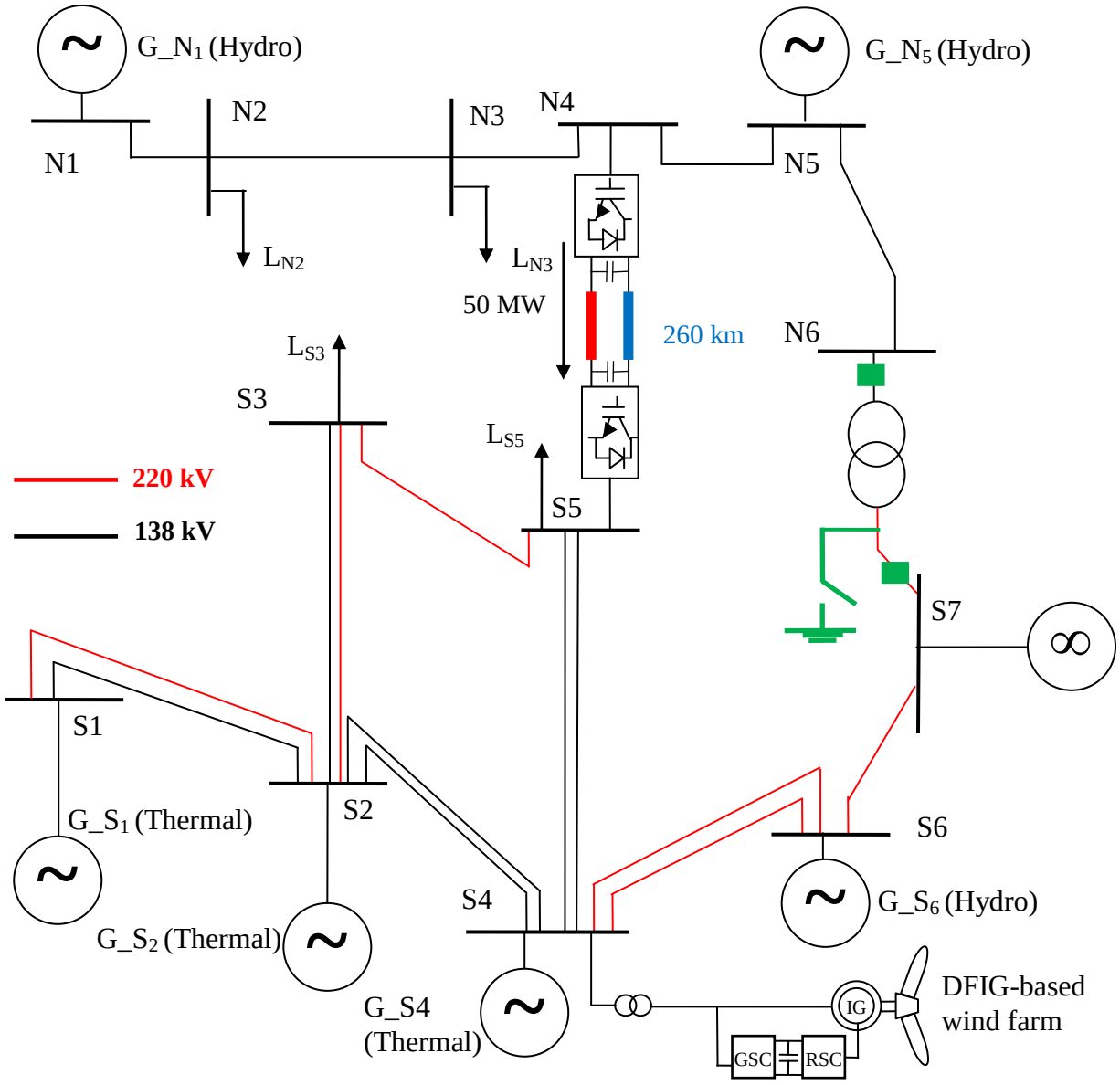

Figure 4.9: Case Study 3: three-cycle, three-phase fault on transmission line N6-S7; SaskPower North system loses its connection with Manitoba grid (POD supplemental controller is not activated).

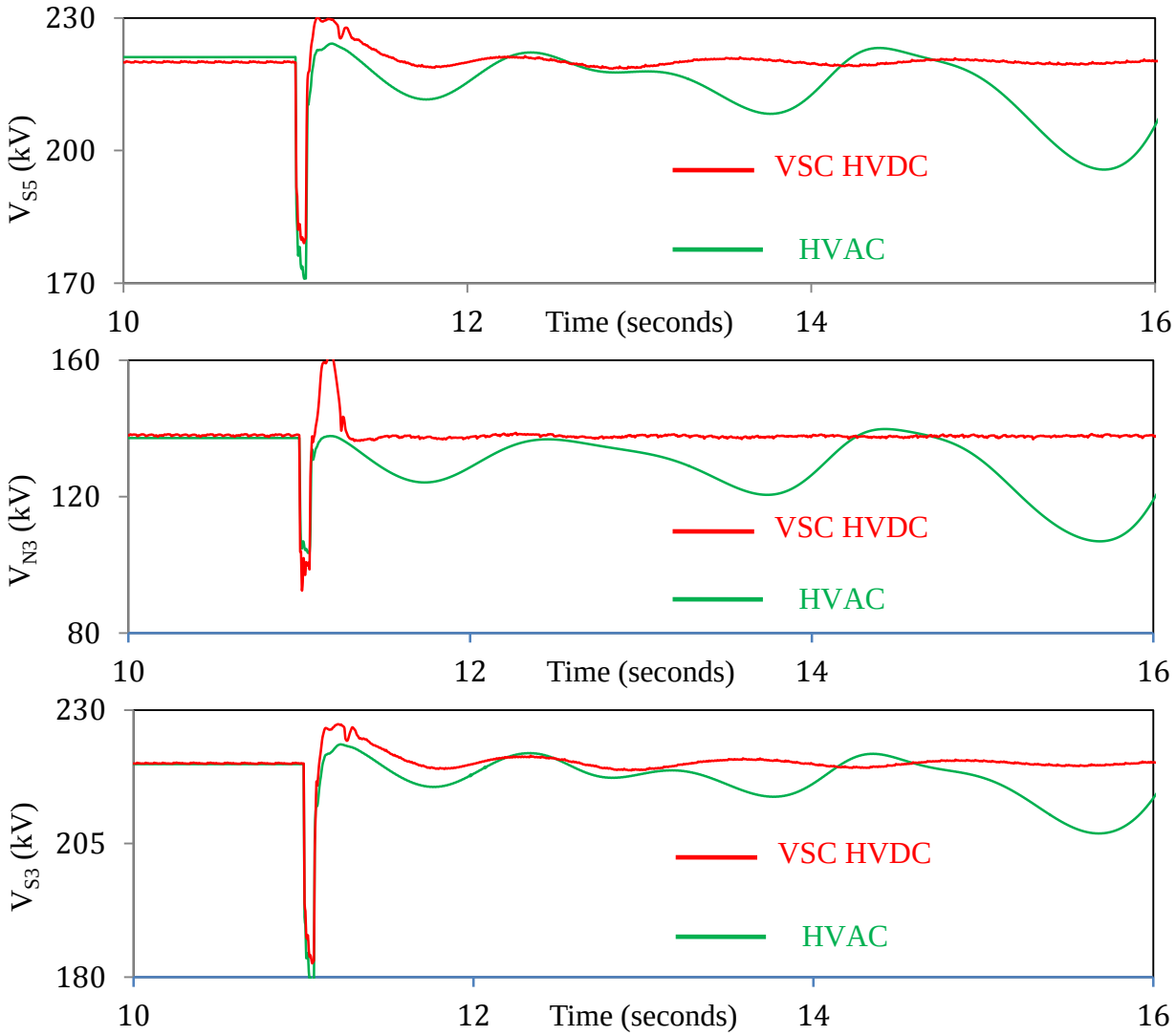

Figure 4.10: System bus voltages during and after clearing a three-cycle, three-phase fault on transmission line N6-S7 (case study 3 – POD supplemental controller is not activated).

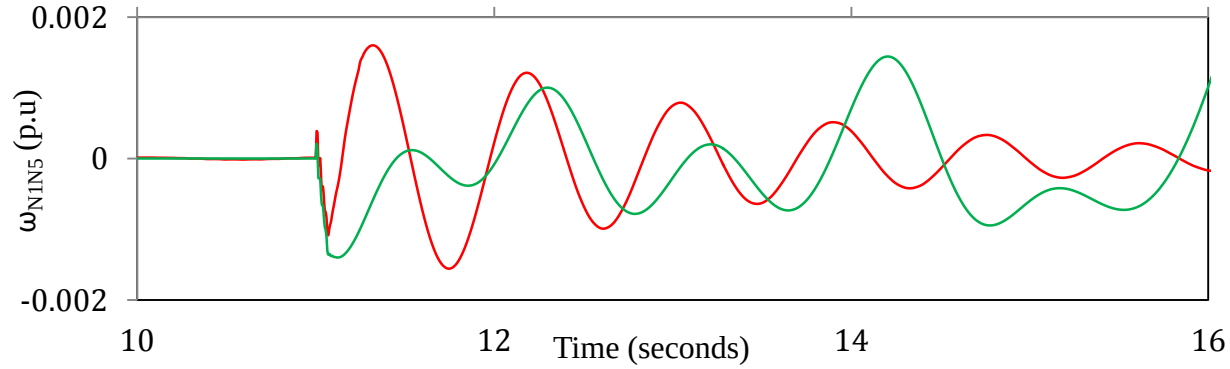

Figure 4.11: Generator speeds, measured with respect to generator G_N5 or G_S4 speed, during and after clearing a three-cycle, three-phase fault on transmission line N6-S7 (case study 3 – POD supplemental controller is not activated).

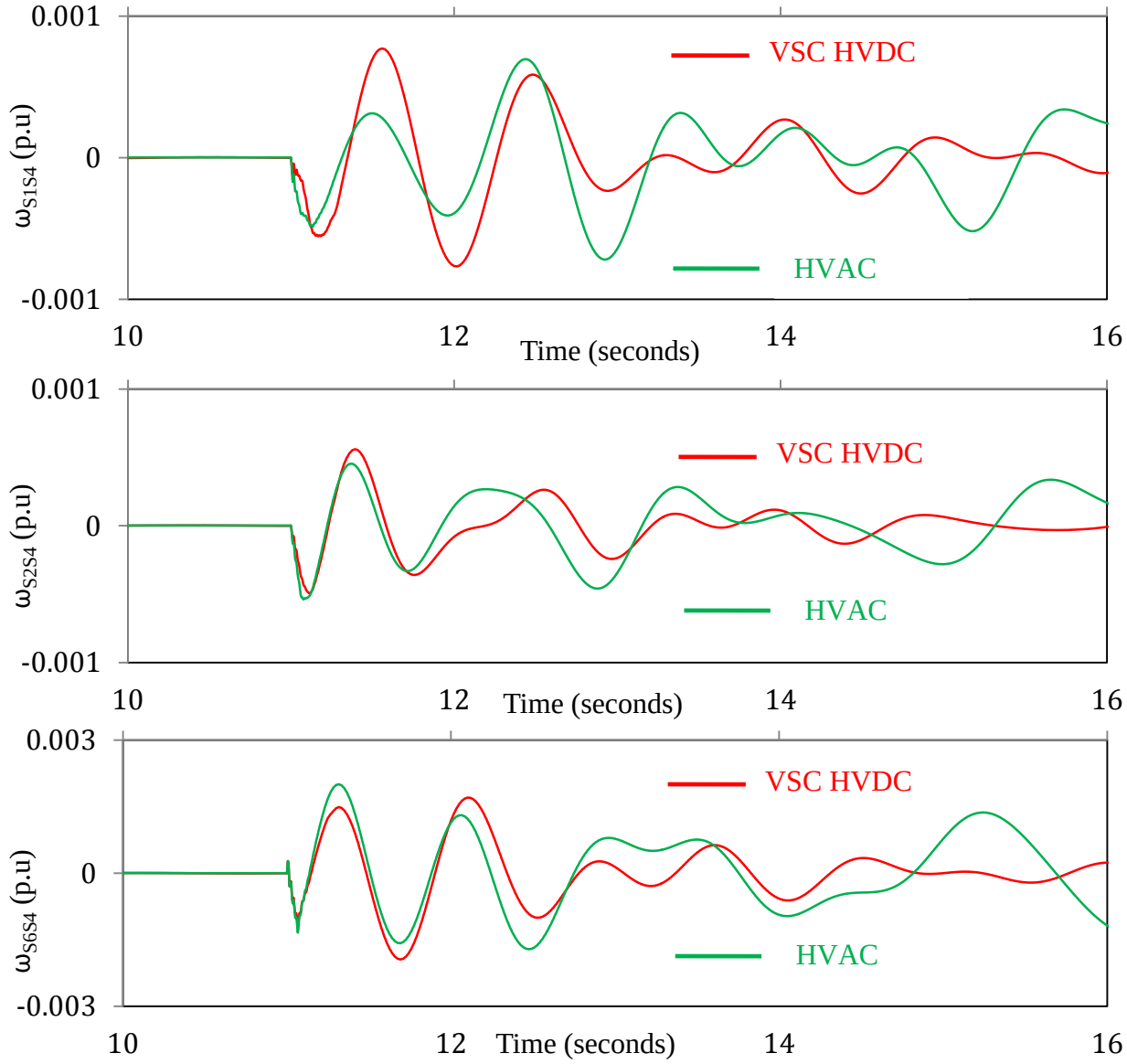

Figure 4.11: continued.

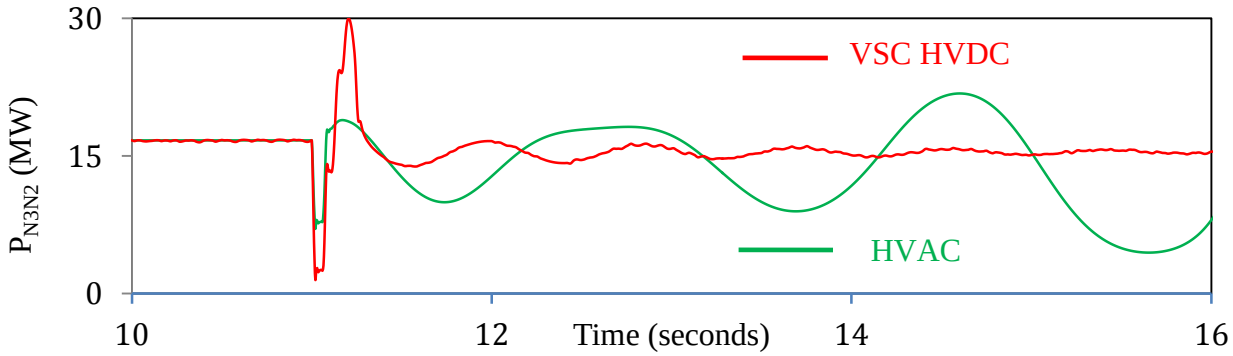

Figure 4.12: Transmission line real power flows during and after clearing a three-cycle, three-phase fault on transmission line N6-S7 (case study 3 – POD supplemental controller is not activated).

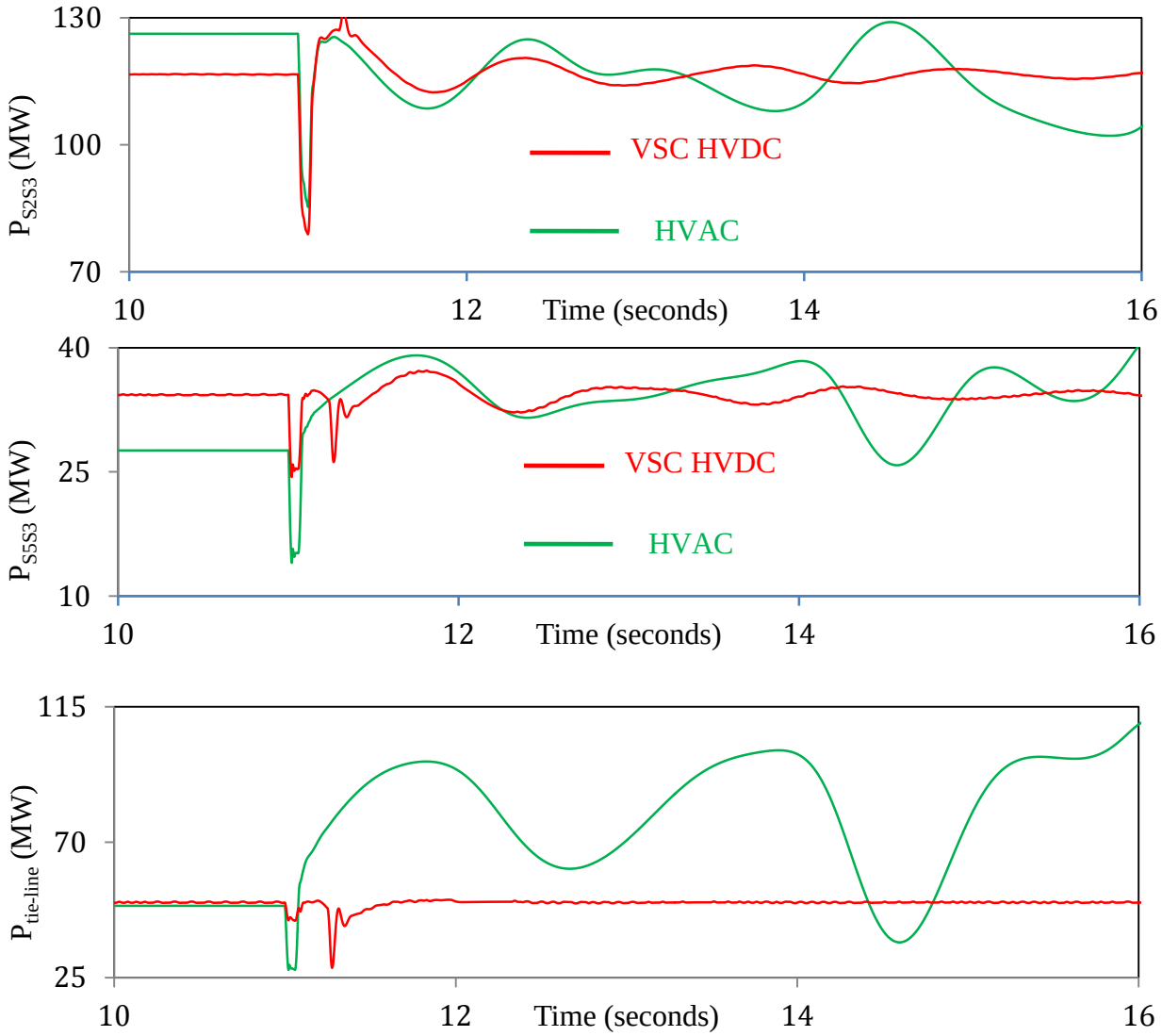

Figure 4.12: continued.

- As it can be seen from these figures, in the case of the AC tie-line, severe oscillations in the system bus voltages, generator speeds and transmission line real power flows are observed. More specific, it can be seen from Figure 4.11 that SaskPower North system loses its stability (observe the growing oscillations in generator G_N1 speed, measured respect to generator G_N5 speed). This is also evident from the tie-line real power flow response, shown in Figure 4.12 that also exhibits severe growing oscillations. On the other hand, Figures 4.10 to 4.12 show that SaskPower system stability is maintained after fault clearing in the case of the VSC HVDC link.

4.2.4 Case Study 4: Three-cycle, three-phase fault on transmission line S6-S7; SaskPower South system loses its connection with Manitoba grid

The fault location is shown in Figure 4.13. Tripping transmission line S6-S7 results in that SaskPower South system loses its connection with Manitoba grid. Selected system bus voltages, generator speeds and transmission line real power flows during and after fault clearing (line tripping) are illustrated in Figures 4.14, 4.15 and 4.16 respectively. The following observations can be made from these figures:

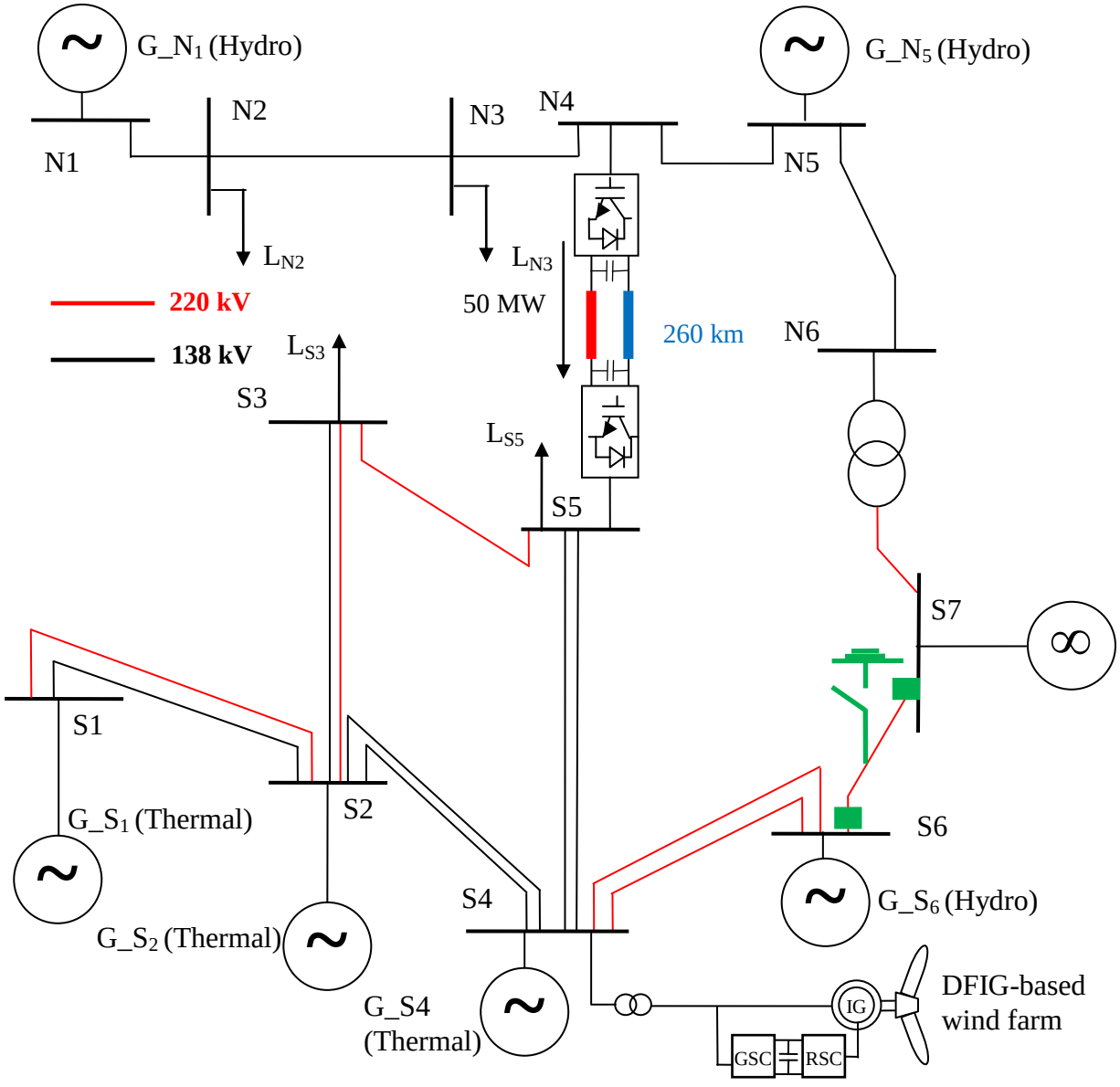

Figure 4.13: Case Study 4: three-cycle, three-phase fault on transmission line S6-S7; SaskPower South system loses its connection with Manitoba grid (POD supplemental controller is not activated).

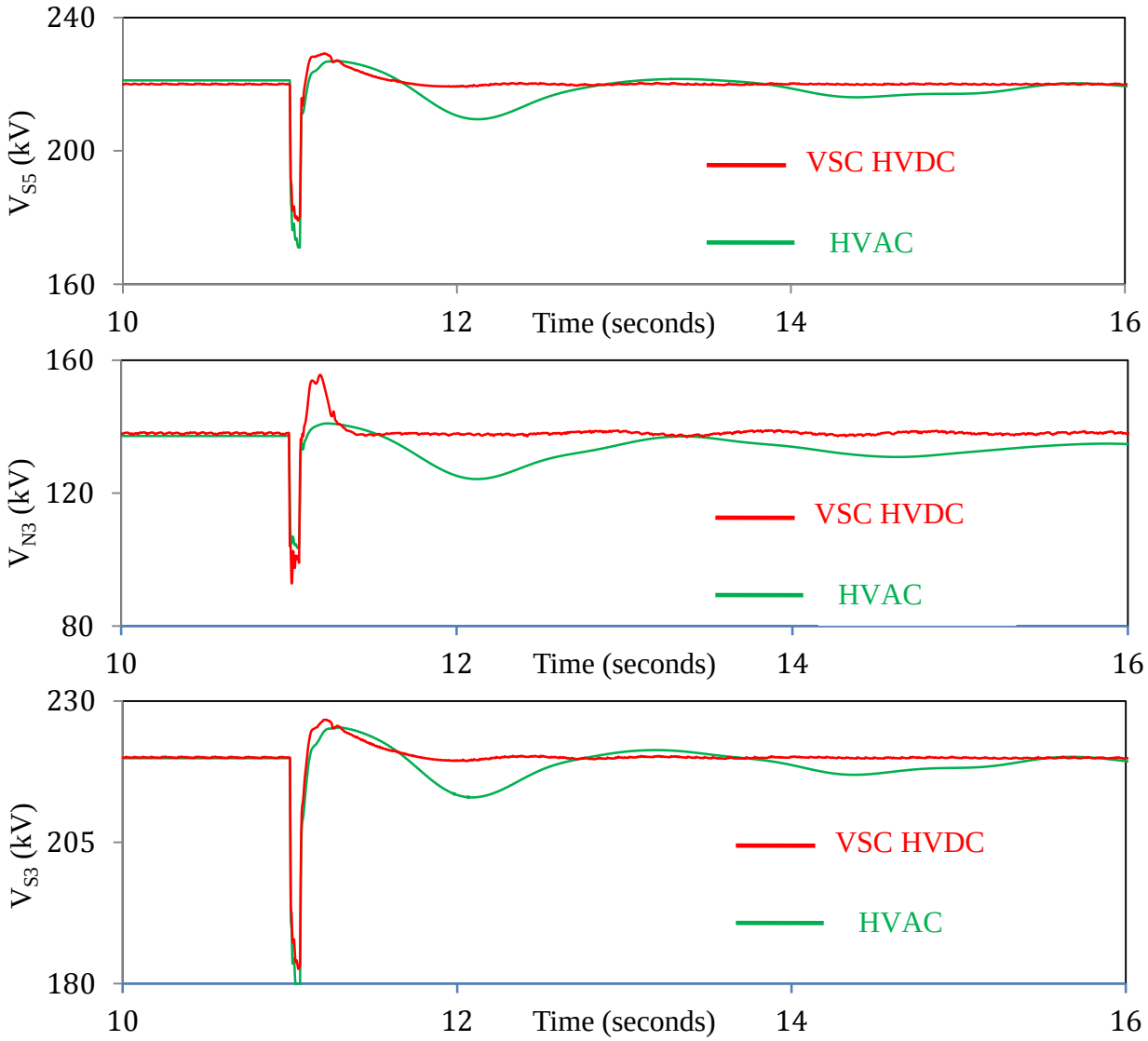

Figure 4.14: System bus voltages during and after clearing a three-cycle, three-phase fault on transmission line S6-S7 (case study 4 - POD supplemental controller is not activated).

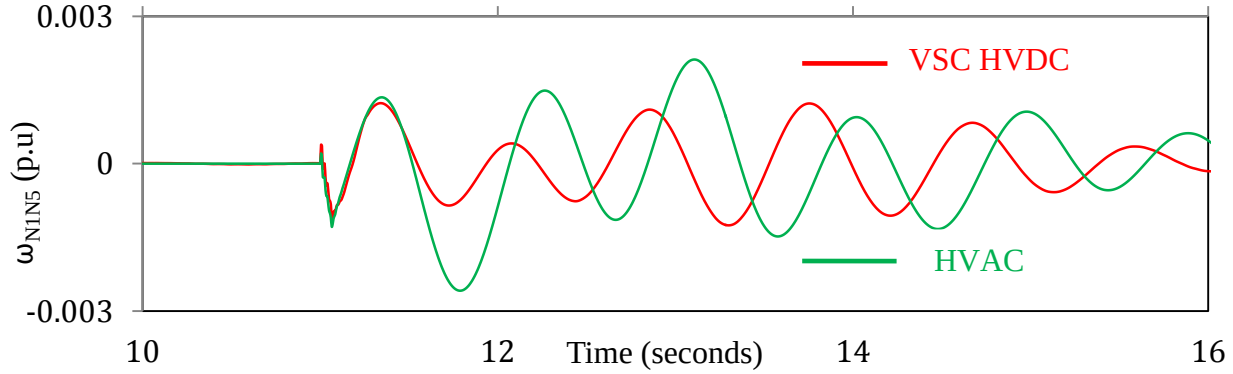

Figure 4.15: Generator speeds, measured with respect to generator G_N5 or G_S4 speed, during and after clearing a three-cycle, three-phase fault on transmission line S6-S7 (case study 4 - POD supplemental controller is not activated).

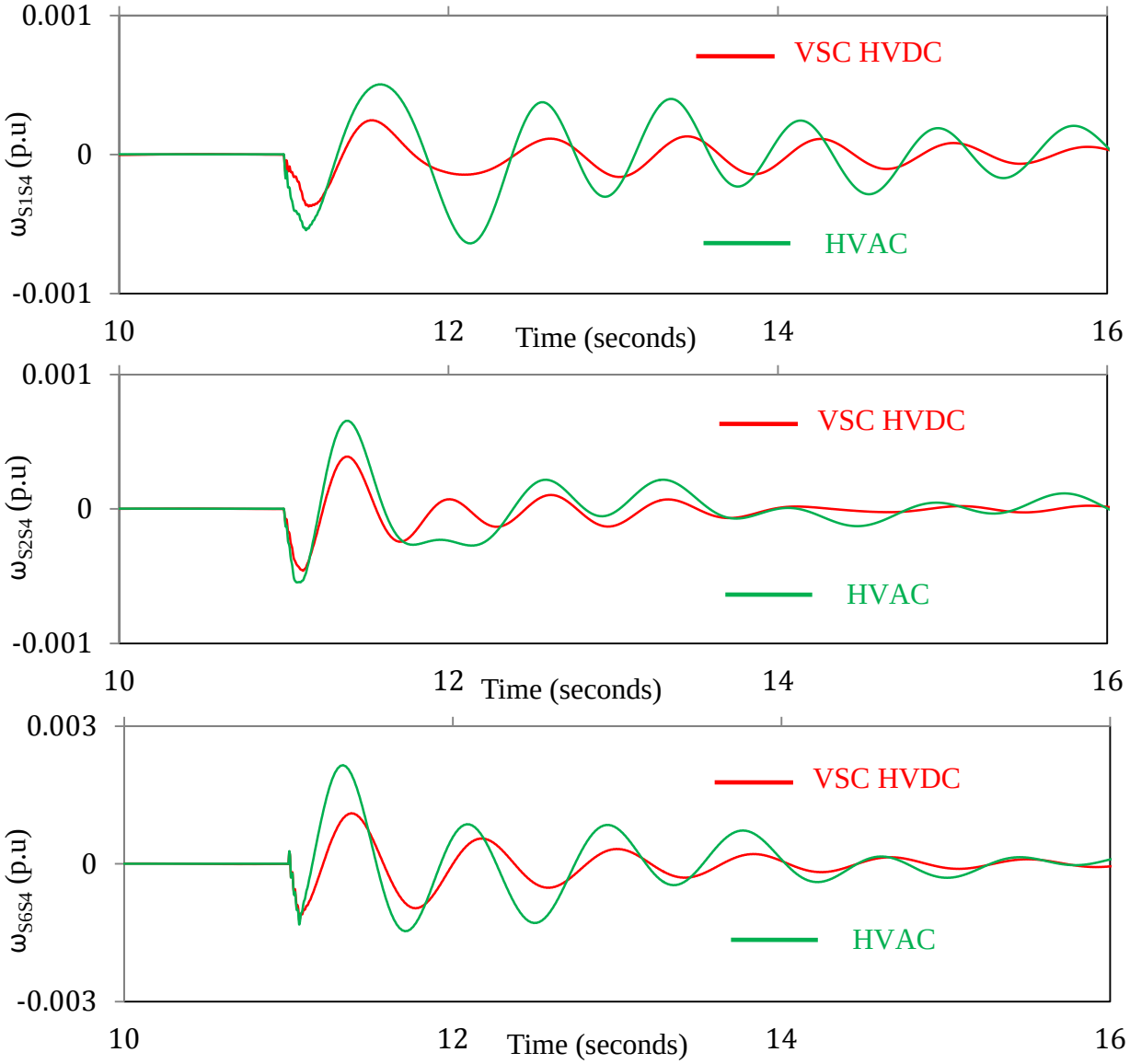

Figure 4.15: continued.

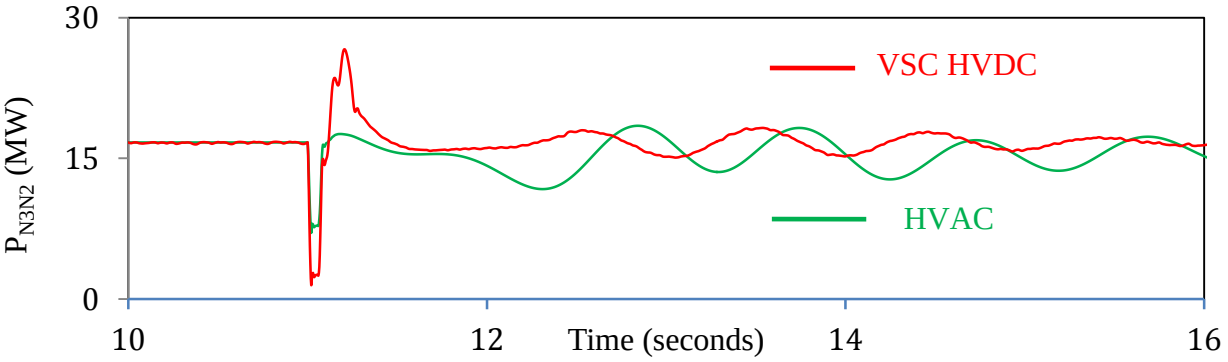

Figure 4.16: Transmission line real power flows during and after clearing a three-cycle, three-phase fault on transmission line S6-S7 (case study 4 - POD supplemental controller is not activated).

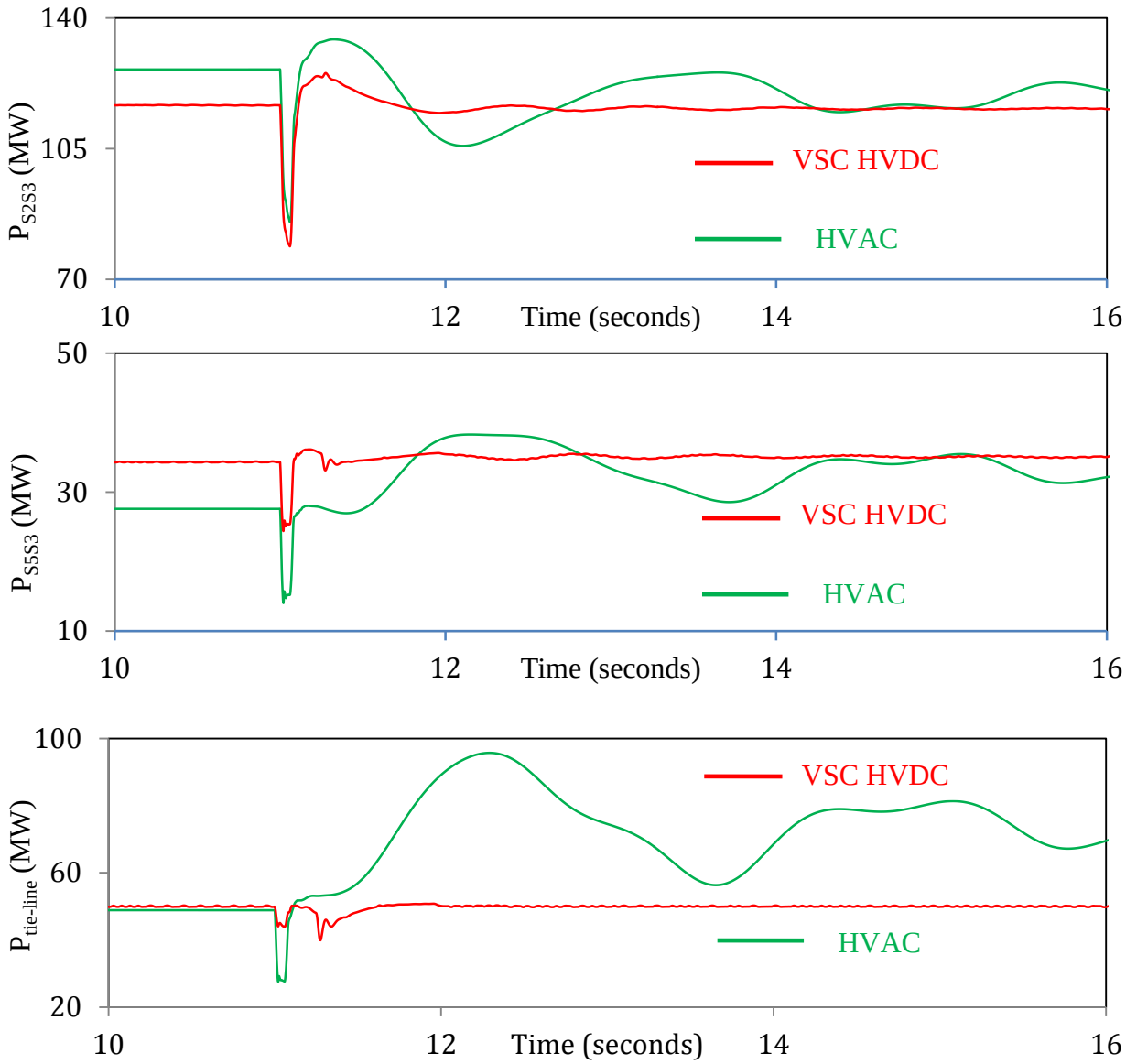

Figure 4.16: continued.

- The disturbance has no severe impact on the system stability regardless of the type of the tie-line.
- The oscillations in the system bus voltages, the generator speeds and the transmission line real power flows are more damped in the case of the VSC HVDC link than in the case of the HVAC tie-line.
- It can be seen from Figure 4.16 that the real power flow through the HVAC tie-line exhibits a poor damping. To the contrary, in the case of the VSC HVDC link, the tie-line real power flow oscillations are well damped.

4.2.5 Case Study 5: Three-cycle, three-phase fault on transmission line S2-S4 with line tripping

The fault location is shown in Figure 4.17. Selected system bus voltages, generator speeds and transmission line real power flows during and after fault clearing (line tripping) are illustrated in Figures 4.18, 4.19 and 4.20 respectively. The following observations can be made from these figures:

- Surprisingly, the oscillations in generator G_N1 speed, measured with respect to generator G_N5 speed, are more damped in the case of the HVAC tie-line than in the case of VSC HVDC link. It should be noticed, however, that $\pm$ 0.004 p.u. speed is a very small range (±1.507 rad/s).

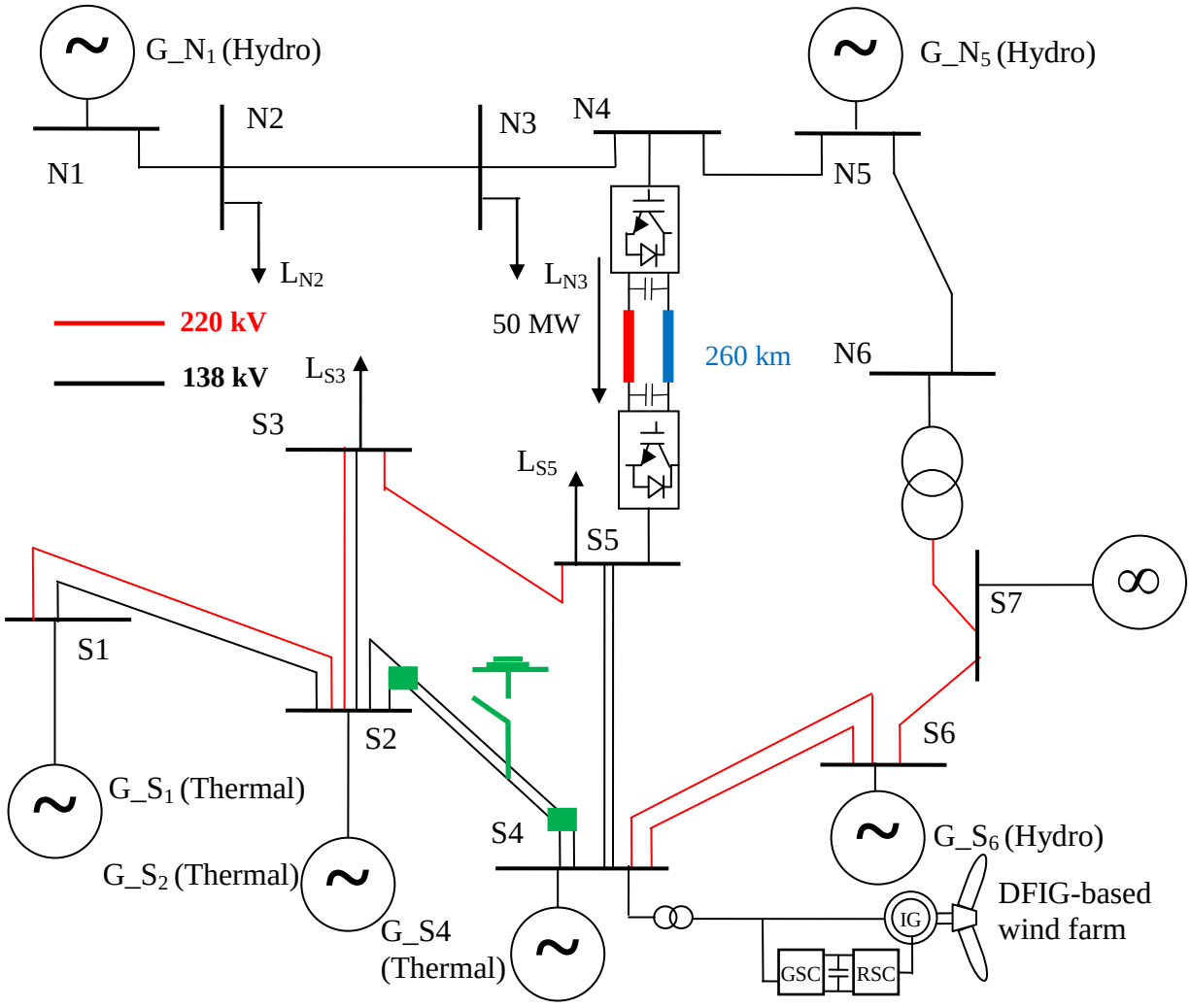

Figure 4.17: Case Study 5: three-cycle, three-phase fault on transmission line S2-S4 with line tripping (POD supplemental controller is not activated).

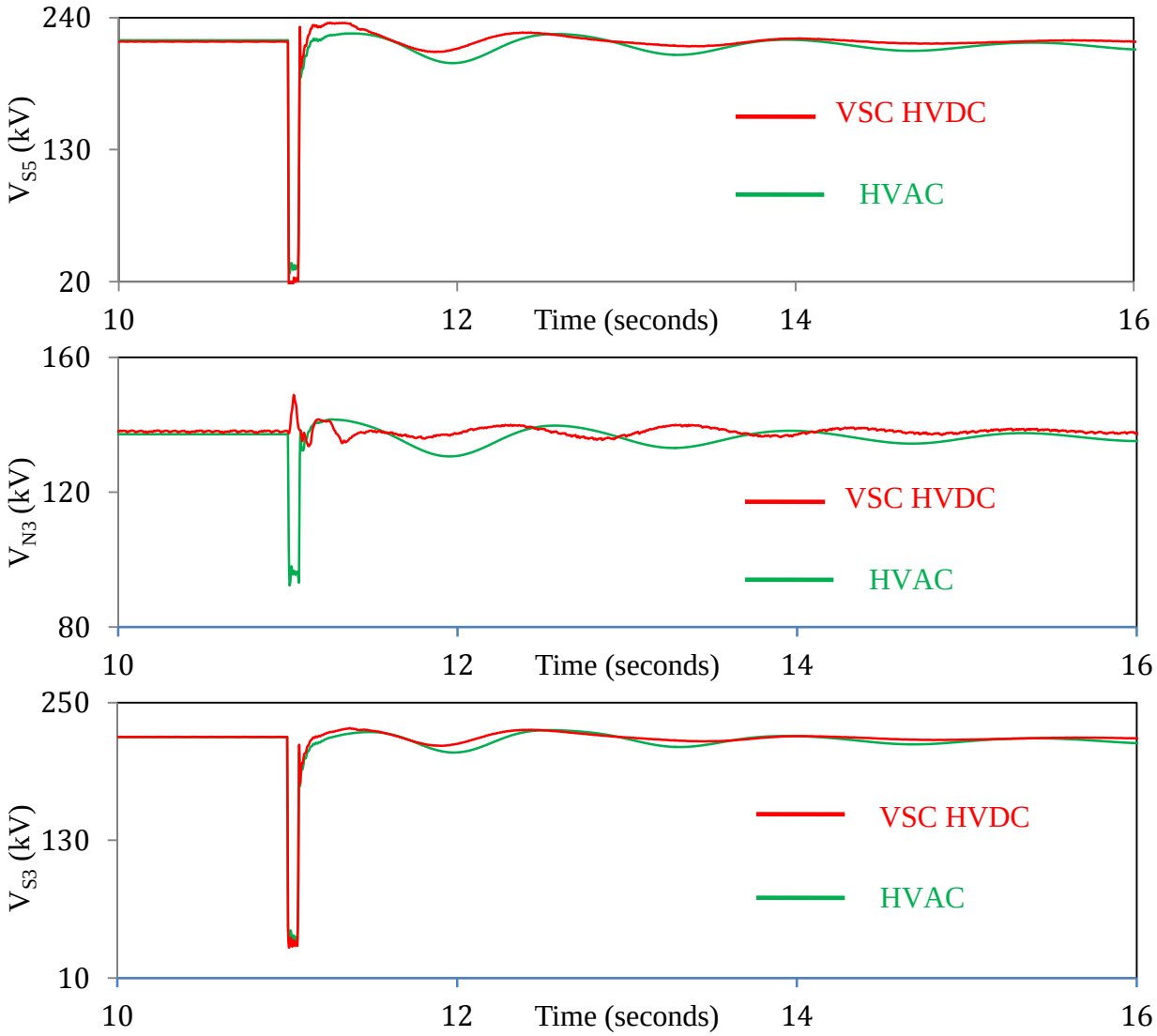

Figure 4.18: System bus voltages during and after clearing a three-cycle, three-phase fault on transmission line S2-S4 (case study 5 - POD supplemental controller is not activated).

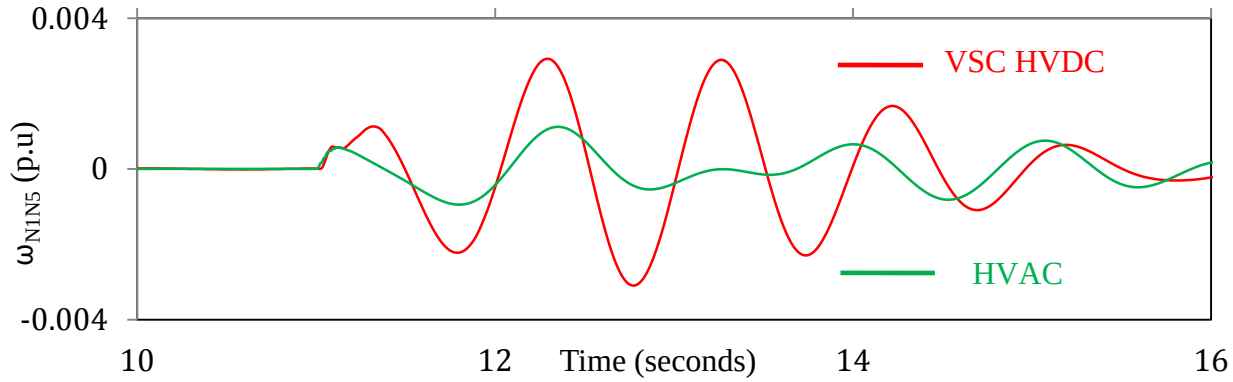

Figure 4.19: Generator speeds, measured with respect to generator G_N5 or G_S4 speed, during and after clearing a three-cycle, three-phase fault on transmission line S2-S4 (case study 5 - POD supplemental controller is not activated).

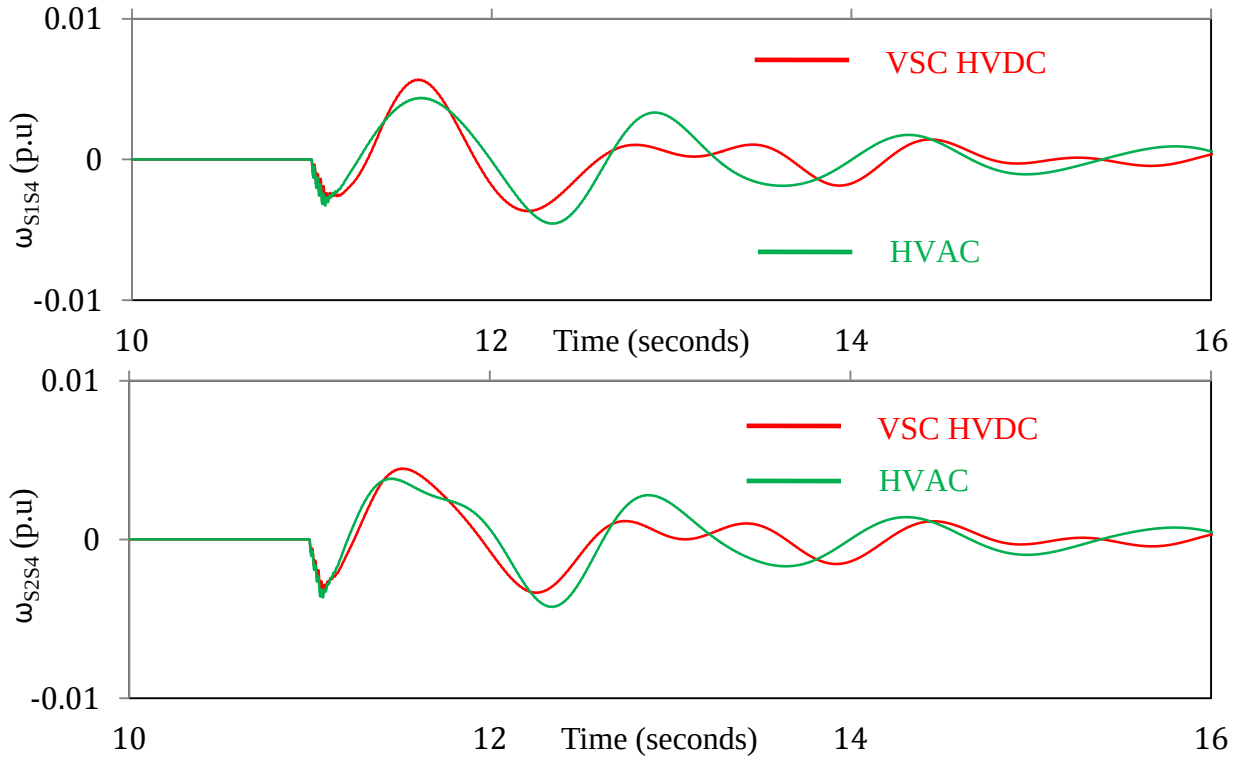

Figure 4.19: continued.

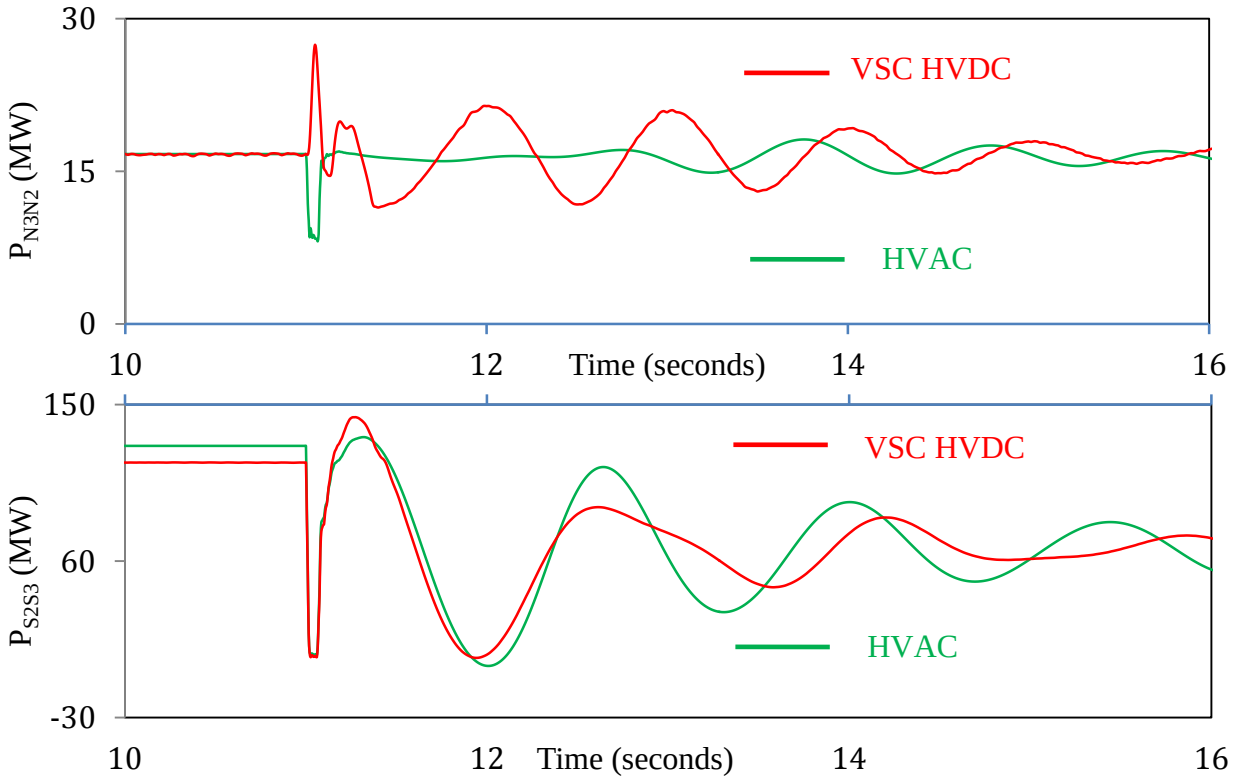

Figure 4.20: Transmission line real power flows during and after clearing a three-cycle, three-phase fault on transmission line S2-S4 (case study 5 - POD supplemental controller is not activated).

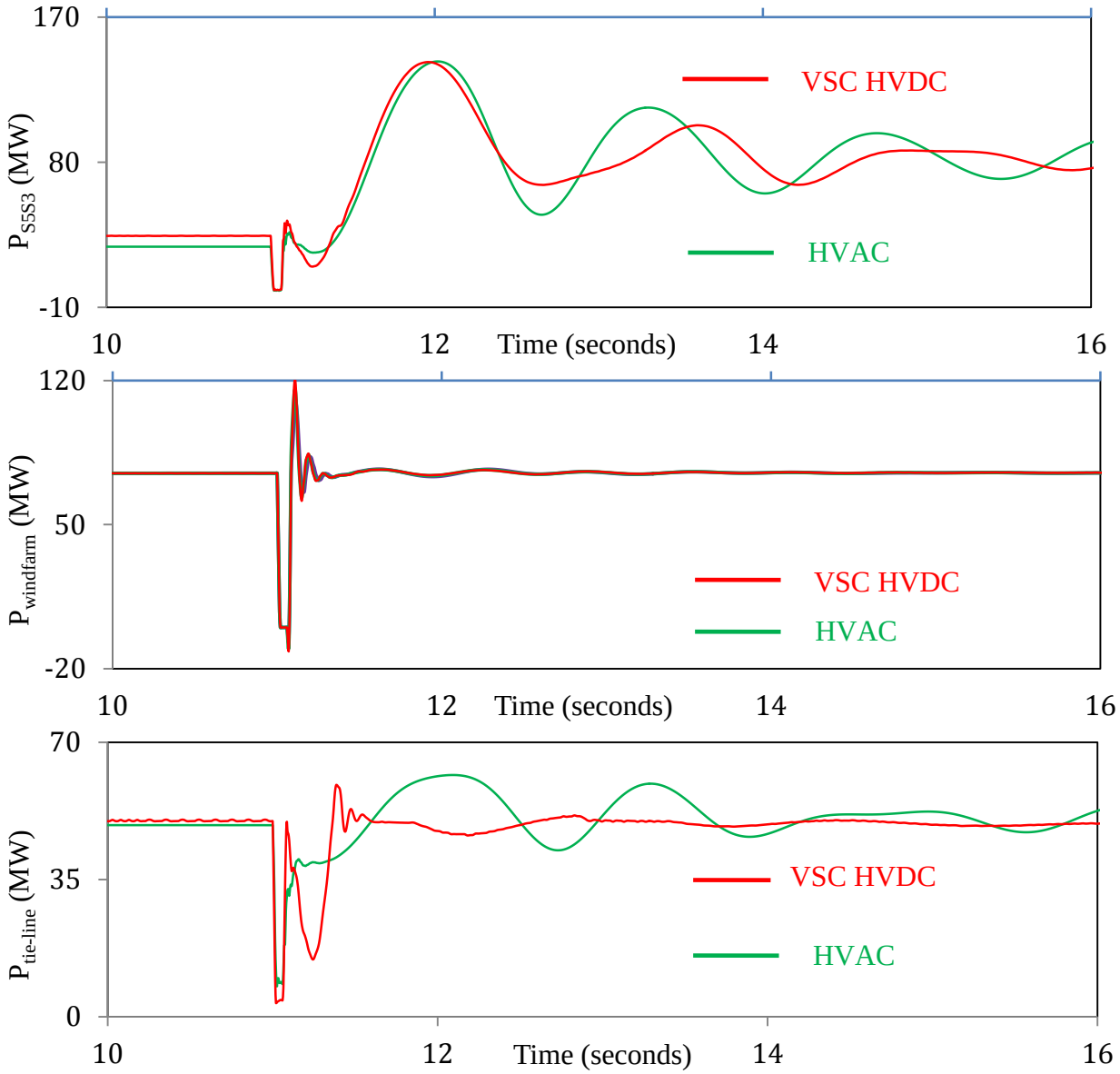

Figure 4.20: continued.

- As a result of tripping line S2-S4, more power is transmitted to load L_{S3} through transmission lines S4-S5 and S5-S3. This is evident from the increase in the real power flow through transmission line S5-S3 as shown in Figure 4.20.
- The disturbance has no adverse impact on the DFIG-based wind farm regardless of the type of the tie-line.
- The real power flow through the VSC HVDC tie-line exhibits a better damping than that in the case of the HVAC tie-line.

4.2.6 Case Study 6: Three-cycle, temporary three-phase fault at bus N5

The fault location is shown in Figure 4.21. Selected system bus voltages, generator speeds and transmission line real power flows during and after fault clearing are illustrated in Figures 4.22, 4.23 and 4.24 respectively. The following observations can be made from these figures:

- As the fault is at SaskPower North system, the magnitude of bus N3 voltage suffers a significant drop during the fault period as seen from Figure 4.22. The drops in the voltage magnitudes of buses S5 and S3 are less than that of bus N3. This is due to the fact that these two buses are located in SaskPower South system remotely from the faulted bus.

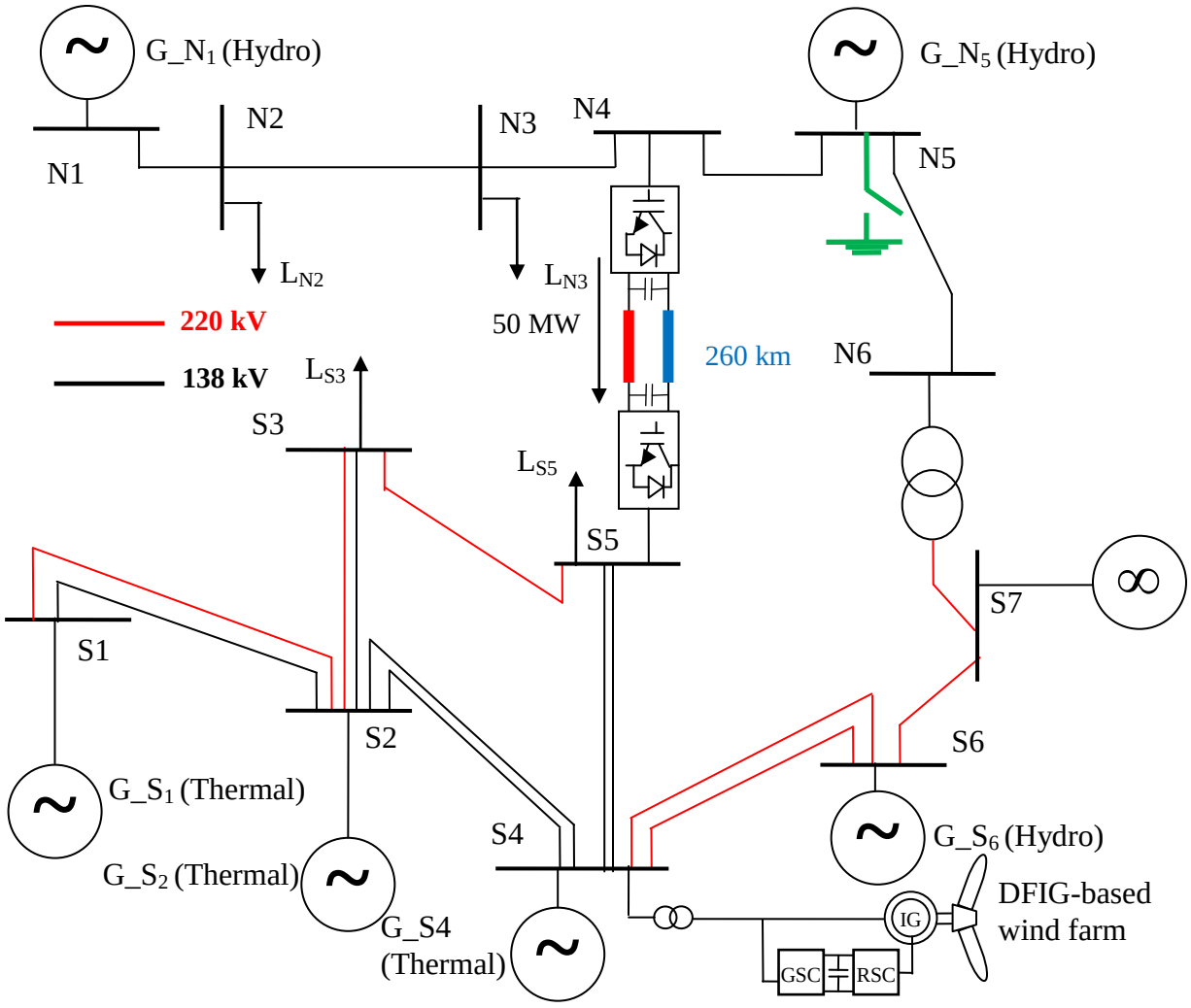

Figure 4.21: Case Study 6: three-cycle, temporary three-phase fault at bus N5 (POD supplemental controller is not activated).

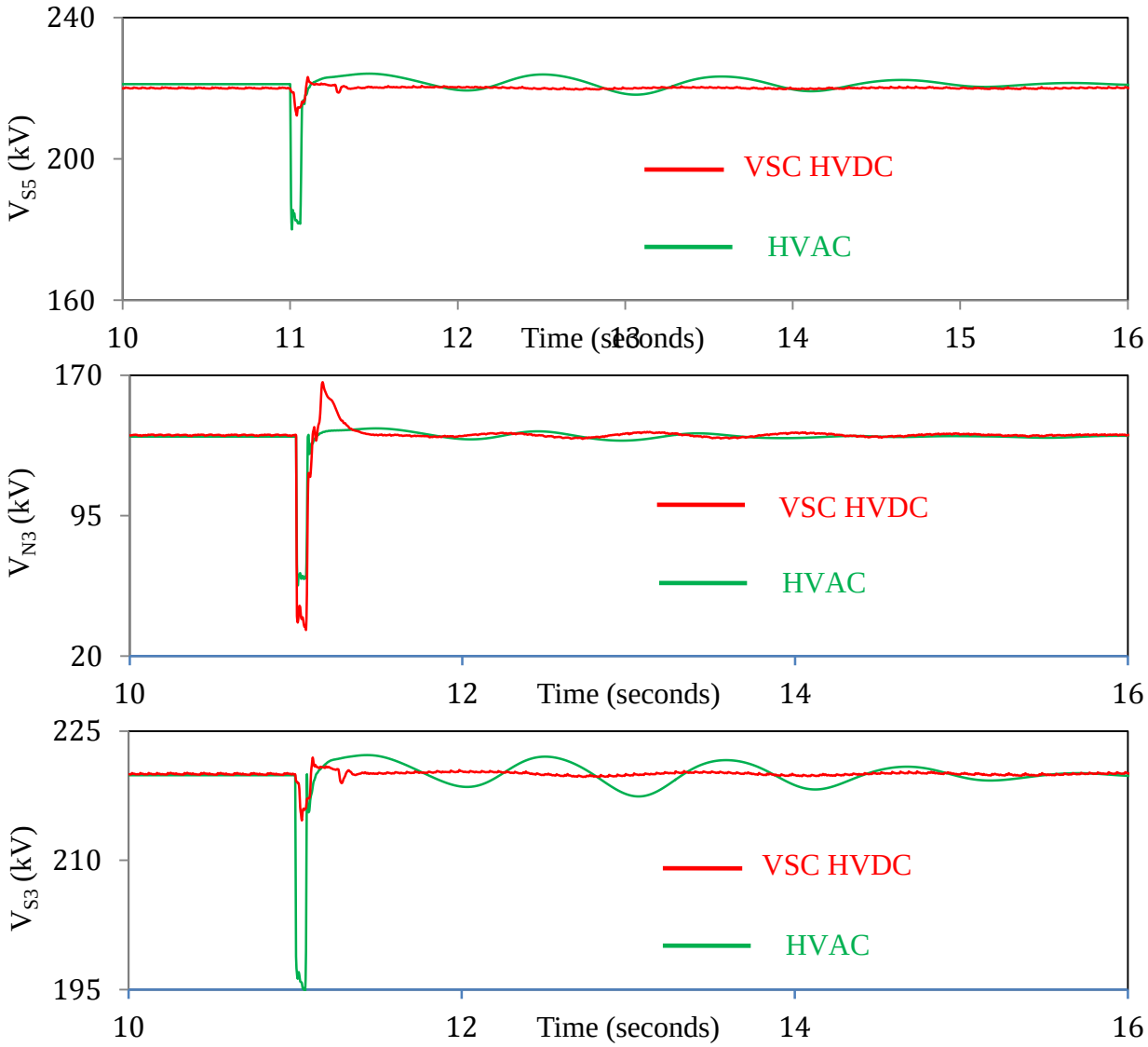

Figure 4.22: System bus voltages during and after clearing a three-cycle, temporary three-phase fault at bus N5 (case study 6 - POD supplemental controller is not activated).

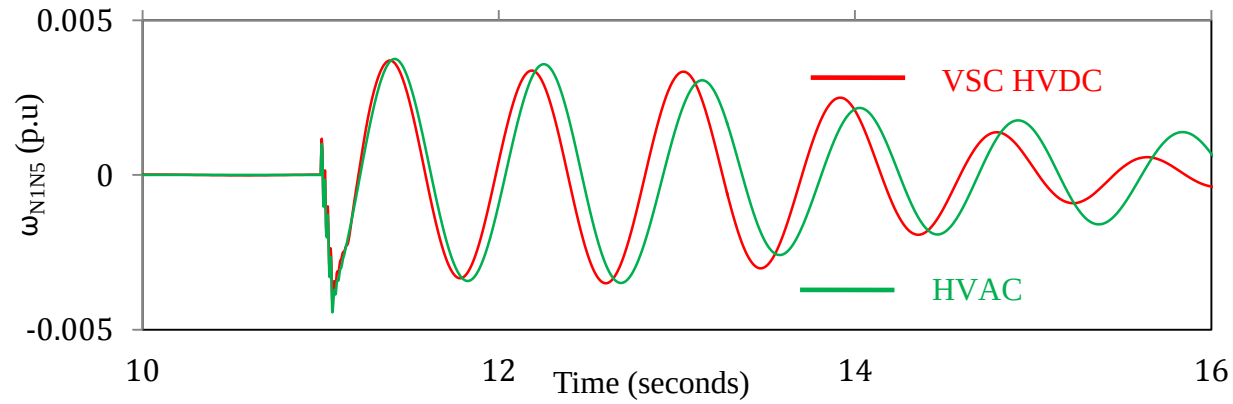

Figure 4.23: Generator speeds, measured with respect to generator G_N5 or G_S4 speed, during and after clearing a three-cycle, temporary three-phase fault at bus N5 (case study 6 - POD supplemental controller is not activated).

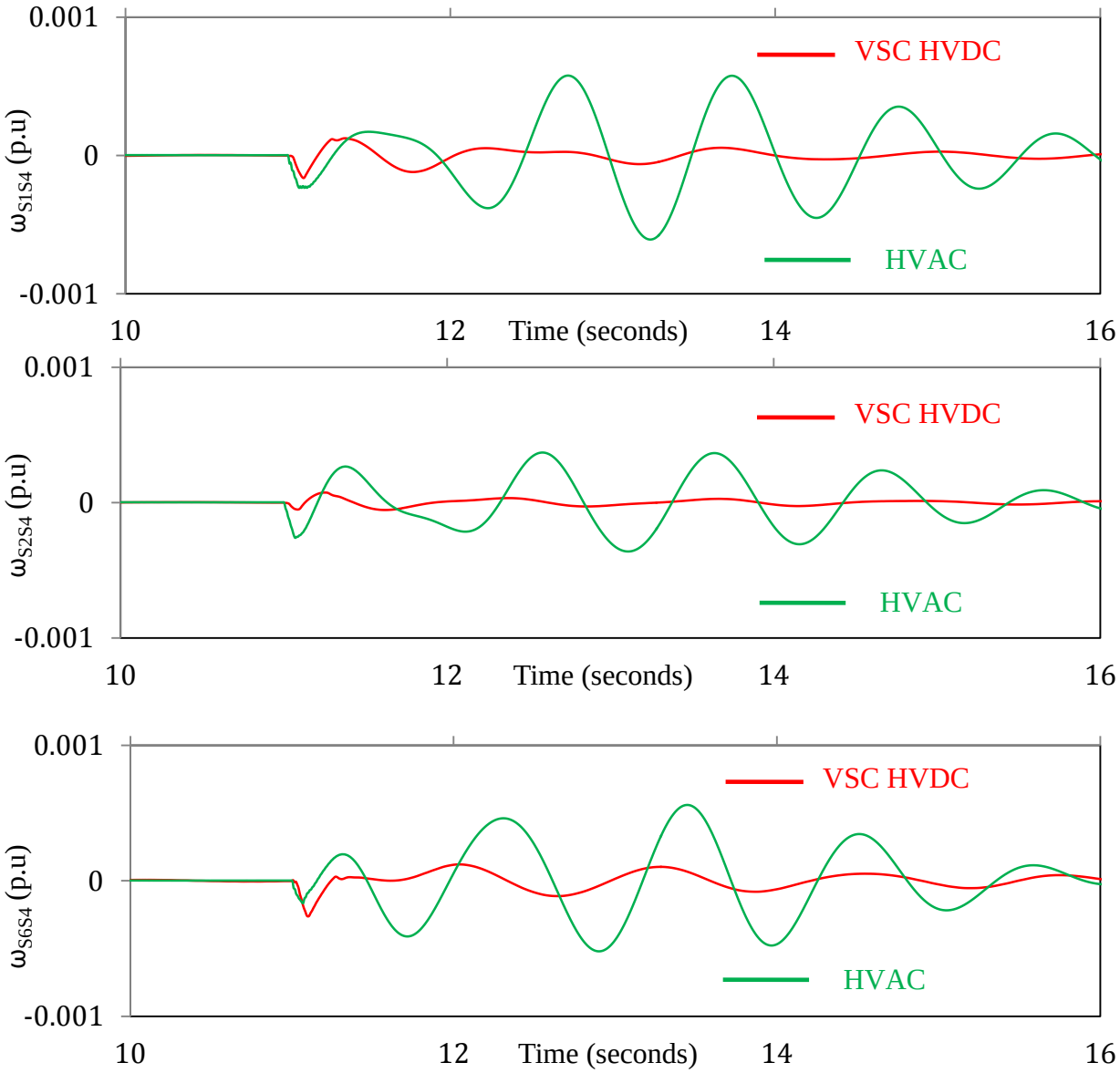

Figure 4.23: continued.

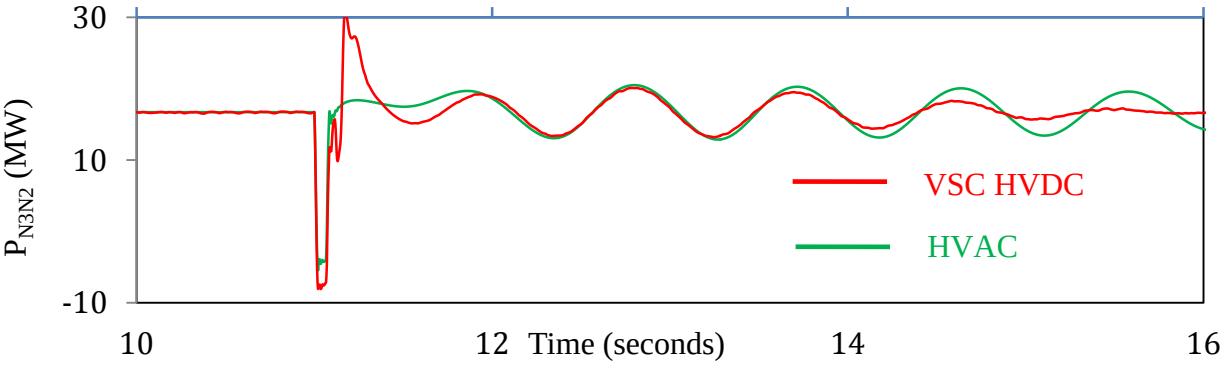

Figure 4.24: Transmission line real power flows during and after clearing a three-cycle, temporary three-phase fault at bus N5 (case study 6 - POD supplemental controller is not activated).

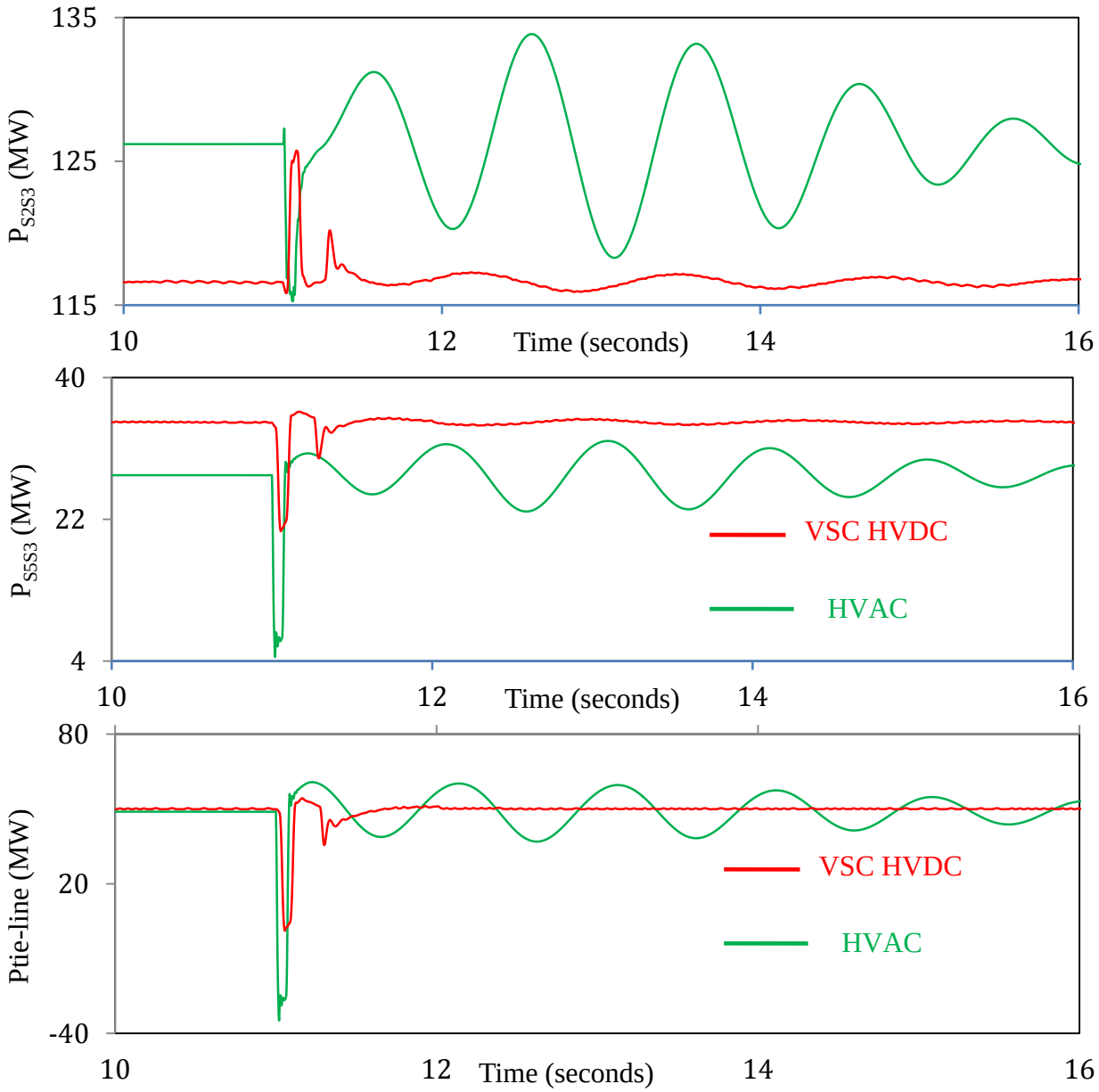

Figure 4.24: continued.

- As the VSC HVDC link dynamically de-couple SaskPower North and South systems, the South system generator speeds (ω_{S1S4}, ω_{S2S4} and ω_{S6S4}) are more stabilized than in the case of the HVAC tie-line as seen from Figure 4.23.
- The system bus voltages and the transmission line real power flows in the case of the VSC HVDC link exhibit better damping than in the case of the HVAC tie-line.

4.2.7 Case Study 7: Three-cycle, temporary three-phase fault on transmission line N6-S7

The fault location is shown in Figure 4.25. Selected system bus voltages, generator speeds and transmission line real power flows during and after fault clearing are illustrated in Figures 4.26, 4.27 and 4.28 respectively. The following observations can be made from these figures:

- From Figure 4.28, it can be seen that the real power flow through the VSC HVDC tie-line exhibits a better damping than that in the case of the HVAC tie-line.

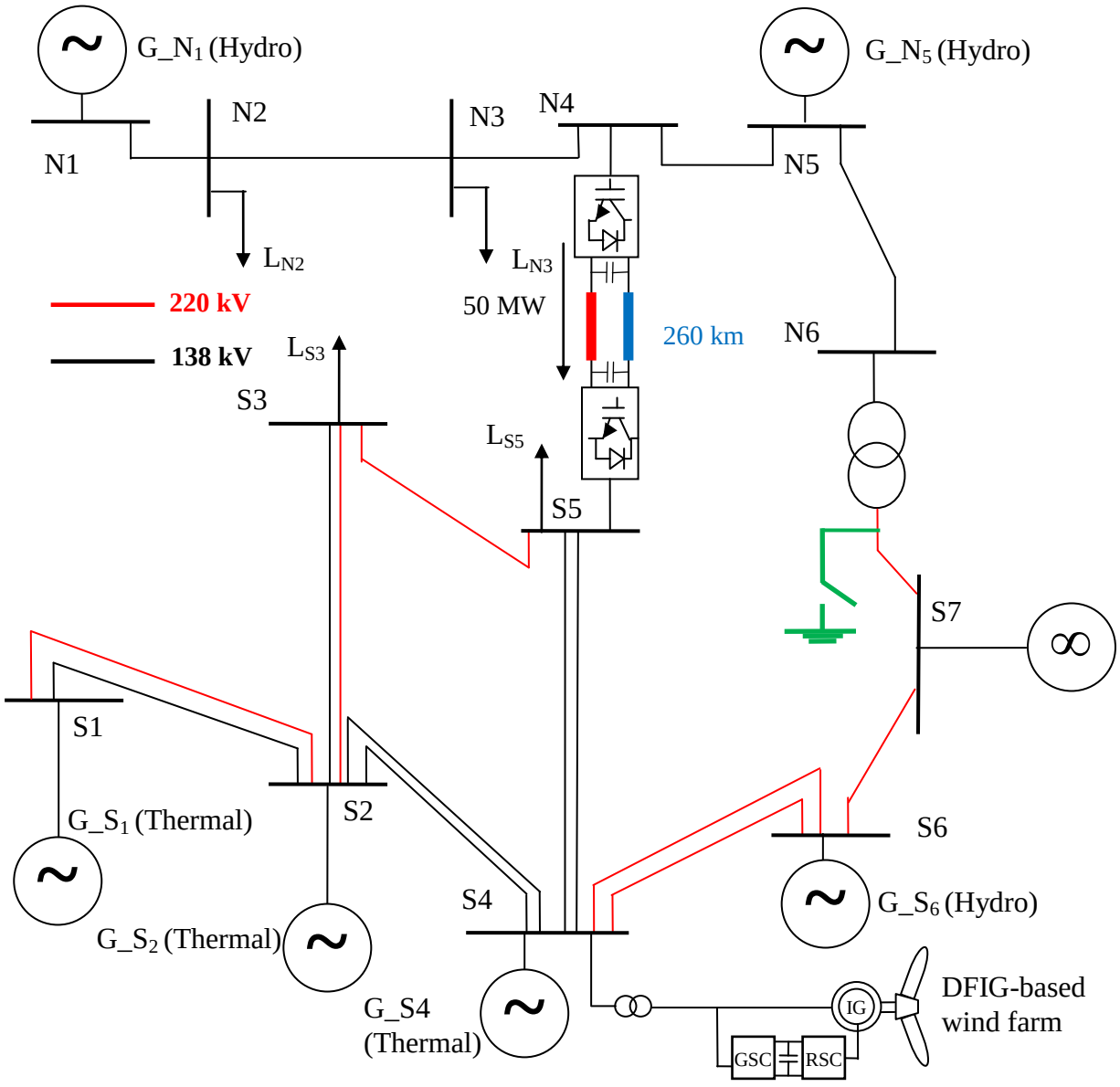

Figure 4.25: Case Study 7: three-cycle, temporary three-phase fault on transmission line N6-S7 (POD supplemental controller is not activated).

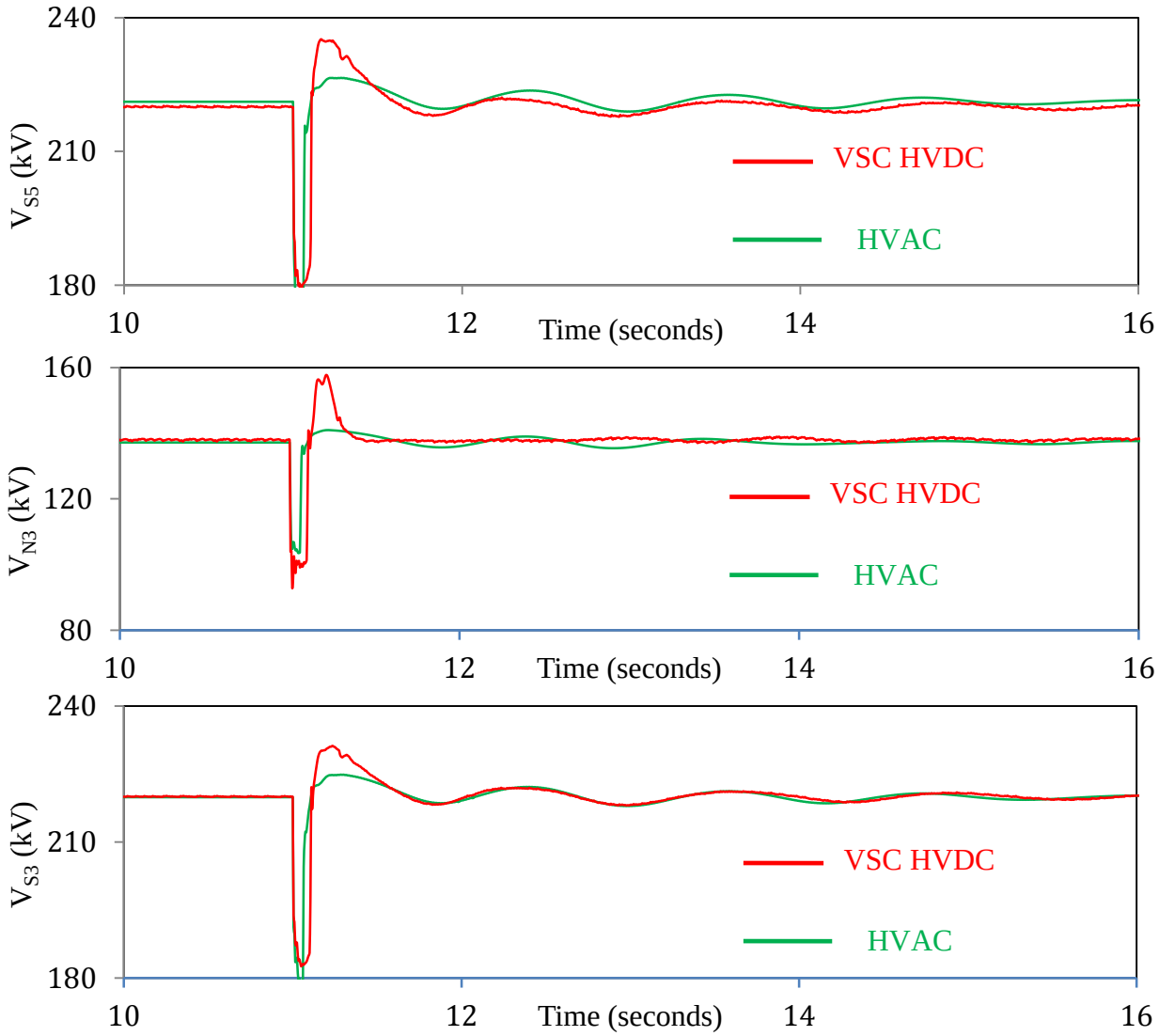

Figure 4.26: System bus voltages during and after clearing a three-cycle, temporary three-phase fault on transmission line N6-S7 (case study 7 - POD supplemental controller is not activated).

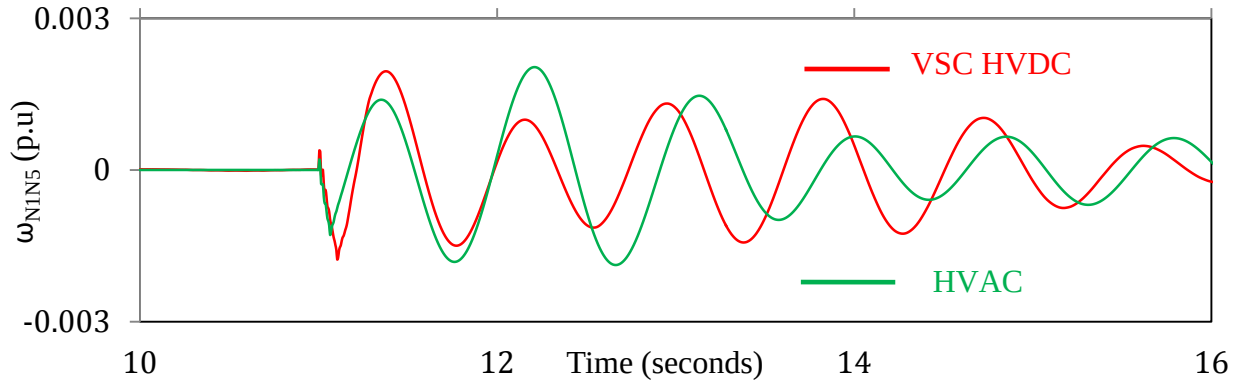

Figure 4.27: Generator speeds, measured with respect to generator G_N5 or G_S4 speed, during and after clearing a three-cycle, temporary three-phase fault on transmission line N6-S7 (case study 7 - POD supplemental controller is not activated).

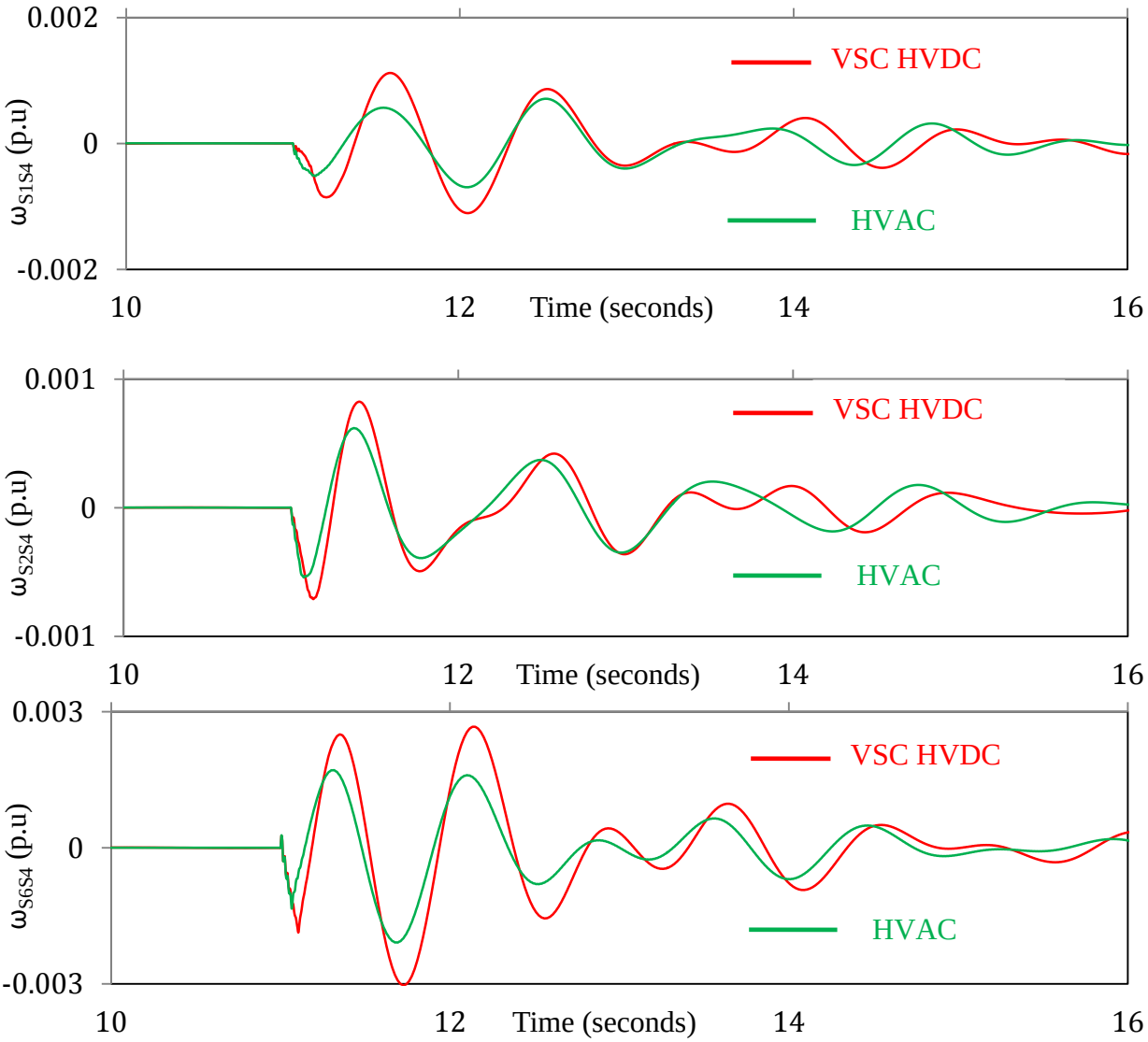

Figure 4.27: continued.

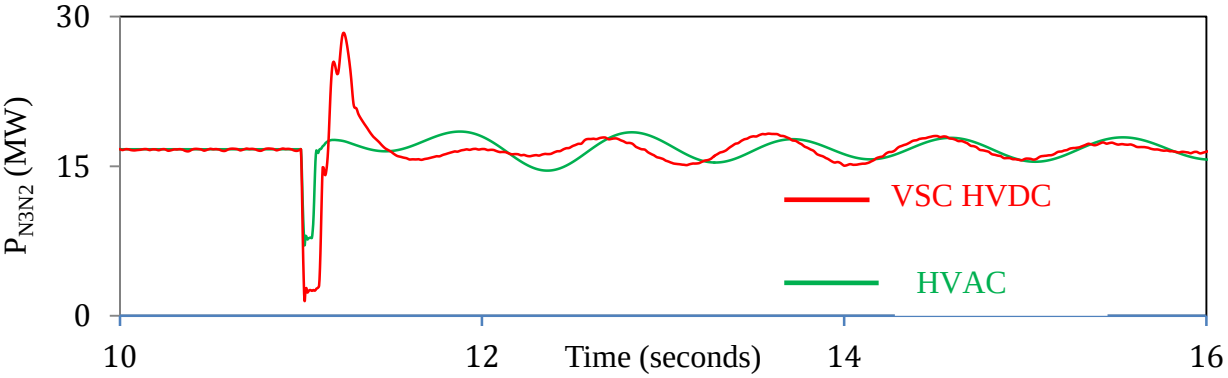

Figure 4.28: Transmission line real power flows during and after clearing a three-cycle, temporary three-phase fault on transmission line N6-S7 (case study 7 - POD supplemental controller is not activated).

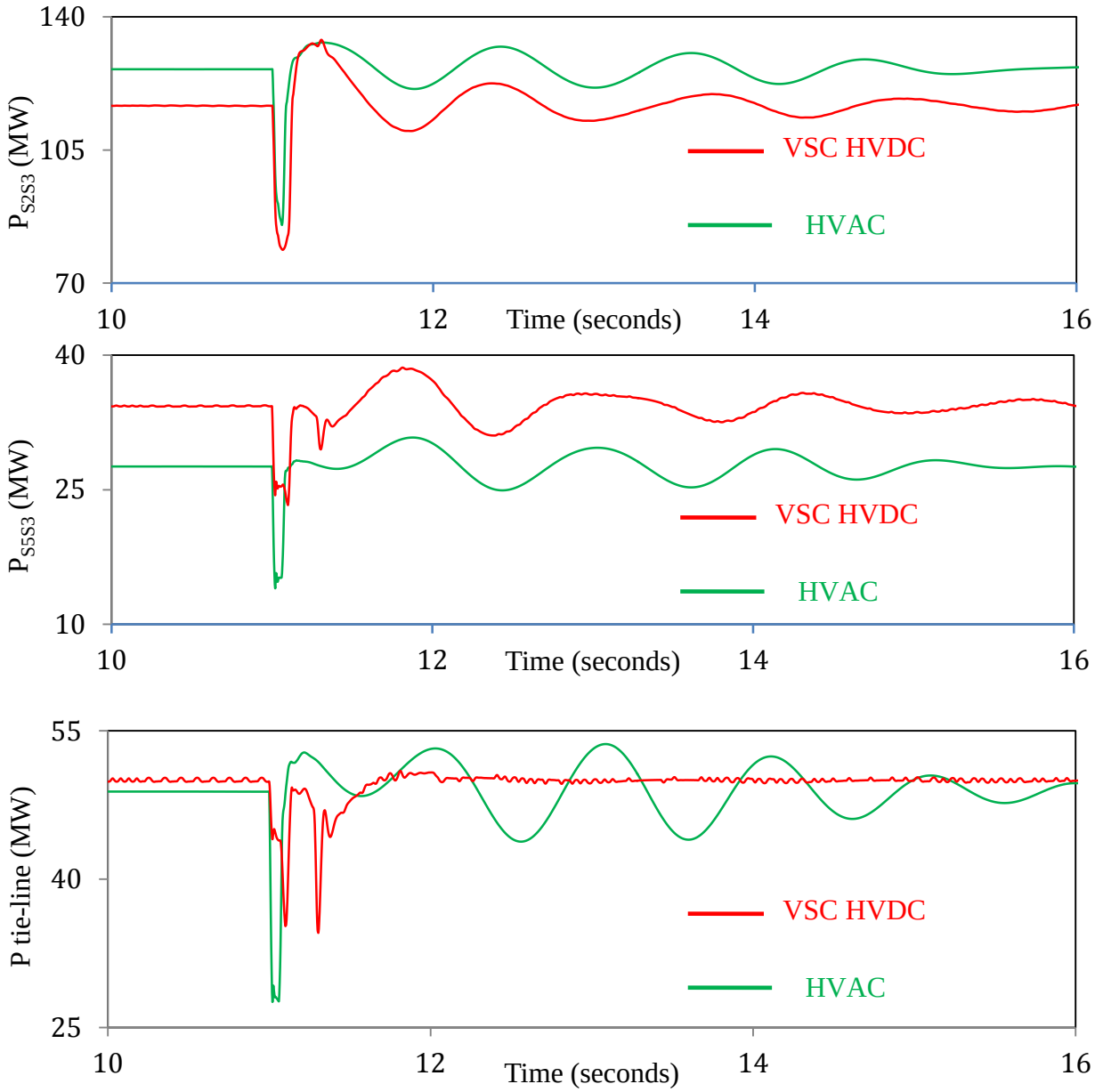

Figure 4.28: continued.

- The oscillations in the system bus voltages, generator speeds and transmission line real power flows exhibit the same damping behaviour in both the VSC HVDC and HVAC tie-lines. It should be noticed, however, that the disturbance has a very small impact on the system dynamics regardless of the type of the tie-line.

4.3 POD Supplemental Controller

The case studies presented in Section 4.2 reveal that the VSC HVDC tie-line exhibits a superior dynamic performance over a HVAC tie-line. It worth noting here that in these case studies, the VSC HVDC POD supplemental controller is disabled (not activated). In this section, the performance of such a controller is examined when it is activated in case studies 3 and 7.

4.3.1. Case Study 3: Three-cycle, three-phase fault on transmission line N6-S7; SaskPower North system loses its connection with Manitoba grid - POD supplemental controller is activated

The fault location is shown in Figure 4.9. As it is discussed before, tripping line N6-S7 results in that SaskPower North system loses its connection with Manitoba grid. Selected system bus voltages and transmission line real power flows during and after fault clearing (line tripping) are illustrated in Figures 4.29 and 4.30 respectively. The time responses of the generator speed deviations are not shown in this case study as their maximum deviation is relatively small (± 0.003 p.u. speed). As it can be seen from these figures, the contribution of the VSC HVDC POD supplemental controller to the damping of system oscillations is, generally, insignificant even though some reductions in the peak values of some bus voltages and real power flows are achieved.

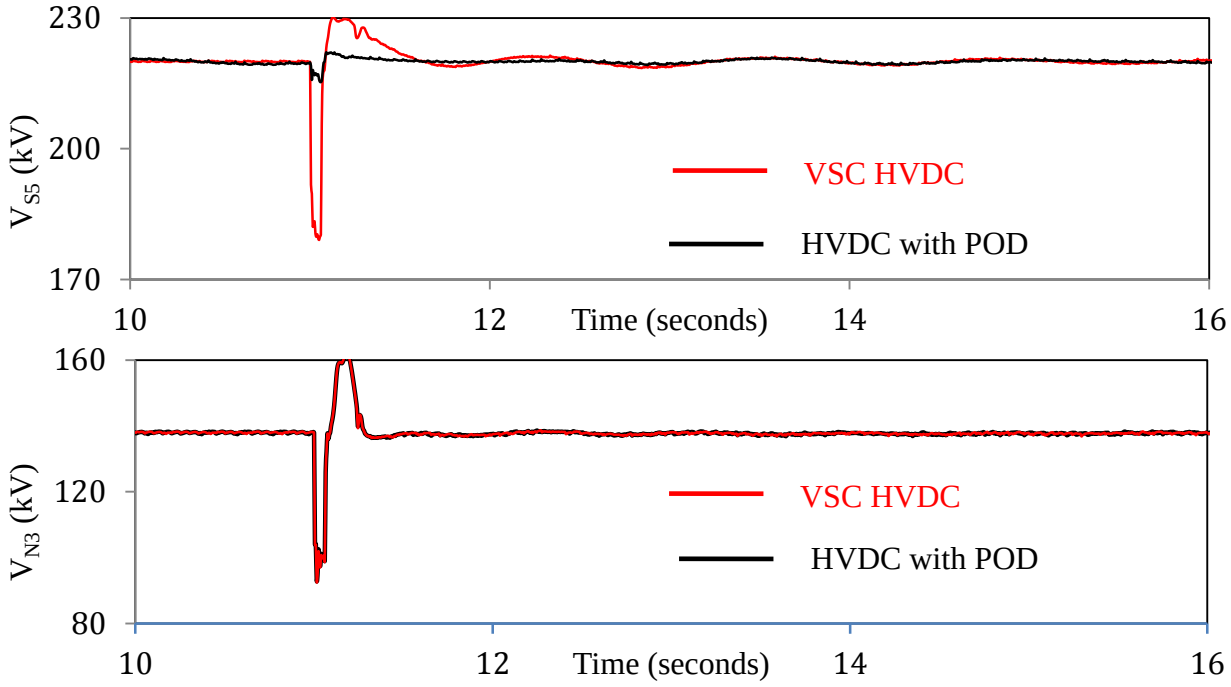

Figure 4.29: System bus voltages during and after clearing a three-cycle, three-phase fault on transmission line N6-S7 (case study 3 - POD supplemental controller is activated).

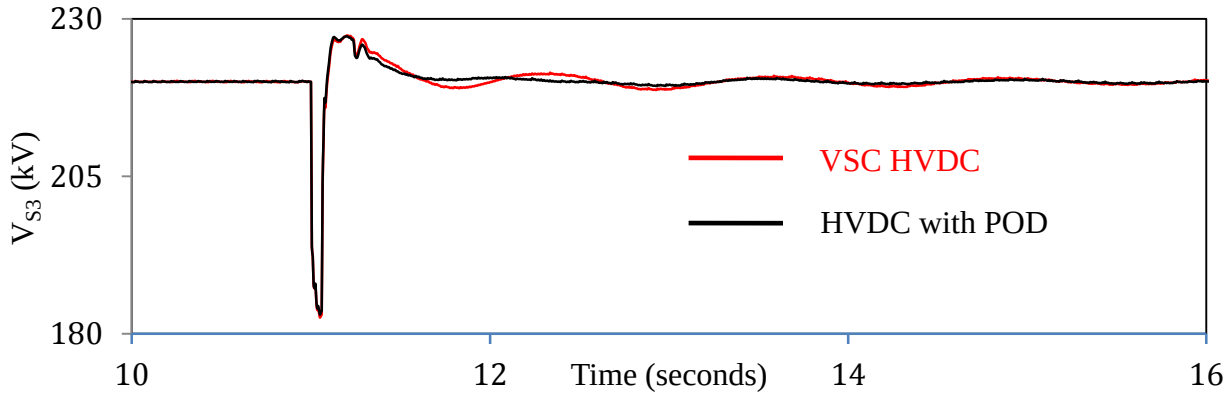

Figure 4.29: continued.

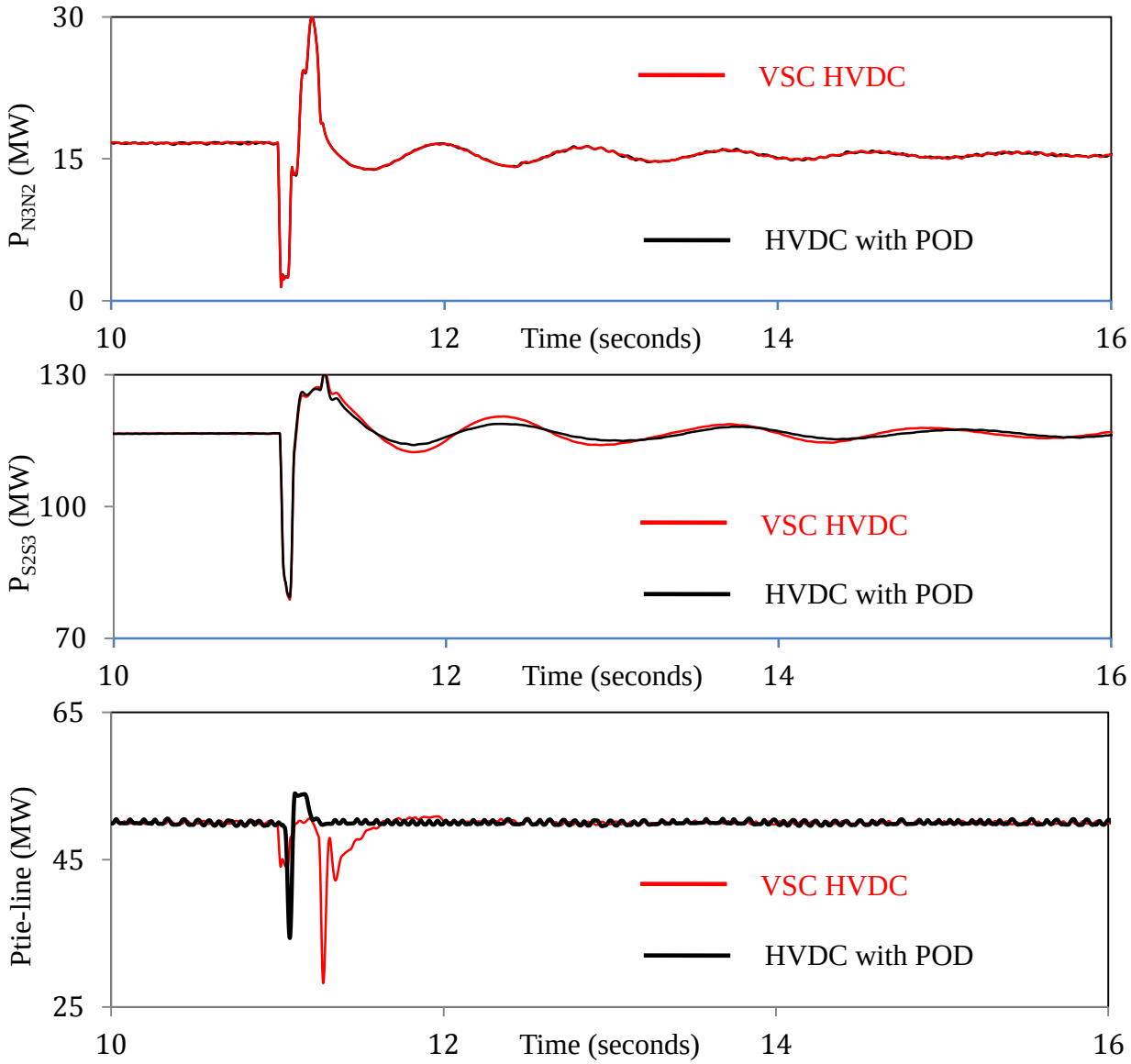

Figure 4.30: Transmission line real power flows during and after clearing a three-cycle, three-phase fault on transmission line N6-S7 (case study 3 - POD supplemental controller is activated).

4.3.2. Case Study 7: Three-cycle, temporary three-phase fault on transmission line N6-S7; POD supplemental controller is activated

The fault location is shown in Figure 4.25. Selected system bus voltages and transmission line real power flows during and after fault clearing are illustrated in Figures 4.29 and 4.30 respectively. Similar to case study 3, the time responses of the generator speed deviations are not shown in this case study as their maximum deviation is relatively small (± 0.003 p.u. speed). As it can be seen from these figures, the contribution of the VSC HVDC POD supplemental controller to the damping of system oscillations is still, generally, insignificant even though some reductions in the peak values of some bus voltages and real power flows are achieved.

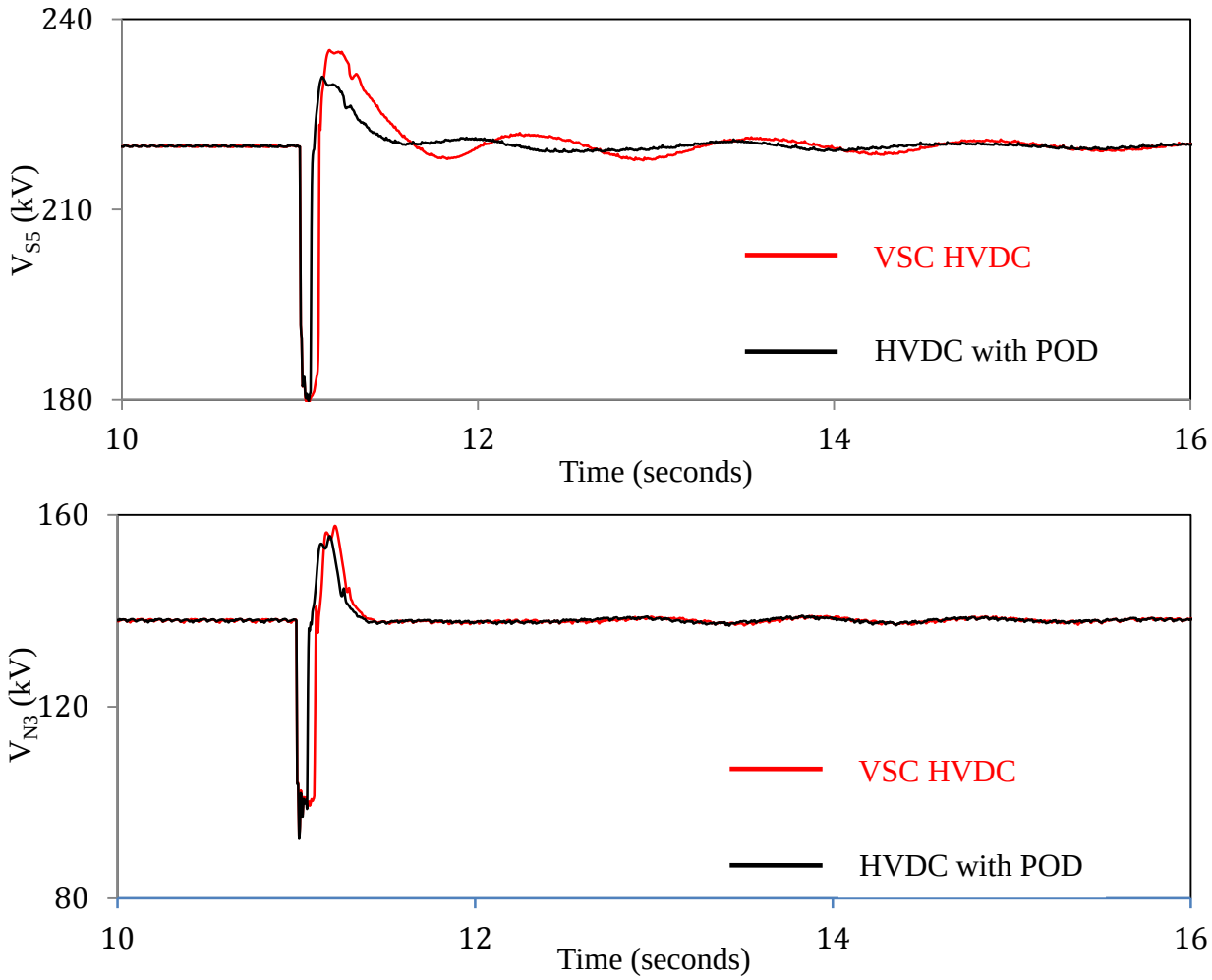

Figure 4.31: System bus voltages during and after clearing a three-cycle, temporary three-phase fault on transmission line N6-S7 (case study 7 - POD supplemental controller is activated).

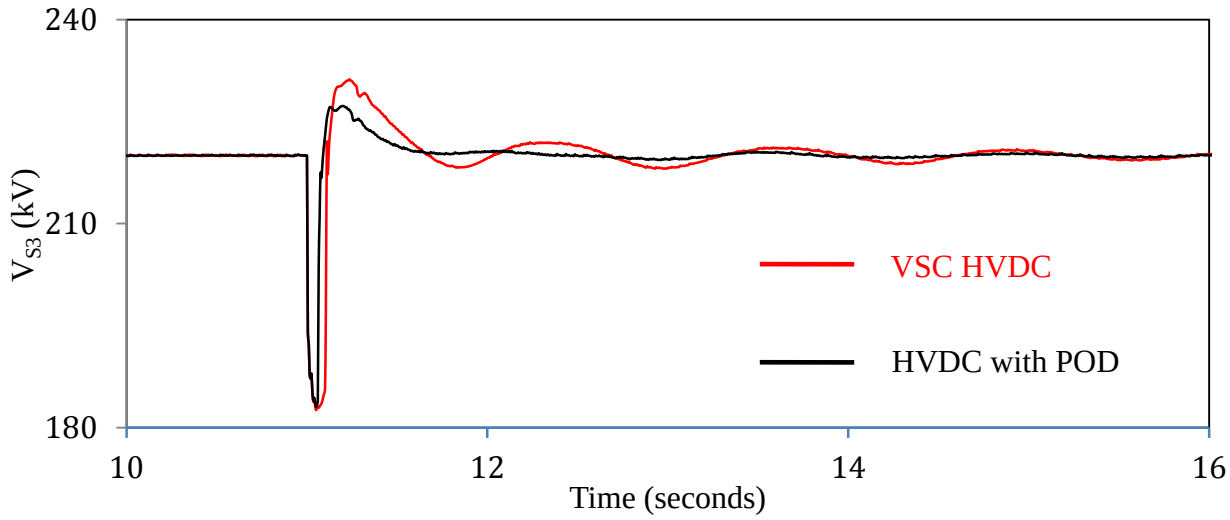

Figure 4.31: continued.

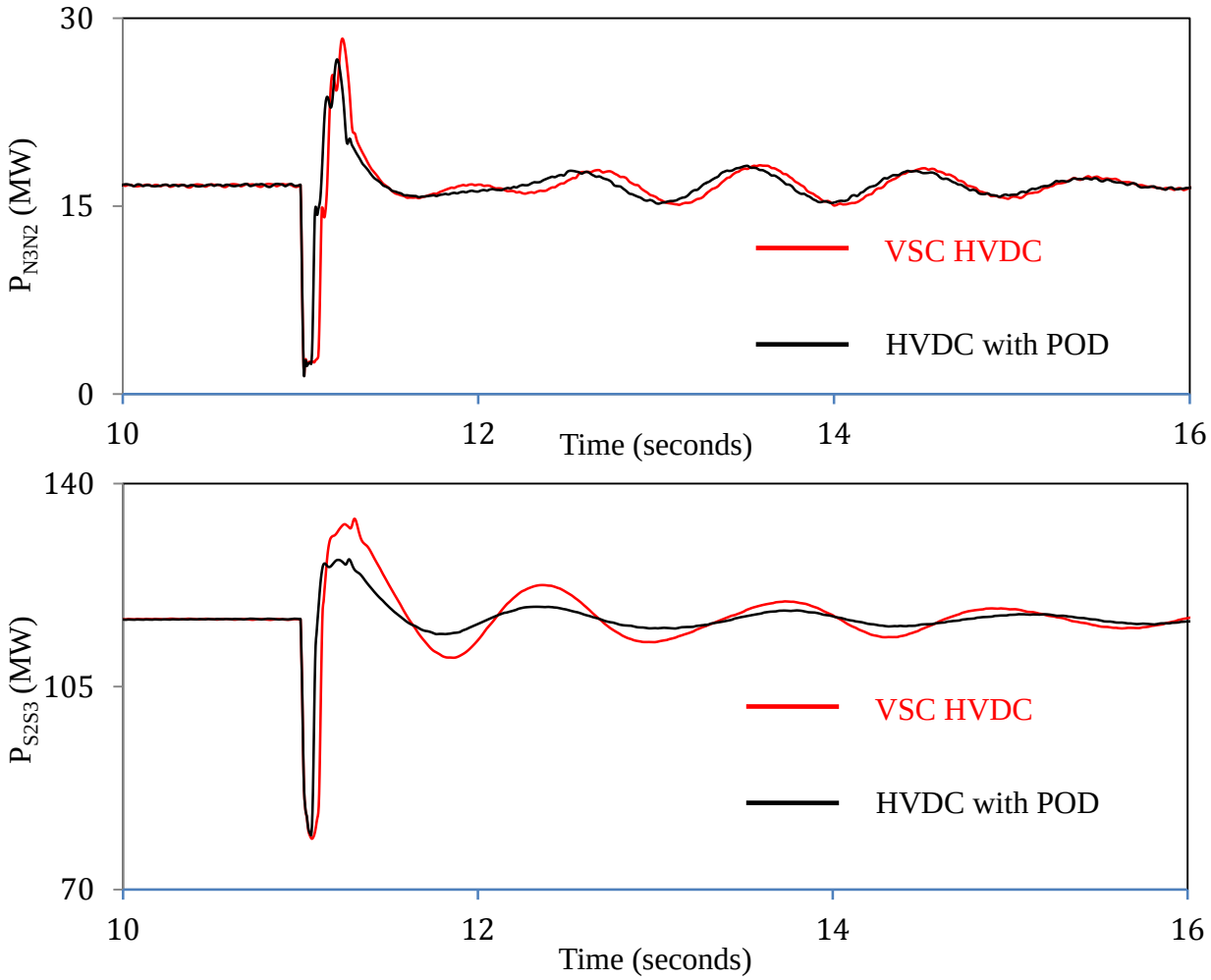

Figure 4.32: Transmission line real power flows during and after clearing a three-cycle, temporary three-phase fault on transmission line N6-S7 (case study 7 - POD supplemental controller is activated).

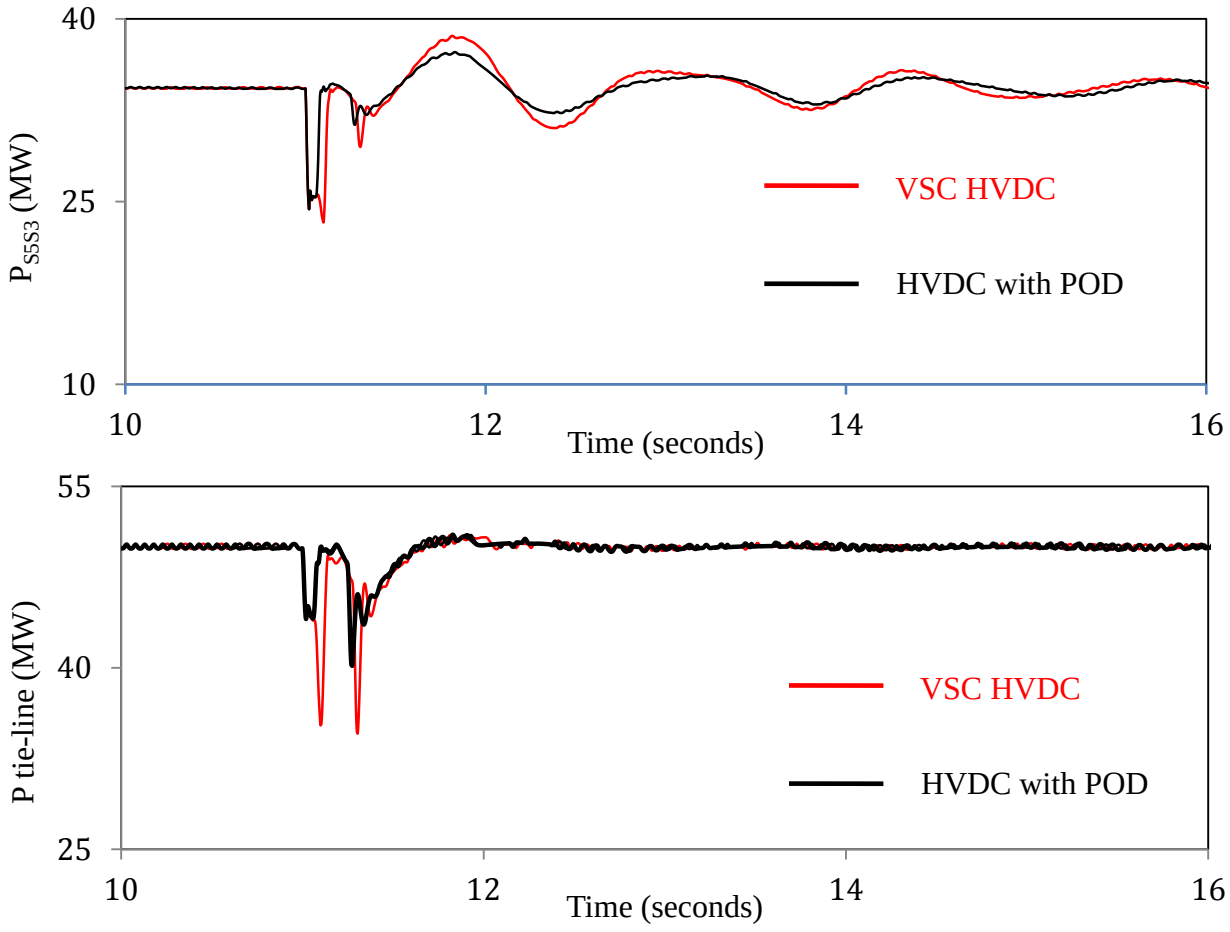

Figure 4.32: continued.

4.4 Summary

In this chapter, the performances of the VSC HVDC link and its POD supplemental controller are investigated through several time-domain simulation case studies of three-cycle, three-phase faults at different system locations of SaskPower integrated system. The results of these investigations have shown that the VSC HVDC tie-line exhibits a superior dynamic performance over a HVAC tie-line. Regarding the performance of the VSC HVDC POD supplemental controller, the results of two case studies have shown that, in general, the contribution of such a supplemental controller to the damping of system oscillations is insignificant even though some reductions in the peak values of some bus voltages and real power flows are achieved.

Chapter 5

SUMMARY AND CONCLUSIONS

5.1 Summary

Connecting SaskPower North and South systems would provide many technical and economic benefits. The tie-line would increase the power exchange between the North and the South system as well as between SaskPower and Manitoba grids. The interconnection would also improve the reliability of the entire SaskPower gird because catastrophic multiple outages can be prevented through emergency power exchange.

The main objective of this research work was to investigate the dynamic performance of a proposed 260 km, ± 110 kV, 50 MW VSC HVDC tie-line that would connect SaskPower North and South systems. The potential problems that might arise due to such an interconnection, namely power flow control and low-frequency oscillations was studied and quantified and a proposed feasible solution should be established. In this context, the effectiveness of the HVDC and a proposed Power Oscillations Damping (POD) controller in damping power system oscillations in the tie-line were investigated through comprehensive time-domain simulation studies on a test system that reasonably represent SaskPower North system and the Northern part of its South system. Although SaskPower real system data were not used, it is believed that the observations and conclusions drawn from this research work would be very similar to those reached with SaskPower real system data

In Chapter 1, the fundamental benefits and the problems arising from grid interconnections are introduced. A brief introduction to SaskPower North and South systems and the objective of the research are also presented in this chapter.

In Chapter 2, the system used for the investigations conducted in this thesis is described and the detailed dynamic models of its individual components are also presented in this chapter. The results of the digital time-domain simulations of a case study for the system during a three-phase fault are presented at the end of this chapter.

In Chapter 3, the load flow profiles of the North and South systems as well as the interconnected North and South systems (with HVAC and HVDC tie-lines) are examined and important conclusions are drawn. The structures of the HVDC main controller as well as the POD supplemental controller and its possible stabilizing signals are also presented in this chapter.

In Chapter 4, the effectiveness of the VSC HVDC main controller in damping power system oscillations is demonstrated through several time-domain simulation case studies. The performance of the POD supplementary controller with possible different stabilizing signals in enhancing the damping of the system oscillations is also presented in this chapter.

5.2 Conclusions

The studies conducted in this thesis yield the following conclusions:

1. Both HVAC and HVDC tie-lines can be used for interconnecting SaskPower North and South systems. The VSC HVDC tie-line has, however, the capability in keeping the pre-connection system load flow unchanged whereas the HVAC tie-line would slightly increase the pre-connection South system load flow.

2. The low-frequency oscillations that are observed in SaskPower integrated system have a frequency in the vicinity of 0.67 to 0.7 Hz.

3. A major advantage of an HVDC tie-line over an HVAC one is that it de-couples dynamically SaskPower North and South systems. In other words, the impacts of disturbances in one system are not significantly felt by the other system.

4. In the case of the HVAC tie-line, the system loses its stability when SaskPower North system loses its connection with Manitoba grid. With an HVDC tie-line, the system stability is maintained during the same contingency.

5. In general, the VSC HVDC controller has shown to be very effective in damping the low-frequency oscillations in SaskPower integrated system oscillations.

6. Generators G_S1 and G_S4 speeds (ω_{S1} , ω_{S4}) and generators G_N1 and G_N5 load angles, measured with respect to generator G_S4 load angle, are found to be appropriate stabilizing signals for the VSC HVDC supplemental controller.

7. In general, the contribution of the VSC HVDC POD supplemental controller to the damping of the system oscillations is insignificant even though some reductions in the peak values of some bus voltages and real power flows could be achieved.

This thesis is a stepping-stone in the direction of more detailed research on the dynamic performance of the future SaskPower VSC HVDC interconnection. It is hoped that the research work documented in this thesis would provide the future direction for studying and analyzing other technical issues that might be impacted by the new interconnection.

REFERENCES

[1] M. Klein, G.J. Rogers and P. Kundur, "A fundamental study of inter area oscillations in power systems," IEEE Transactions on Power Systems, August 1991, Vol. 6, pp. 914-921.

[2] P.M. Anderson and A.A. Fouad, *Power System Control and Stability*, IEEE Press, 1994.

[3] N.G. Hingorani and L. Gyugyi, *Understanding FACTS: Concepts and Technology of Flexible AC Transmission Systems*, New York, IEEE Press, 2000.

[4] C. Gama, "Brazilian North-South Interconnection Control-Application and Operating Experience with a TCSC," Proceedings of the 1999 IEEE PES Summer Meeting, Edmonton, Alberta, Canada, 1999, Vol. 2, pp. 1103-1108.

[5] K. Meah and S. Ula, "Comparative Evaluation of HVDC and HVAC Transmission System," IEEE Power Engineering Society General Meeting, Tampa, Florida, U.S, 2007, pp. 1-5.

[6] B.R. Andersen, "HVDC Transmission – Opportunities and Challenges," The 8th IEE International Conference on AC and DC Power Transmission, London, United Kingdom, March 2006, pp. 24-29.

[7] A. Lindberg and T. Larsson, "PWM and control of three level voltage source converters in an HVDC back-to-back station," The 6th IEE International Conference on AC and DC Power Transmission, London, United Kingdom, May 1996, pp. 297 – 302.

[8] J. Peralta, H. Saad, S. Dennetière, J. Mahseredjian and S. Nguefeu, "Detailed and Averaged Models for a 401-level MMC-HVDC System," IEEE Transactions on Power Delivery, July 2012, Vol.27, pp.1501-1508.

[9] A. Lesnicar and R.Marquardt, "An innovative modular multilevel converter topology suitable for a wide power range," IEEE Power Tech Conference Proceedings, Bologna, Italy, Jun. 2003, Vol.3.

[10] H. Patel and V.K. Sood, "Modeling of Voltage Source Converter Based HVDC System in EMTP-RV," IEEE Electric Power and Energy Conference (EPEC), Halifax, Canada, Aug. 2010, pp. 1-6.

[11] G.J Rogers, *Power system oscillation,* Massachusetts, Kluwer Academic Publishers, 2000, pp 1-6.

[12] Sushan Pan, "Damping Power System Oscillations Using a Phase Imbalanced Hybrid Series Capacitive Compensation Scheme," M.Sc Thesis, University of Saskatchewan, October 2010.

[13] P. Kundur, *Power system stability and control*, New York, McGraw-Hill, 1994, pp. 46-136.

[14] Y. Yu, *Electric Power System Dynamics*, New York, Academic Press, 1983.

[15] O.I. Elgerd, *Electrical Energy Systems Theory*, McGraw-Hill, 1971.

[16] B. Chaudhuri, S. Ray and R. Majumder, "Robust low-order controller design for multi-modal power oscillation damping using flexible AC transmission systems devices," IET Generation, Transmission & Distribution, May 2009, Vol. 3, pp. 448-459.

[17] T. Abdelazim and O.P. Malik, "An adaptive power system stabilizer using self-learning fuzzy systems," IEEE Power Engineering Society General Meeting, Toronto, Canada, July 2003, Vol.3, pp.1715-1720.

[18] Kundur, P., *Power system stability and control*, New York, McGraw-Hill, 1994, pp. 403-500.

[19] L. Wang and K.H. Wang, "Dynamic Stability Analysis of a DFIG-Based Offshore Wind Farm Connected to a Power Grid through an HVDC Link," IEEE Transactions on Power Systems, August 2011, Vol. 26, pp. 1501-1510.

[20] Y. Lei, A. Mullane, G. Lightbody and R. Yacamini, "Modeling of the Wind Turbine with a Doubly Fed Induction Generator for Grid Integration Studies," IEEE Transactions on Energy Conversion, March 2006, Vol. 21, pp. 257-264.

[21] C. Zhu, L. Fan and M. Hu, "Control and Analysis of DFIG-Based Wind Turbines in a Series Compensated Network for SSR Damping," 2010 IEEE Power and Energy Society General Meeting, Minneapolis, U.S, July 2010, pp. 1-6.

[22] L. Yang, Z. Xu, J. Ostergaard, Z.Y. Dong, K.P. Wong and X. Ma, "Oscillatory Stability and Eigenvalue Sensitivity Analysis of a DFIG Wind Turbine System," IEEE Transactions on Energy Conversion, March 2011, Vol. 26, pp. 328-339.

[23] L. Fan, R. Kavasseri, Z.L Miao and C. Zhu, "Modeling of DFIG-Based Wind Farms for SSR Analysis," IEEE Transactions on Power Delivery, October 2010, Vol. 25, pp. 2073-2082.

[24] Jiping Zhang, "Power System Dynamic Enhancement Using Phase Imbalance Series Capacitive Compensation and Doubly Fed Induction Generator-Based Wind Farms," M.Sc Thesis University of Saskatchewan, April 2013.

APPENDIX A

DATA OF THE SYSTEM UNDER STUDY

A.1 Synchronous Generators

Table A.1: Synchronous generator data.

	G_N1	G_N5	G_S1	G_S2	G_S4	G_S6
Rating, MVA	25	158	192	147.1	192	231.6
Rated voltage, kV	13.2	13.8	18	15.5	18	13.8
Armature resistance, r_a , p.u.	0.005	0.005	0.002	0.002	0.002	0.005
Leakage reactance, x_l , p.u.	0.18	0.18	0.184	0.184	0.184	0.18
Direct-axis synchronous reactance, x_d , p.u.	1.18	1.18	2.03	2.03	2.03	1.18
Quadrature-axis synchronous reactance, x_q , p.u.	0.78	0.78	1.97	1.97	1.97	0.78
Direct-axis transient reactance, $x_d^{'}$, p.u.	0.295	0.295	0.309	0.309	0.309	0.295
Quadrature-axis transient reactance, $x_q^{'}$, p.u.	0.2868	0.2868	0.471	0.471	0.471	0.2868
Direct-axis subtransient reactance, $x_d^{''}$, p.u.	0.2362	0.2362	0.225	0.225	0.225	0.2362
Direct-axis transient open-circuit time constant, $T_{do}^{'}$, s	3.996	3.996	7.32	7.32	7.32	3.996
Quadrature-axis transient open-circuit time constant, $T_{qo}^{'}$, s	0.0484	0.0484	0.67	0.67	0.67	0.0484
Direct-axis subtransient open-circuit time constant, $T_{do}^{''}$, s	0.0297	0.0297	0.022	0.022	0.022	0.0297
Zero-sequence reactance, x_0 , p.u.	0.18	0.18	0.184	0.184	0.184	0.18
Inertia constant, H, s	3.5	3.5	4.15	4.15	4.15	3.5

A.2 Transformers

Table A.2: Transformer data.

	TN_1	TN_5	TS_1	TS_2	TS_4	TS_6
Rating, MVA	25	175	200	150	200	250
Rated voltage, kV	13.2/138	13.8/138	18/220	15.5/220	18/220	13.8/220
Resistance, r_T , p.u.	0.002	0.002	0.002	0.002	0.002	0.002
Leakage reactance, x_T , p.u.	0.12	0.12	0.12	0.12	0.12	0.12

A.3 Transmission Lines

All transmission lines have the same series impedance and shunt admittance per unit length.

Transmission voltage = 138 kV:

Positive Sequence Parameters:

$$Z_{T.L.series} = 0.13047 + j\,0.4847\ \Omega/km$$

$$Y_{T.L.shunt} = j\,3.3679\ \mu S/km$$

Zero Sequence Parameters:

$$Z_{T.L.series} = 0.65235 + j\,01.4541\ \Omega/km$$

$$Y_{T.L.shunt} = j\,1.1226\ \mu S/km$$

Transmission voltage = 220 kV:

Positive Sequence Parameters:

$$Z_{T.L.series} = 0.093 + j\,0.501144\ \Omega/km$$

$$Y_{T.L.shunt} = j\,3.338448\ \mu S/km$$

Zero Sequence Parameters:

$$Z_{T.L.series} = 0.465 + j\,1.503432\ \Omega/km$$

$$Y_{T.L.shunt} = j1.112816\ \mu S/km$$

A.4 System Loads

$N_2 = 32 + j\,24\ MVA$

$N_3 = 28 + j\,21\ MVA$

$S_3 = 150 + j\,50\ MVA$

$S_5 = 90 + j\,40\ MVA$

A.5 Excitation System

Table A.3: Excitation system data.

K_A = 2	K_E = 1.0
K_{FE} = 0.03	T_A = 0.04 s
T_{FE} = 1.0 s	T_E = 0.01s
Lim_max = 4.75 p.u.	*Lim_min* = -4.75 p.u.